INTERNATIONAL JOURNAL OF
IJCOE
COASTAL OFF SHORE AND
ENVIRONMENTAL ENGINEERING

Internal Waves in the Strait of Hormuz using Sentinel-1 radar images
Sahar Tajbakhsh Mosalman, Hossein Farjami, Akbar Rashidi Ebrahim Hesari, Sajjad Andi

Long-range Power Density Profiling Measurement Using Coastal Acoustic Tomography (Study area: Persian Gulf)
Mehran Sadeghi Delooee, Reza Alimardani,Hossein Mousazadeh, Masoud Bahreinimotlagh, Reza Roozbahani, Mortaza Eftekari, Mohammed Basel AlSawaf, Sayyed Ahmad Sajjadi, Ashkan Farokhnia, Reza Hosseinzadeh Asl, Ali Davaei

Probability density functions of the DoB in tubular KT-joints of jacket-type platforms under out-of-plane bending loads
Hamid Ahmadi, Esmaeil Zavvar, Vahid Mayeli

Comparative Analysis of Distorted Froudian and Equivalent Single Degree of Freedom Models in Offshore Jacket Platform Seismic Simulation
Mohamadhosein Mohasel, Ahmad Reza Mostafa Gharabaghi, Mohamad Reza Chenaghlou

Analyzing the Impact of Non-Dimensional Hydrodynamic Coefficients on the Performance of Oscillating Wave Surge Converters
Ghazale Sadripour, Rouzbeh Shafaghat*, Behrad Alizadeh Kharkeshi

The Impact of Westward Currents in the Indian Ocean on Precipitation in Western and Southwestern Iran
Ali Sadeghi, Farzaneh Jafari Hombari, Farshad Pazhoh, Mohammadreza Rozbahany

Volume 10 Issue 2| Mar 2025

WWW.IJCOE.org info@ijcoe.org

www.ijcoe.org

International Journal of Coastal, Offshore and Environmental Engineering (IJCOE) Vol.10/Issue 2/ May 2025

39

International Journal of Coastal, Offshore & Environmental Engineering

Since 2015

ISSN: 2980-8731 (online)

Volume 10 | Issue2 | May 2025

IJCOE

Editor-in-Chief: Prof. Hamid S.Bahai

International Journal of
Coastal, Offshore
& Environmental
Engineering
Since 2015
ISSN: 2980-8731 (online)

In The Name of God

Message from the Editor-in-Chief

The IJCOE journal office was established in 2015,and its first issue was published in 2016. TheIJCOE covers a wide range of research in thefields of oceanography & ocean technology, aswell as marine industries & marine engineering.The editorial board of IJCOE consists of nearly130 of the greatest scientists and researchersfrom over 30 countries worldwide, and thejournal's review board comprises 1,000 membersfrom all five continents. The membership andapplication process for joining the editorial andreview boards of this journal is ongoing. IJCOE isa research-academic quarterly journal that haspublication and distribution permissions fromthe Press Organization and permission topublish scientific-research articles from theMinistry of Science, Research, and Technology(MSRT) with an "A" rating. It also holds a "Q1"rating from the ISC institute with an impactfactor (IF) of approximately 0.43 and isconsidered a "core journal" (prestigious andoutstanding journal). IJCOE is an open-accessjournal and allows the download and receipt ofaccepted articles in full text for free. It respectsand adheres to copyright and COPE regulations.The journal's office operates 24/7, providingservices to researchers. In addition to publishinga regular quarterly journal, IJCOE has 16 specialissues on specific topics in preparation. It alsoprovides conditions for publishing specializedbooks, references, and handbooks. Moreover, itis ready to cooperate with the secretariats ofreputable international conferences to publishtheir selected and outstanding articles. IJCOEevaluates, appraises, and publishes books,articles, and the scientific achievements andfindings of esteemed researchers and scientistsworldwide who are innovating and conductingin-depth research in the "important and strategicfield of the maritime technology & Oceanengineering." It welcomes any form of jointcooperation with universities, research institutes,and related research centers at the national,regional, and international levels, and extends ahand for collaboration.

Classification of Editorial Board in IJCOE

- Editor-in-Chief
- Director-in-Chief
- Deputy Editor
- Executive Managers
- English Text Editor
- Technical Editor
- International Editorial Board
- National Editorial Board
- Editorial Board Associate
- Editorial Board Assistant
- Guest Editorial Board
- Advisory Board
- Administrative Coordinator
- Honorary Board Member
- Methodology Advisor

Author Benefits

- Open Access
- Rapid Publication
- Thorough Peer-Review
- No Copyright Constraints
- Coverage by Leading Indexing Services
- Discounts On Article Processing Charges (APC)
- No Space Constraints, No restriction on the maximum length of the papers, number of figures or colors

Aims of IJCOE

Hydrodynamics

Marine equipment

Structural mechanics

Ocean environmental predictions

Stochastic calculations Experimental

Automatic Control of Marine Systems

Scope of IJCOE

Marine Hazards

Ocean Acoustics

Naval Architecture

Ocean Engineering

Coastal Engineering

Marine Meteorology

Marine Earth Sciences

Underwater Technology

Marine Renewable Energy

Polar & Arctic Engineering

Marine Renewable Energy

Marine Geography & Geodesy

Marine Environmental Engineering

Automatic Control of Marine Systems

Hydro Physics & Physical Oceanography

Type of papers

- Case Studies
- Book Reviews
- Review Article
- Letters to the Editor
- Methodology Papers
- Editorials and Commentaries
- Response or Rejoinder Papers
- Perspective or Opinion Papers
- Conceptual or Theoretical Papers
- Meta-Analysis and Systematic Reviews
- Short Communications or Brief Reports
- Research Articles (Original Research Papers)

Scientific Research Journal

Ministry of Science, Research And Technology (MSRT)

Jurnal Ranking 2023: A

Ministry Of Science, Research And Technology (ISC)

Citation Impact 2022: 0.429

Quartile 2022 : Q1

Core Collection

IJCOE is a Member of

- CIVILICA We Respect the Science
- Google Scholar
- Jouroscope
- COPE 20TH ANNIVERSARY 1997-2017 cc BY NC SA
- ISC
- JREF.IR Journals Reference
- DOAJ DIRECTORY OF OPEN ACCESS JOURNALS
- ISSN INTERNATIONAL STANDARD SERIAL NUMBER INTERNATIONAL CENTRE
- Researcher.Life
- doi Crossref EScience Press mEDRA
- iThenticate
- magiran
- OPEN ACCESS
- pistotn
- RG ResearchGate
- Regional Information Center for Science and Technology RICEST
- ScienceGate
- Scilit
- SID
- website.informer.com
- WEBrate

Cantact Us

Office 1 | Research Institute of Meteorology and Atmospheric Science

Address | Tehran, Shahid Kharrazi Highway, Pajoohesh Blvd, Research Institute of Meteorology and Atmospheric Science, Sand and Dust Storm International Research Center (SDS-IRC), No. 13, 1st floor.

Phone | +982144787652

Postal code | 13611-14977

website | www.rimac.ac.ir

Office 2 | Iranian National Institute for Oceanography and Atmospheric Science

Address | Tehran, Dr. Fatemi Gharbi St., Shahid Etemadzade St., No. 3, third floor.

Phone | +982166944873

Postal code | 13389 – 14118

website | www.inio.ac.ir

Email | Info@ijcoe.org

Website | www.ijcoe.org

Follow Us

www.ijcoe.org

INTERNATIONAL JOURNAL OF IJCOE COASTAL, OFFSHORE & ENVIRONMENTAL ENGINEERING

Volume & Issue:

Volume 10, Issue 2, May 2025

Number of Articles: 6

Content

Internal Waves in the Strait of Hormuz using Sentinel-1 radar images 1

Sahar Tajbakhsh Mosalman, Hossein Farjami, Akbar Rashidi Ebrahim Hesari, Sajjad Andi

Long-range Power Density Profiling Measurement Using Coastal Acoustic Tomography (Study area: Persian Gulf) 7

Mehran Sadeghi Delooee, Reza Alimardani,Hossein Mousazadeh, Masoud Bahreinimotlagh, Reza Roozbahani, Mortaza Eftekari, Mohammed Basel AlSawaf, Sayyed Ahmad Sajjadi, Ashkan Farokhnia, Reza Hosseinzadeh Asl, Ali Davaei

Probability density functions of the DoB in tubular KT-joints of jacket-type platforms under out-of-plane bending loads 16

Hamid Ahmadi, Esmaeil Zavvar, Vahid Mayeli

Comparative Analysis of Distorted Froudian and Equivalent Single Degree of Freedom Models in Offshore Jacket Platform Seismic Simulation 35

Mohamadhosein Mohasel, Ahmad Reza Mostafa Gharabaghi, Mohamad Reza Chenaghlou

Analyzing the Impact of Non-Dimensional Hydrodynamic Coefficients on the Performance of Oscillating Wave Surge Converters 45

Ghazale Sadripour, Rouzbeh Shafaghat*, Behrad Alizadeh Kharkeshi

The Impact of Westward Currents in the Indian Ocean on Precipitation in Western and Southwestern Iran 54

Ali Sadeghi, Farzaneh Jafari Hombari, Farshad Pazhoh, Mohammadreza Rozbahany

INTERNATIONAL JOURNAL OF
COASTAL, OFFSHORE & ENVIRONMENTAL ENGINEERING IJCOE Vol.10/No. 2/Spring 2025 (1-6)

Available online at: www. Ijcoe.org

Internal Waves in the Strait of Hormuz using Sentinel-1 radar images

Sahar Tajbakhsh Mosalman[1], Hossein Farjami[2*], Akbar Rashidi Ebrahim Hesari[3], Sajjad Andi[4]

[1],Sahar Tajbakhsh Mosalman, Assistant Professor, Atmospheric Exploration Department, Institute of Meteorology and Atmospheric Sciences,
*[2]*Iranian National Institute for Oceanography and Atmospheric Science, Tehran, IRAN*
[3,4]Tarbiat Modares University, Tehran, IRAN

ARTICLE INFO

Article History:
Received : 15 Nov 2023
Accepted : 02 Jun 2025

Keywords:
Internal waves,
Strait of Hormuz,
radar and satellite images,
Sentinel-1

ABSTRACT

Internal waves (IWs) are oscillations of the water column that occur at the interface between two layers of different densities. They play an important role in ocean dynamics, mixing, and biogeochemical processes. However, IWs are difficult to observe and measure *in situ*, especially in complex and narrow regions such as the Strait of Hormuz. This study uses bathymetric data and over 100 satellite and radar images from different sensors and platforms to investigate the occurrence and behavior of IWs in the Strait of Hormuz. The results show that IWs are persistent in this area due to the interaction of the internal current with the steep slope of the strait. The waves emerge in shallow waters near the coasts of Iran and Oman, but they change their direction and location when they reach the continental shelf. The leading crest of IWs has a length ranging from 10 to 20 km, and the wavelength varies from 1 to 3 km. The study confirms the findings of previous numerical simulations of internal wave generation and propagation in this region. It also suggests that the bathymetry is the main factor influencing IWs in the Strait of Hormuz, rather than water column stratification. This study provides new insights into the spatial and temporal characteristics of IWs in the Strait of Hormuz, which can help improve the understanding and modeling of ocean circulation and ecology in this region.

1. Introduction

Human life depends on various aspects of the oceans and seas, such as economy, politics, and society. They provide resources such as oil and gas, transportation routes, recreation opportunities, and livelihoods for coastal communities [1]. The oceans and seas also influence the atmospheric systems, climate regulation, precipitation patterns, storms, and other environmental phenomena [2, 3]. Coastal waters are particularly important areas that have various functions and challenges. Processes such as waves, surface wind, currents, and internal waves (IWs) affect them[4] IWs are phenomena that occur in fluids with different densities, when currents encounter irregular topography [5][5]. These waves are generated by disturbances in the ocean with stable stratification. Eddy currents are the main factor that creates these waves [6].

IWs are waves that occur within the ocean, between layers with different densities. Ekman first identified them in 1904, who observed them because of ship motion. They have a wide range of wavelength, period, and amplitude, and they can cause environmental changes such as nutrient mixing, animal mass distribution, and sediment suspension in the sea [7]. IWs are one of the prominent dynamic features of all stratified fluids in the ocean, sea, lake and water bodies [8]. The density difference between the layers can be caused by temperature, salinity and pressure that, air-sea interaction can influence such variations [9]. IWs can have various effects on the environment, such as mixing nutrients, transporting sediments, and influencing acoustic propagation.

Moreover, the study of IWs propagation in the ocean basins is important for many industries, such as shipbuilding, marine engineering, and military industries. In addition, these waves affect the sound speed distribution in the horizontal and vertical directions, and their study is especially necessary for submarine navigation. Therefore, the investigation and recognition of IWs is not only important for marine transportation, coastal engineering, water movement, but also for oil projects and offshore platforms [10], [11]. Remote sensing technology can detect IWs, even though they occur below the surface. They look like alternating dark and light parallel lines in radar and satellite images[12, 13].

The Strait of Hormuz is a strategic location for oil transportation and regional security[14]. The Strait of Hormuz is a narrow and shallow passage that connects the Persian Gulf and the Oman Sea. Azizpour et al. (2015) investigated the seasonal variability of the Persian Gulf outflow water (PGOW) volume and its impact on the water masses in the Strait of Hormuz. They found that the PGOW volume reached its maximum in spring, when the surface salinity gradient between the Persian Gulf and the Gulf of Oman was the highest. They also identified two distinct water masses in the eastern part of the strait. In summer, these two water masses extended to the central and western part of the strait, forming a three-layered structure in the water column. The interfaces between the water masses were characterized by sharp fronts with different intensities, depending on the temperature and salinity gradients [15]. However, it is also a challenging environment for IWs generation and propagation, due to its complex bathymetry and hydrography. The main objective of this study is to investigate the occurrence and characteristics of IWs in the Strait of Hormuz, using satellite and radar images. The results provide a better understanding of the dynamics and impacts of IWs in this region, which has a crucial strategic role in the region and the world, both militarily and economically. This study employs Sentinel-1 radar images to explore the generation mechanisms of IWs in the Strait of Hormuz

2. Data and Methodology

2.1- Study area

The Strait of Hormuz is a narrow and curved sea passage that connects the Persian Gulf to the Sea of Oman, in the northwestern of the Indian Ocean. It lies between the Iranian plateau and the Arabian Peninsula, at about 26°30' N and 56°30' E [16], [17]. The Sea of Oman is a branch of the Arabian Sea that has an L-shaped configuration and extends eastward from the Strait of Hormuz. The Persian Gulf is a semi-enclosed water body that lies westward from the Strait of Hormuz and has an average depth of 35 m. The deepest point in the Persian Gulf is about 90 m, while the Strait of Hormuz reaches more than 100 m in depth [18]. The Strait of Hormuz is the only outlet for the waters of the Persian Gulf and has a significant strategic and economic importance for the region and the world (Figure 1).

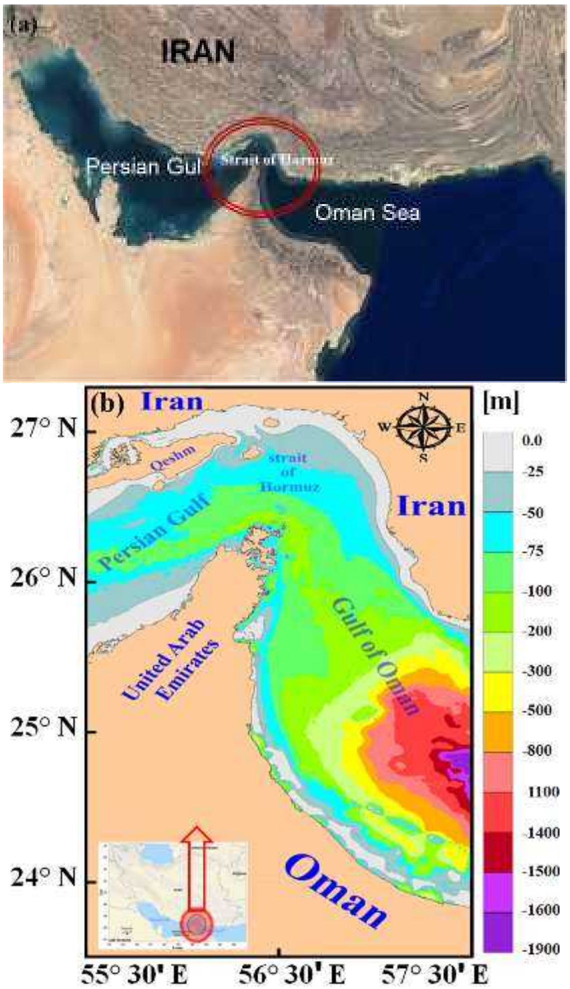

Figure 1: Topography and geographic location of the Strait of Hormuz

2.2- Satellite data

This study used SAR radar images from Sentinel-1 satellite in 2015 and geostationary data and altitudes[19] to identify IWs in the Strait of Hormuz. Sentinel-1 is a European radar observatory that developed as part of the Global Monitoring for Environment (GMES) space programs. It consists of two satellites, Sentinel-1A and Sentinel-1B, which launched by the European Space Agency (ESA) on April 3, 2014 and April 25, 2016, respectively. Sentinel-1 mission operates in C-band frequency, which is suitable for detecting IWs in SAR radar images [20]. It offers four different imaging modes with resolutions up to 5 m and coverage up to 400 km. By using one or more SAR images, the two-dimensional structure of IWs can be determined by measuring features such as crest length, number of wave packets, propagation direction, distance between neighboring wave packets, and wavelength. This allows us to investigate IWs from their generation to their development and propagation, at smaller temporal and spatial scales, using satellite observations.

2.3- Data Analysis

To examine the temporal variability of IWs in the Strait of Hormuz, we obtained the SAR images of Sentinel-1 satellite for all seasons of the year from the website (https://scihub.copernicus.eu/). To isolate internal tides from satellite observations, we applied a two-step procedure: data preprocessing and plane-wave fitting. The data preprocessing aimed to eliminate outliers and barotropic signals from the original data and compute the parameters for the plane-wave fitting [21, 22]. We applied preliminary processing and appropriate filters to the radar images, analyzed, and processed them fully in SNAP, Arc Map and Matlab programing platform. We used edge detection techniques in Matlab to identify IWs from the corrected SAR images. We applied Sobel and Canny filters, which are methods of edge detection that reduce unnecessary information from the data while preserving the important structural features [23]. These filters also reduce the noise in the image. By performing the required processing, we revealed the IWs in the images. After analyzing the satellite images, we tried to determine the generation mechanism of IWs by using bathymetric data and processed images. We used Surfer and Grapher software to plot the two-dimensional and three-dimensional shape of the bathymetry, which showed a relatively high slope in this area (Figure 1b).

3. Results and Discussion

The dynamics of internal gravity waves depend on several factors, such as the stratification of the fluid, the shape of the seafloor or the terrain, the tidal forces, the wind or pressure fluctuations, and the nonlinear interactions among the waves. Internal gravity waves can have different wavelengths, periods, amplitudes, and propagation directions, depending on these factors.

We analyzed the Sentinel-1 satellite radar images for all seasons of 2015 in the Strait of Hormuz region and found that IWs occur in most months of the year in this region. We examined the topography of the region and the IWs observed in the radar images and found that the IWs packets form after crossing the slope of the continental shelf and entering the shallow coastal waters near the coasts of Iran and Musandam. We also observed IWs packets around the islands of Lark, Qeshm, Hangam and near the coasts of the cities of the emirate such as Al-Rams, Al-Hamra Island and Ras Al-Khaimah. However, we did not include them in this study because they are located in the Persian Gulf basin, not in the Strait of Hormuz. We collected more than 100 images from Sentinel-1 in the Strait of Hormuz in 2015 and detected IWs in them. The number of radar images in each season was more than 20. Figure 2 shows an example of IWs in the Strait of Hormuz from a Sentinel-1 image recorded on June 30, 2015. In this image, we identified two IWs packets P1 and P2 (Figure 2a) with different propagation directions. The P1 (Figure 2b) IW packet originated at a distance of 11 km west of Mubarak Mount and propagated towards the west. The P2 (Figure 2c) IW packet was detected at a distance of 22 km southwest of Mubarak Mount and propagated towards the northwest. As we mentioned earlier, this area has a steep slope that causes IWs to form near the coasts and in shallow areas after the internal current passes over the slope of the continental shelf. The IWs observed in the radar images in this area could be related to the tidal currents interacting with the seafloor roughness in the Strait of Hormuz.

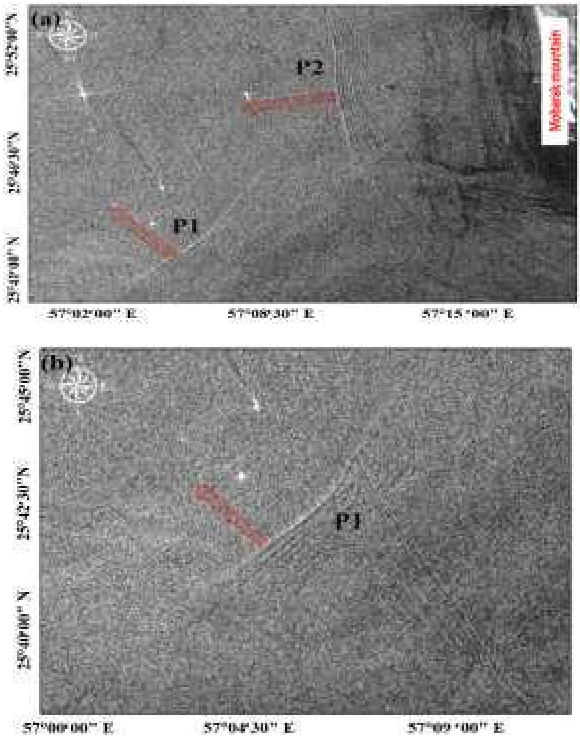

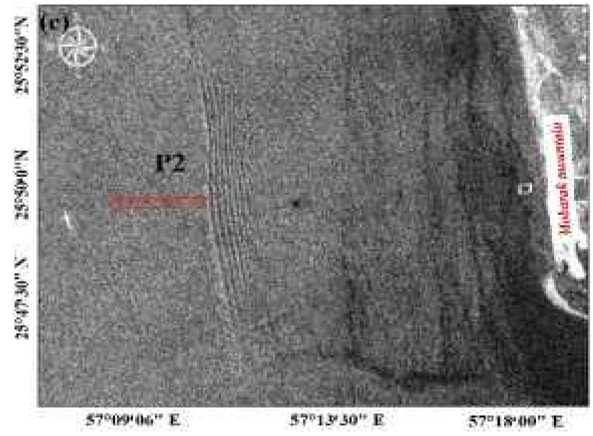

Figure 2: Sentinel-1 image, IWs near the shores of Mount Mubarak (Iran) on 06/30/2015.

Figure 3 shows another example of IWs in the Strait of Hormuz from a Sentinel-1 image recorded on October 28, 2015. In this image, we detected an IW packet near the coast of Sirik, which propagated towards the east, i.e., towards the coast of Sirik and Sarkhor Taheroi. This packet was located 12 km west of Sirik city. The leading wave crest had a length of about 15 km, considering the shape of the lowlands and the seafloor elevations in this area (Figure 1) we expected that the IWs in this area were generated by the tidal currents passing over the slope of the continental shelf.

Figure 3: Sentinel-1 image, IWs near Sirik (Iran) on 10/28/2015.

Figure 4 shows another example of IWs in the Strait of Hormuz from a Sentinel-1 image recorded on July 24, 2015. In this image, we detected two IWs packets near the coasts of Kirtan and Brizek, which were separated by a distance of 7 km. The propagation direction of these two packets was almost the same and was towards the east. These waves were located at a distance of 12 and 19 km from Brizak, respectively. The leading wave crest of the IWs packets P1 and P2 (Figure 2a) had a length of about 10 and 20 km, respectively.

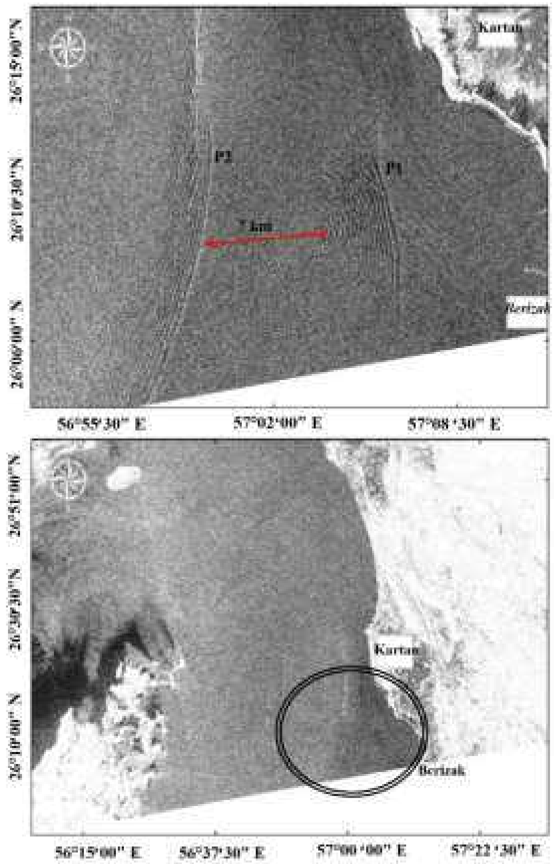

Figure 4: Sentinel-1 image, IWs near the coast of Brizak (Iran) on 07/24/2015.

Based on the findings of this study, we concluded that the IWs that occur in different locations of the Strait of Hormuz, are generated by the tidal currents passing over the seafloor irregularities in shallow areas and near the coasts. When the tidal currents encounter the sloping topography of the strait, they generate internal waves at the interface of the stratified water layers. These internal waves propagate along the density gradient, and can have large amplitudes and wavelengths.

3. Conclusion

We investigated IWs based on the channel shape, the seafloor elevation, and the processing of more than 100 satellite and radar images that cover the entire Strait of Hormuz. The results indicate that the IWs in the Strait of Hormuz are persistent and continuous due to the internal current passing over the steep slope in this area, and they occur in shallow areas near the coasts. However, these waves do not always occur in a same location because they form in different directions and start spreading and propagating after crossing and hitting the continental shelf. We also identified IWs in the eastern and western parts of the Strait of Hormuz by analyzing radar images using the software mentioned earlier. The length of the leading crest of the

IWs that we detected in this area ranged from 10 to 20 km. We considered the water column stratification and the flexible currents passing over the seafloor surfaces with variable slope as the formation factors of IWs. The results of internal waves manifestation in the Strait of Hormuz are similar to the findings of [4], [13].

We compared our results with the previous study by [24] who used the MITgcm model in non-hydrostatic and fully nonlinear conditions to simulate the three-dimensional evolution of nonlinear IWs in the Gulf of Oman continental shelf. They identified three stages of internal wave formation in their study. The first stage was when IWs are generated from the deep parts and propagate towards the Musandam coasts; the second stage was happened when IWs form after entering the continental shelf areas and expand towards the coasts of Iran; and the third stage can be presented when these waves spread towards the coasts of Oman[24]. We found a good agreement between our results and those of Khalilabadi et al. (2015), as well as those of [25], who used a different model to study the IWs in the same region. We used Sentinel-1 satellite radar images to reveal the IWs packets formed in the whole study area, especially near the coasts of Iran. We also examined the shape of the lowlands and the seafloor elevations in this area. We concluded that these waves are generated at a depth of 25 m, which is consistent with the second stage of IWs formation predicted by Khalilabadi et al. (2015). The IWs packets that we detected agree with their study.

We found that the IWs in the Strait of Hormuz, which are observed with a relatively high density, are generated in all areas by the tidal currents passing over the seafloor surfaces with variable slope, and are influenced by the seafloor depth and height. We determined that the water column stratification does not play a role in the formation of IWs in the Strait of Hormuz.

Acknowledgement

This is to certify that the Iranian National Institute for Oceanography and Atmospheric Science (INIOAS) has supported the current research project through the proposal (INIOAS-1400-031-01-39-01). The authors would like to express their gratitude to the USGS Earth Explorer and Copernicus for providing data and information.

References

[1] K. Evans, N. Bax, and D. C. Smith, “Australia state of the environment 2016: marine environment, independent report to the Australian Government Minister for the Environment and Energy,” *Australian Government Department of the Environment and Energy, Canberra*, 2017.

[2] Y. Lu *et al.*, “Major threats of pollution and climate change to global coastal ecosystems and enhanced management for sustainability,” *Environmental Pollution*, vol. 239, pp. 670–680, 2018. https://doi.org/10.1016/j.envpol.2018.04.016

[3] S. Andi, A. Rashidi Ebrahim Hesari, and H. Farjami, “Detection of internal waves in the Persian Gulf,” Remote Sensing Letters, vol. 12, no. 2, pp. 190–198, 2021. https://doi.org/10.1080/2150704X.2020.1847349

[4] V. Klemas, “Remote sensing of ocean internal waves: An overview,” J Coast Res, vol. 28, no. 3, pp. 540–546, 2012. https://doi.org/10.2112/JCOASTRES-D-11-00156.1

[5] S. A. Thorpe, The turbulent ocean. Cambridge University Press, 2005. https://doi.org/10.1017/CBO9780511819933

[6] W. S. Holbrook and I. Fer, “Ocean internal wave spectra inferred from seismic reflection transects,” Geophys Res Lett, vol. 32, no. 15, 2005. https://doi.org/10.1029/2005GL023733

[7] P. H. Leblond and L. A. Mysak, “Waves in the Ocean Elseviers Oceanographic Series. 602 pp.” Elsevier Scientific Publ. Company, Amsterdam, Oxford, New York, 1978. https://doi.org/10.1007/s00024-019-02263-8

[8] B. A. Hughes, “The effect of internal waves on surface wind waves 2. Theoretical analysis,” J Geophys Res Oceans, vol. 83, no. C1, pp. 455–465, 1978. https://doi.org/10.1029/JC083iC01p00455.

[9] A. I. Belov, V. A. Zhuravlev, and A. N. Serebryanyĭ, “Sound field variations caused by intense internal waves in a shallow sea with a weak thermocline,” Acoust Phys, vol. 52, pp. 132–137, 2006. https://doi.org/10.1134/s1063771006020035.

[10] T. F. Duda and J. C. Preisig, “A modeling study of acoustic propagation through moving shallow-water solitary wave packets,” IEEE journal of oceanic engineering, vol. 24, no. 1, pp. 16–32, 1999. https://doi.org/10.1109/48.740153.

[11] J.-F. Cretaux, S. Calmant, F. Papa, F. Frappart, A. Paris, and M. Berge-Nguyen, “Inland surface waters quantity monitored from remote sensing,” Surv Geophys, pp. 1–34, 2023. https://doi.org/10.1007/s10712-023-09803-x

[12] A. Rashidi Ebrahim Hesari, S. Andi, and H. Farjami, “Study of Internal Waves in the Persian Gulf Using Field Data and Satellite Images,” International Journal of Coastal and Offshore Engineering, vol. 2, no. 4, pp. 9–16, 2019. https://doi.org/10.29252/ijcoe.2.4.9

[13] R. K. Ramazani, *The Persian Gulf and the strait of Hormuz*. Brill Archive, 1979.

[14] J. Azizpour, V. Chegini, M. Khosravi, and A. Einali, “Study of the physical oceanographic properties of the persian gulf, strait of hormuz and gulf of oman based on PG-GOOS CTD measurements,” Journal of the Persian Gulf, vol. 5, no. 18, pp. 37–48, 2014. URL: http://marine-eng.ir/article-1-939-fa.html (In Persian).

[15] K. R. Walters and W. F. Sjoberg, *The Persian Gulf region: a climatological study*. USAF Environmental Technical Applications Center, 1988.

[16] M. reza abbasi, “Evaluating semi-empirical wave forecasting method CEM in the Strait of Hormuz,” *International Journal of Coastal, Offshore and Environmental Engineering(ijcoe)*, vol. 4, no. 3, pp. 43–46, 2019, https://doi.org/10.29252/ijcoe.3.3.43.

[17] M. Heidarzadeh, J. Šepić, A. Rabinovich, M. Allahyar, A. Soltanpour, and F. Tavakoli, “Meteorological tsunami of 19 March 2017 in the Persian Gulf: observations and analyses,” *Pure Appl Geophys*, vol. 177, pp. 1231–1259, 2020. https://doi.org/10.1016/j.wace.2022.100527.

[18] K. Clauss, M. Ottinger, P. Leinenkugel, and C. Kuenzer, “Estimating rice production in the Mekong Delta, Vietnam, utilizing time series of Sentinel-1 SAR data,” *International journal of applied earth observation and geoinformation*, vol. 73, pp. 574–585, 2018. https://doi.org/10.1016/j.jag.2018.07.022.

[19] I. Karang and T. Osawa, “Internal solitary waves propagation speed estimation in the northern-part of Lombok Strait observed by Sentinel-1 SAR and Himawari-8 images,” in *IOP Conference Series: Earth and Environmental Science*, IOP Publishing, 2021, p. 012042. https://iopscience.iop.org/article/10.1088/1755-1315/944/1/012042.

[20] W. R. Alpers, F. Bignami, D. Cavaliere, and G. Sannino, “SAR observation of internal waves generated by sub-mesoscale eddies in the Strait of Sicily,” *Authorea Preprints*, 2022. http://dx.doi.org/10.1002/essoar.10511912.1.

[21] H. Farjami and S. Andi, “Satellite Image Dataset of Internal Waves in the Persian Gulf,” *International Journal of Maritime Technology*, pp. 107–110, 2021. URL: http://ijmt.ir/article-1-778-en.html.

[22] C.-X. Deng, G.-B. Wang, and X.-R. Yang, “Image edge detection algorithm based on improved canny operator,” in *2013 International Conference on Wavelet Analysis and Pattern Recognition*, IEEE, 2013, pp. 168–172. https://doi.org/10.1016/j.procs.2020.08.049.

[23] B. Morro *et al.*, “Offshore aquaculture of finfish: Big expectations at sea,” *Rev Aquac*, vol. 14, no. 2, pp. 791–815, 2022. https://doi.org/10.1111/raq.12625.

[24] M. R. Khalilabadi, M. Sadrinassab, V. Chegini, and M. Akbarinassab, “Internal wave generation in the Gulf of Oman (outflow of Persian Gulf),” 2015. https://doi.org/10.3390/w15040746.

[25] G. S. Carter, M. C. Gregg, and R.-C. Lien, “Internal waves, solitary-like waves, and mixing on the Monterey Bay shelf,” *Cont Shelf Res*, vol. 25, no. 12–13, pp. 1499–1520, 2005. https://doi.org/10.1016/j.csr.2005.04.011.

INTERNATIONAL JOURNAL OF
COASTAL, OFFSHORE & ENVIRONMENTAL ENGINEERING IJCOE Vol.10/No. 2/Spring 2025 (7-15)

Available online at: www. Ijcoe.org

Long-range Power Density Profiling Measurement Using Coastal Acoustic Tomography (Study area: Persian Gulf)

Mehran Sadeghi Delooee[1], Reza Alimardani[2*],Hossein Mousazadeh[3], Masoud Bahreinimotlagh[4], Reza Roozbahani[5], Mortaza Eftekari[6], Mohammed Basel AlSawaf[7], Sayyed Ahmad Sajjadi[8], Ashkan Farokhnia[9], Reza Hosseinzadeh Asl[10], Ali Davaei[11]

1 Department of Mechanical Engineering of Biosystems, University of Tehran, Tehran, Iran

*2 *Department of Mechanical Engineering of Biosystems, University of Tehran, Tehran, Iran (r.mardani@ut.ac.ir)*

3 Department of Mechanical Engineering of Biosystems, University of Tehran, Tehran, Iran

4 Water Research Institute, Tehran, Iran

5 Water Research Institute, Tehran, Iran

6 Water Research Institute, Tehran, Iran

7 Faculty of Engineering Department of Civil and Environmental Engineering, Kitami Institute of Technology, Kitami, Japan

8 Department of Mechanical Engineering, Iran University of Science and Technology, Tehran, Iran

9 Department of Energy, Institute of Science and High Technology and Environmental Science, Graduate University of Advanced Technology, Kerman, Iran

10 College of Agricultural Engineering and Technology, University of Tehran, Iran

11 Department of Computer Engineering, South Tehran Branch, Islamic Azad University, Tehran, Iran

ARTICLE INFO

Article History:
Received : 21 Feb 2024
Accepted : 10 Jun 2025

Keywords:
Tidal stream turbine
Layered current velocity
Persian Gulf
CAT
Inverse Problem

ABSTRACT

Prior to the design and installation of tidal stream turbines, a thorough understanding of coastal hydrodynamic parameters, such as power density, is essential. The accurate estimation of current velocity is a key component in power density calculations. Acoustic Tomography (AT), as a robust remote sensing technique, is widely employed to measure currents velocities across various water layers. This methodology relies on recording the travel time of acoustic waves propagating through the water layers, followed by the solution of the associated AT inverse problem. This study conducted a reciprocal sound transmission experiment in the Persian Gulf, employing two 10-kHz Coastal Acoustic Tomography (CAT) stations situated 3 km apart, and submerged 6 meters beneath the water surface. The five-layer structures of the range-averaged current in the vertical section were reconstructed through regularized inversion of the travel time data for two rays. The regularized inversion revealed a maximum velocity of 0.89 m/s within layer 3 (20-30 m depth). Notably, velocity inversion errors across all five layers (1-5) remained negligible, ranging from 0.006 to 0.014 m/s, compared to the observed velocity variation. Further analysis of the velocity histogram indicated that the dominant current speeds at the site fell within the range of 0.1-0.5 m/s, falling short of the standard economic threshold of 1 m/s for tidal energy conversion. These findings demonstrate the potential of CAT to accurately profile coastal current velocities.

1. Introduction

There are several substitutes available to reduce greenhouse gas (GHG) emissions from energy systems that can meet the global energy demand. Renewable energy stands as a promising alternative, which has great potential for climate change mitigation, social and economic development, providing a safe source of energy, and reducing environmental impact (Thiébaut et al., 2020).

The oceans, which cover more than two-thirds of the earth, have significant amounts of energy in the form of waves, tidal currents (Jahromi, 2024; khoshkholgh, 2023), as well as heat and salinity gradients (Bahaj, 2013). Tidal stream energy, or marine hydrokinetic energy (MHKE), attracts significant attention compared to other forms of ocean energy due to its reliable and predictable nature (Radfar et al., 2017). The life cycle of a tidal energy typically involves three main stages: (1) design and construction, (2) installation, and (3) operation and maintenance.

Monitoring and measuring the flow field, particularly the vertical variation of current velocity, is crucial throughout the life cycle of a tidal energy converter. During Stage 1, this information is paramount for tidal energy converter developers, as many industry-standard flow characterization metrics depend on descriptions of the underlying mean flow (Sellar & Wakelam, 2018; Thiébaut et al., 2020). During Stage 2, thorough resource assessment becomes critical. This process ensures the safe utilization and efficient operation of tidal stream turbines (Gunawan et al., 2014).

As stated, the resource assessment, specifically measuring power density, is a key action in developing and installing tidal stream turbines. While the primary parameter assessed is current velocity, there is no significant difference between resource assessments of different tidal stream energy converters (turbines and kites).

Acoustic Tomography (AT) has evolved as a valuable tool for monitoring coastal waters, without disrupting activities like fishing and shipping. This technology uses a special technique that analyzes travel times of acoustic signals in water to extract the parameters of an aquatic medium (including sound speed, current velocity, and temperature) on a large scale area. A typical AT device (Figure 1 b) is comprised of a pair of acoustic transducers and processing units (Kaneko et al., 2020).

This study aims to reconstruct high-resolution vertical profiles of current velocity. Many researchers have mapped vertical profiles of current velocity and water temperature using AT and compared their results with Acoustic Doppler Current Profiler (ADCP), Acoustic Doppler Velocimeter (ADV), and CTD measurements.

Taniguchi et al. (2013) employed AT to profile the flow velocity of the Kuroshio Current in southeast Taiwan, comparing their results with data from a moving ADCP. They used the explicit solution and regularized inversion to estimate the current velocity. Their analysis found a high degree of consistency between the AT and ADCP measurements, further validating the accuracy of AT for measuring current velocities in complex ocean environments.

Li et al. (2017) successfully utilized AT to map the complex internal flow structure within a circular multidirectional wave/current basin. They divided the water column into five layers and estimated the layered current velocity by solving the regularized inverse problem. Notably, their AT results showed close agreement with measurements from an Acoustic Doppler Velocimeter (ADV), demonstrating the robustness of AT for measuring flow velocity.

Syamsudin et al. (2017) deployed two CAT devices in the Bali Strait, to measure the velocity and temperature of tidal currents across five vertical layers. Their results, when compared to data from an ADCP, showcased a high degree of agreement, demonstrating the accuracy and effectiveness of AT for measuring these parameters.

Syamsudin et al. (2019) employed the one-way AT in the Lombok Strait, to map the temperature profiles of internal solitary waves across four distinct layers. They compared their reconstructed temperatures with data from a Conductivity-Temperature-Depth (CTD) sensor, finding an excellent match between the AT and CTD measurements.

Huang et al. (2020) utilized CAT to measure high-resolution water temperature profiles across four layers within Thousand-Island Lake, Hangzhou, China. This technique, particularly relevant for environmental monitoring in the lake, achieved good agreement with the CTD data.

Taniguchi et al. (2021) investigated the effectiveness of AT in capturing high-frequency fluctuations in tidal currents. Their study successfully demonstrated agreement between AT's path-averaged current estimates and hourly ADCP data. Notably, AT was able to detect these fast variations which eluded the ADCP, highlighting its potential to enhance the reconstruction of velocity fields through inversion or data assimilation methods. These results show the high accuracy of AT and prove its feasibility for measuring tidal current velocity. Thus, no further comparison with the ADCP measurement is needed.

Kawanishi et al. (2015) pioneered the use of AT to assess tidal energy potential in the Nekosto Strait of Japan, with a maximum water depth of 100 meters. Their study estimated a peak flow velocity of 1 m/s across the strait, translating to a potential power output of 40 MW and an average power density of 0.5 kW/m². While this marked the first application of AT for calculating power density, the analysis exclusively focused on depth-averaged values, leaving room for future investigations into vertical variations in power potential.

This study uses AT to map vertical profiles of current velocity in the Persian Gulf, employing a regularized inverse problem to solve for velocity values. By analyzing these velocities, we can extract power density, a crucial parameter for identifying potential tidal energy sites. Our research distinguishes itself by calculating the layered power density (detailed in section 3.5). This innovative approach facilitates the determination of the optimal installation depth for tidal stream turbines, maximizing their energy extraction potential.

2. Material and Methods

2.1. Experimental settings

In this study, two 10 kHz CAT stations operating were deployed in the Persian Gulf, Iran (Figure 1a). Each station (S1 and S2) transmitted acoustic signals to its counterpart at 1-minute intervals, separated by a distance of 3 km and a depth of 6 meters from the water surface. Notably, the seabed exhibited a smooth topography with a consistent depth of 60 meters between the stations (Figure 1b). To complement the AT measurements, concurrent data on water temperature and salinity (CTD) was collected throughout the water column.

In noisy aquatic mediums such as gulfs, coasts, and shallow water of rivers, a particular method is required for transmitting and processing sound, which hinders signal attenuation. It has been proven that signal

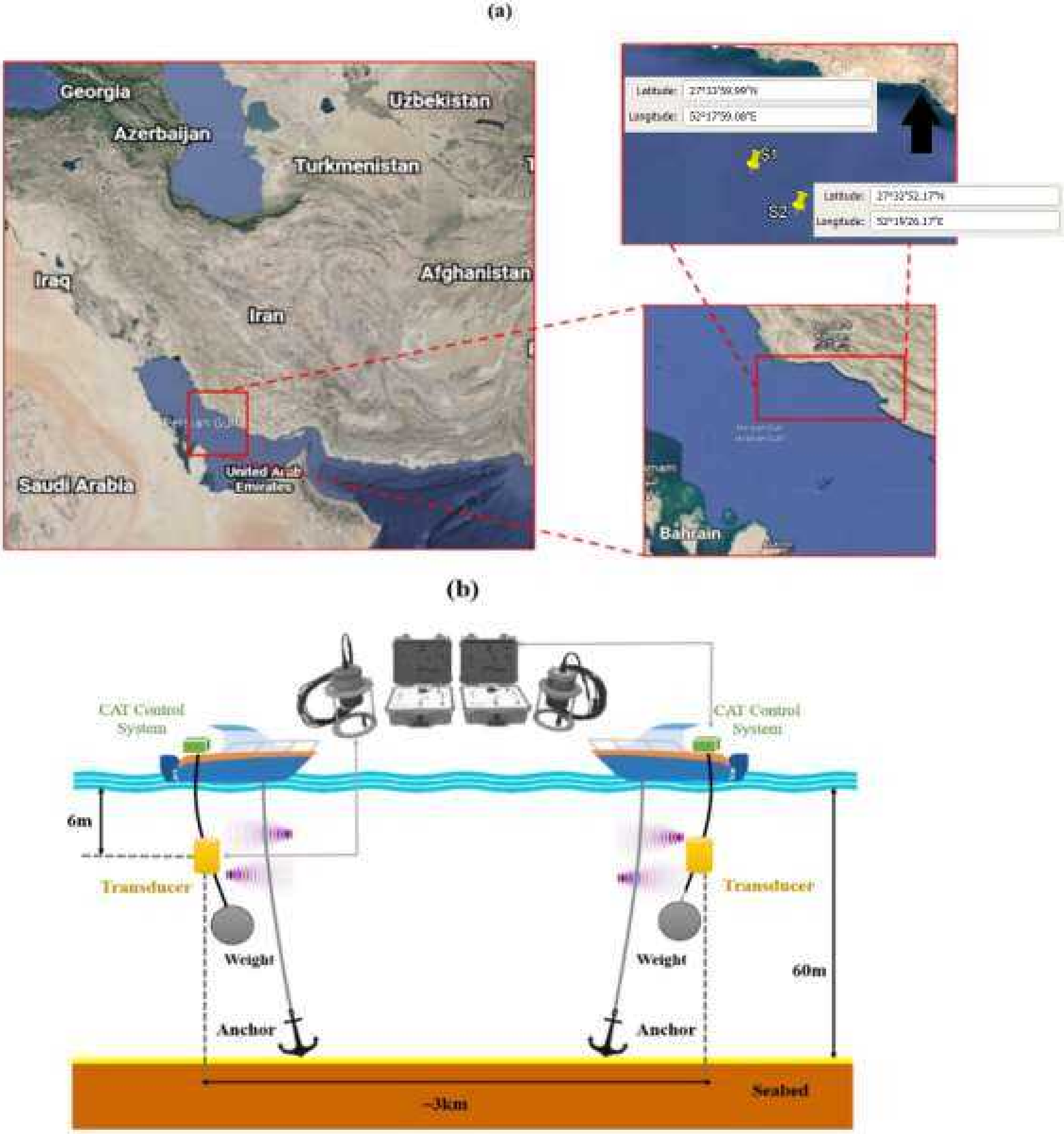

Figure 1. Sound transmission: (a) geographical location, and (b) schematic of the experimental arrangement and the components of a typical CAT system

modulation with an M-sequence and taking the cross-correlation of received signals is an efficient method (Bahreinimotlagh et al., 2020).

Table 1 shows the characteristics of M-sequence modulated signals that were transmitted reciprocally in this experiment.

Table 1. Characteristics of the reciprocal sound signals

M-sequence order	12
Carrier cycles per digit	1023
Source Level	190 dB re 1 μPa at 1 m

Examining the peak values in the correlation plots (also known as signal-to-noise ratio or SNR) reveals the arrival times of different acoustic rays. While the highest peak corresponds to the first ray, subsequent arrivals can be identified by analyzing smaller peaks within specific time windows after the initial peak. This process extracts both the arrival times and their corresponding travel times, essential for calculating range-averaged current values.

2.2. Range-independent ray simulation

Ray simulation, a fundamental step in the CAT implementation, utilizes the site-specific CTD data to theoretically model acoustic ray paths. In coastal environments, the ray-tracing method simulates sound propagation by considering only refraction using Snell's rule (Kaneko et al., 2020). In this study, we employed ray-tracing to simulate sound transmission between stations S1 and S2. Ray simulation provides the possible successfully transmitted rays (called Eigen rays), which are valuable in arrival peaks identification procedure and regularized inverse problem solution.

2.3. Range-averaged current (RAC) and lowpass filter

Considering a reciprocal sound transmission between two stations (S1→S2 and S2→S1) with a distance of L, the corresponding travel times t_1 and t_2 can be calculated by taking a path integral, as Eqs. 1 and 2 (Kaneko et al., 2020):

$$t_1 = \int_{\Gamma^+} \frac{ds}{C+v} \approx \frac{L}{C_m + V_m} \tag{1}$$

$$t_2 = \int_{\Gamma^-} \frac{ds}{C-v} \approx \frac{L}{C_m - V_m} \tag{2}$$

where $\Gamma^+$and $\Gamma^-$are the ray paths, ds is the arch length element along the refracted ray, C is the sound speed, and v is the current velocity. On the right side of the Eqs. 1 and 2, C_m and V_m represent the section-averaged sound speed and current velocity.

The range-averaged velocity, or more often referred to as range-averaged current (RAC), in the vertical cross-section of the two stations is calculated by solving Eqs. (1) and (2) which yields Eq. (3):

$$V_m = \frac{C_0^2}{2L} \Delta t \tag{3}$$

where $\Delta t = t_2 - t_1$, is the differential travel time, and C_0 is the reference sound speed.

The RAC time series often exhibits significant high-frequency components, which are seen as severe fluctuations. To address this issue, we implemented a 10-minute Blackman window low-pass filter, effectively smoothing the RAC time-series. Therefore, modified differential times were calculated using Eq. (4) to account for these filtering-induced changes."

$$\Delta t' = V_m' \frac{2L}{C_0^2} \tag{4}$$

where V_m' and $\Delta t'$ are the lowpass filtered range-averaged velocity and modified differential time, respectively.

2.4. Regularized inversion

In case M acoustic rays pass through N layers, the travel time of the i-th ray along and against the current (t_i^+ andt_i^-) equals to:

$$t_i^{\pm} = \sum_{i=1}^{N} \frac{l_{ij}}{(c_j \pm u_j)} \tag{5}$$

In Eq. (5) c_j is the path-averaged sound speed, u_j is the current velocity for the j-th layer, and l_{ij} is the arc length of the i-th ray passing through the j-th layer (Li, 2018). Since the current velocity is significantly smaller than the sound speed ($u \ll c$), the differential travel times (DTTs) can be formulated as Eq. (6), and it could be shown in its matrix notation (Eq. 7).

$$\Delta t_i = (t_i^+ - t_i^-) = -2 \sum_{i=1}^{N} \frac{l_{ij} u_j}{c_j^2} \tag{6}$$

$$\begin{bmatrix} \Delta t_1 \\ \Delta t_2 \\ \vdots \\ \Delta t_M \end{bmatrix} = \begin{bmatrix} -2\frac{l_{11}}{c_1^2} & -2\frac{l_{12}}{c_2^2} & \cdots & -2\frac{l_{1N}}{c_N^2} \\ -2\frac{l_{21}}{c_1^2} & -2\frac{l_{22}}{c_2^2} & \cdots & -2\frac{l_{2N}}{c_N^2} \\ \vdots & \vdots & \ddots & \vdots \\ -2\frac{l_{M1}}{c_1^2} & -2\frac{l_{M2}}{c_2^2} & \cdots & -2\frac{l_{MN}}{c_N^2} \end{bmatrix} \cdot \begin{bmatrix} u_1 \\ u_2 \\ \vdots \\ u_N \end{bmatrix} \tag{7}$$

Eq. (7) can be generalized as Eq. (8), in which y is the DTTs matrix, E is the coefficients matrix (sound speed and arc length of each ray in each layer), x is the layered current velocity matrix, and n is the error matrix.

$$y = Ex + n \tag{8}$$

There are several approaches to solve the inverse problem (Eq. 8). The classic algebra (least-squares) is not recommended for solving the acoustic tomography inverse problem, owing to the ill-posed nature of the problem, which leads to an unstable solution. To overcome the challenges associated with ill-posedness in the inverse problem, we employ a regularization technique (Eq. (9) and Figure 2). This approach effectively mitigates solution instability and yields an accurate and physically meaningful reconstruction of the current velocity field (Syamsudin et al., 2019).

$$\begin{aligned} J = n^T n + \lambda x^T H^T H x \\ = (y - Ex)^T (y - Ex) \\ + \lambda x^T H^T H x \end{aligned} \tag{9}$$

$$\hat{x} = (E^T E + \lambda H^T H)^{-1} E^T y \tag{10}$$

where λ is the Lagrange multiplier, and it is determined by minimizing the squared residuals considering a predetermined value. H is the regularization matrix, which is made from a second-order derivative operator $\frac{\partial^2 \mathrm{x}}{\partial \mathrm{z}^2}$.

This matrix is used to smooth the solution by applying a moving average to three consecutive layers (Syamsudin et al., 2017).

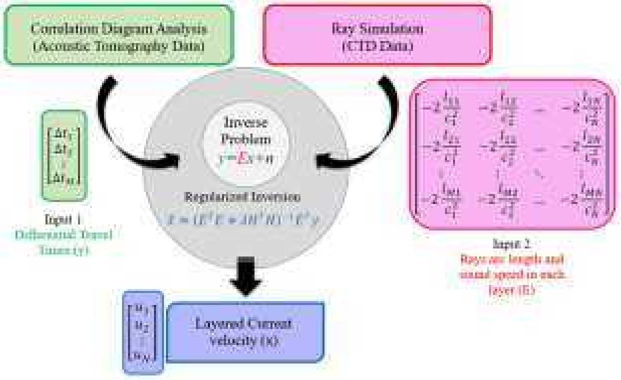

Figure 2. Components of a regularized inverse problem

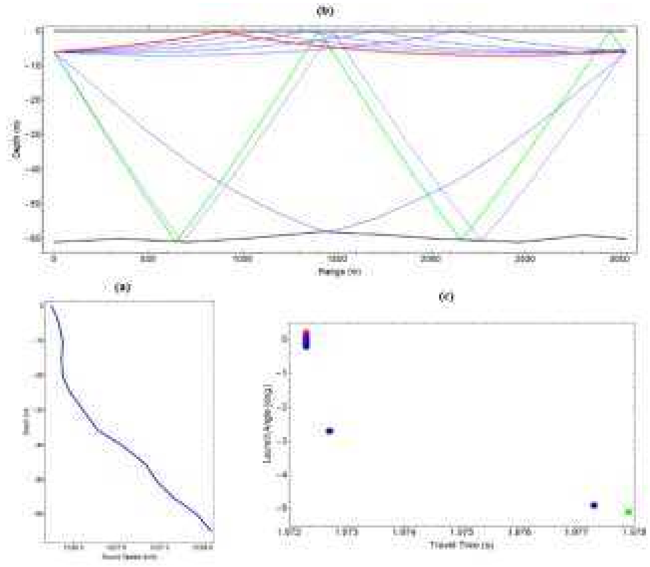

Figure 3. Results of the range-independent ray simulation: (a) Sound speed profile, (b) Transmitted Eigen rays between S1 and S2 (marked by red and green curves), (c) Rays travel times

$$\int_{-D}^{0}\left(\frac{\partial^2 x}{\partial z^2}\right)^2 dz=\sum_{i=1}^{M}(x_{i-1}-2x_i+x_{i+1})^2=x^T H^T H x \tag{11}$$

where D is the seabed depth. Considering 5 horizontal layers for a vertical slice, the regularization matrix is expressed by Eq. (12).

$$H=\begin{bmatrix}-2 & 1 & 0 & 0 & 0\\ 1 & -2 & 1 & 0 & 0\\ 0 & 1 & -2 & 1 & 0\\ 0 & 0 & 1 & -2 & 1\\ 0 & 0 & 0 & 1 & -2\end{bmatrix} \tag{12}$$

Inversion uncertainty is formulated as Eq. (13), where $\langle nn^T\rangle$ is the expected variance of differential travel times. Velocity inversion error can be estimated by Eq. (14).

$$P=(E^T E+\lambda H^T H)^{-1}E^T\langle nn^T\rangle E(E^T E+\lambda H^T H)^{-1} \tag{13}$$

$$V_{error}=diagonal(\sqrt{P_{\Delta t}}) \tag{14}$$

2.5. Power density

Power per unit area is called power density (PD) and calculated by Eq. (15), where ρ ($1025kg/m^3$) is the seawater density, and V is the current velocity.

$$PD=\frac{P}{A}=\frac{1}{2}\rho V^3 \tag{15}$$

3. Results and discussion

This section delves into the analysis of the AT data, divided into two key parts: (a) Processing and Interpretation: This covers ray simulation, arrival peak identification, range-averaged current calculation, and inversion results, and (b) Site Characterization: This focuses on assessing the site's velocity status through vertical profiles, velocity histograms, and power density estimation.

3.1. Ray simulation

Initially, the CTD data and Mackenzie's equation were used to calculate the sound speed profile. Then, the ray simulation was performed to determine the Eigen rays transmitted between two stations. The sound speed profile (Figure 3 a) exhibits slight change from the surface to the seabed. Regarding ray simulation results and correlation diagrams, two peaks are identified. These peaks correspond to the first (Ray 1, red-ray in Figure 3b) and second (Ray 2, green-ray in Figure 3b) Eigen rays, representing refracted surface-reflected (RSR) and surface-reflected bottom-reflected (SRBR) paths, respectively. Their reference travel times and ray arch lengths within each layer are summarized in Table 2.

3.2 Arrival peak identification

Signal processing of the raw AT data yielded correlation diagrams (travel time-SNR). Since two rays were successfully transmitted, we needed to identify two arrival peak points. The first peak was extracted using the largest peak method with an SNR threshold of 5. Ray simulation data (Table 2) predicted the second peak to occur about 5.5 ms later. Therefore, a 5-ms search window with a lower SNR threshold of 3 was used to identify the second peak (Figure 4a). Figure 4b presents the correlation diagrams and the identified peak points for both simultaneous signals.

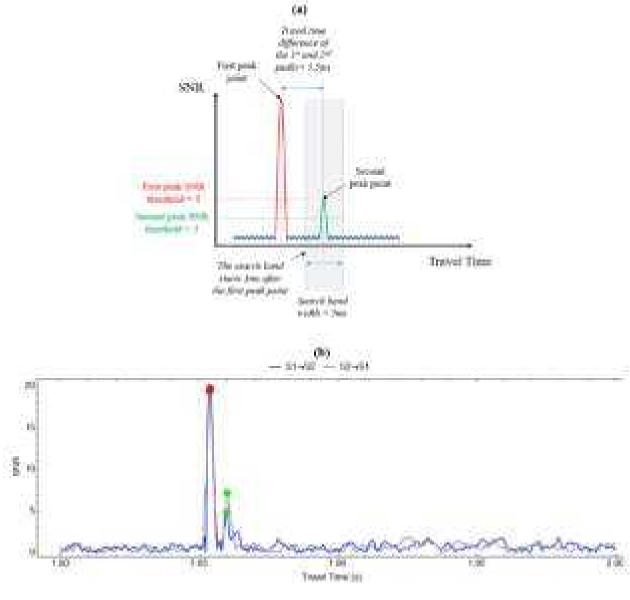

Figure 4. Arrival peak identification, (a) SNR thresholds and the search band, and (b) The correlation diagram of reciprocal sound transmission and the identified peaks

Table 2. Layered arch length and reference travel time of the transmitted eigen rays

Ray No.	Travel time	Ray length in: Layer 1	Layer 2	Layer 3	Layer 4	Layer 5
Ray 1 (RSR)	1.97231	3029.9	0	0	0	0
Ray 2 (SRBR)	1.9779	490.1	475.8886	480.0697	495.2206	1098.3

Applying the same procedure to the entire dataset generated a layered view of all correlation diagrams in Figure 5, where the first (red) and second (green) arrival peaks for each measurement are clearly marked. As expected, the first surface-reflected peaks exhibit higher SNR levels (15-20) due to minimal energy loss. In contrast, the second peaks, which involve multiple interactions with the seabed, show significantly lower SNR (5-10) due to signal strength. Additionally, Figures 5c and 5d reveal that the estimated ray travel times are consistently between 1.85 and 1.92 seconds.

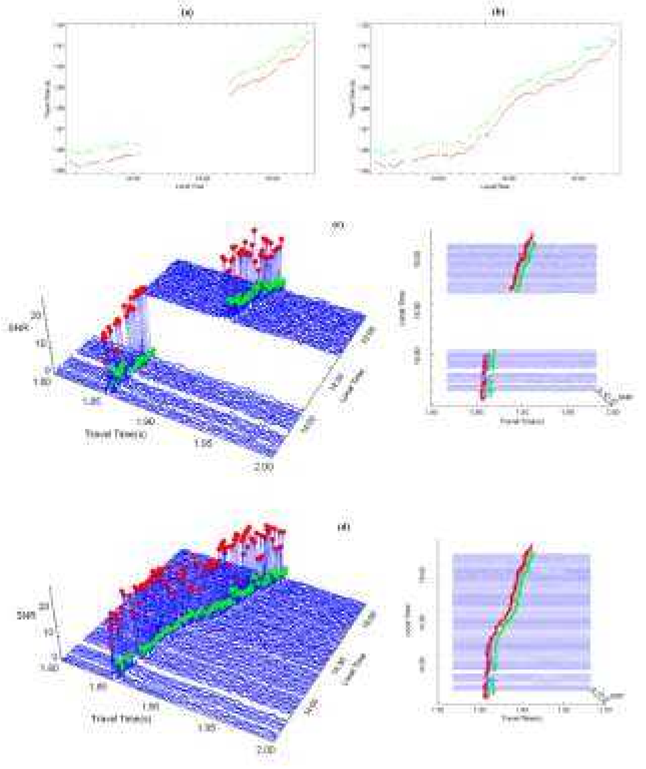

Figure 5. Stack plots of correlation diagrams with the 1st and 2nd peaks marked red and green respectively: (a) S1→S2, (b) S2→S1, and their corresponding travel

Figure 5a reveals a data gap between 14:03 and 14:40, corresponding to a loss of signals. This occurred due to a temporary battery malfunction in the CAT station during the experiment. We carefully evaluated the impact of this missing data and found it to have a negligible effect on the following calculations.

3.3 Range-averaged current (RAC)

Range-averaged current (RAC) values were calculated using Equation (3) based on the differential travel time between the first and second arrival peaks. A Blackman window low-pass filter with a 10-minute cutoff frequency was applied to smooth the RAC time series (red and green curves in Figure 6).

The RAC values reconstructed using the first and second peaks exhibit notable differences. This likely originates from the distinct paths traversed by each ray: the first exclusively within the first layer, while the second interacted with all five layers of the water column (Figure 7). This observation suggests a clear disparity between the surface current regime (layer 1) and the whole vertical slice current regime.

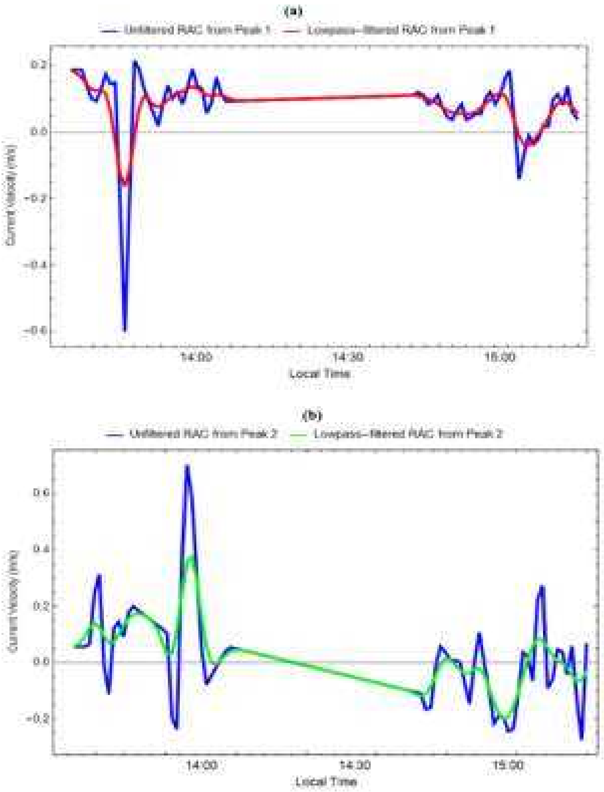

Figure 7. Current velocity calculated by regularized inversion: The highlighted regions show the before and after the battery malfunction time which were used to investigate the current histogram and power density in section 3.5

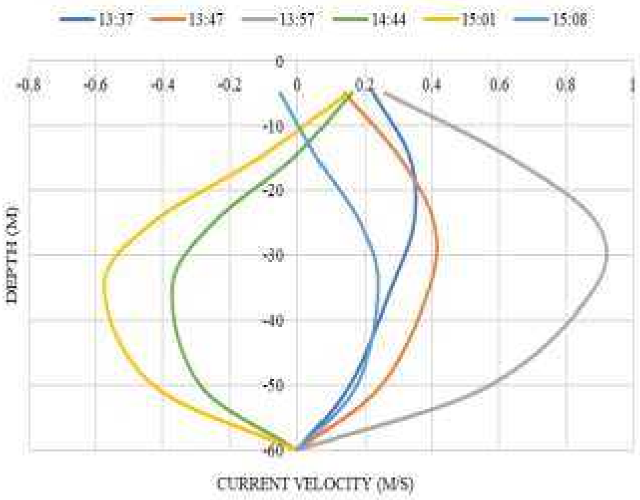

Figure 8. Current velocity vertical profiles in 6 different instants

3.4 Inversion results and current velocity profiles

Solving the regularized inverse problem with adjusted travel times and ray simulation data (Figure 3) revealed the current velocity distribution within five layers (0-10, 10-20, 20-30, 30-40, and 40-60 m) (solid lines in Figure 8). However, these velocity values must be corrected regarding the angle between the transmission line and the current dominant direction (α) which was estimated to be 54° in this research (Appendix).

The corrected velocity values are shown as dashed lines in Figure 8. The maximum current velocity of 0.89 m/s occurred in layer 3 at 13:57. At this specific time, the velocities in other layers were: 0.26 m/s (layer 1), 0.63 m/s (layer 2), 0.88 m/s (layer 4), and 0.57 m/s (layer 5). Table 3 presents the inversion error for each layer. Analyzing these values alongside the range of velocities observed in the data, we can confidently conclude that the inversion error is negligible, indicating robust and accurate velocity estimation.

Figure 9 clearly reveals that layers 3 and 4 have the most potential for exhibiting significantly higher velocity values compared to the other layers. To quantify the similarity in velocity behavior across layers, we calculated the Root Mean Squared Error (RMSE) of the velocity time series for each layer pair (Table 4). This analysis reveals a particularly low RMSE of 0.08 between layers 3 and 4, indicating that their velocity profiles are nearly identical.

”

3.5 Velocity histogram and Power density (PD)

Focusing on layers 3 and 4, we analyzed only the highlighted sections in Figure 8 to gain clearer insights into the site's typical current velocity status and power density values. The sign of velocity (+ or -) indicates the current direction, but since it is not of high importance, the absolute value of velocities was taken into account.

The velocity histogram (Figure 9 a) shows that the site predominantly experiences current speeds between 0.1 and 0.5 m/s. Sites with practical current velocities greater than 1 m/s are economically viable, but the current in this site during the experiment does not satisfy this limit. Therefore, this site likely wouldn't support sufficient power generation for in-stream tidal turbines. This conclusion aligns with the power density (PD) analysis. While peak PD values reach 350 and 100 W/m² in sections A and B (Figure 9b and 9c), respectively, the average PD remains significantly lower at 42 and 14 W/m², respectively.

These findings emphasize the importance of extended measurement periods to capture temporal variations in current velocity and considering more efficient tidal energy conversion systems, such as tidal kites developed by Minesto. It is also claimed that due to the moving nature of this energy conversion method, the current velocity can increase up to ten times (Roberts et al., 2016). The tidal kite system operates typically at mid-depth. Often described as a "flying" kite with a turbine and generator attached underneath, it traces a lying figure-eight path nearly perpendicular to the tidal flow.

This paper and the research conducted by (Kawanishi et al., 2015) indicate the capability of the AT technique in measuring power density for tidal energy potential assessment. However, the calculation of layered power density in this paper enables us to determine the best installation depth for tidal stream turbines.

4. Conclusion

Utilizing two 10-kHz CAT stations, this study assessed the tidal stream energy potential in the Persian Gulf, Iran, by mapping velocity and energy profiles through the regularized inverse problem. Reciprocally transmitted acoustic rays with measured arrival times were used to calculate range-averaged current (RAC) values, crucial for assessing tidal stream energy potential. Differences in RAC values between rays 1 and 2, likely due to distinct travel paths, necessitated smoothing the time series with a low-pass filter. This smoothed data then served as input for the regularized inverse problem, enabling the reconstruction of velocity profiles within a 5-layer vertical slice.

Layer 3 experienced the maximum velocity with a value of 0.89 m/s. The accurate evaluation of velocity profiles and considering RMSE between layers indicated that layers 3 and 4 are very similar and have a higher potential than others.

Further analysis of the velocity regime, using velocity histograms and power density (PD) diagrams, indicated that this site is not economically viable for the chosen tidal energy conversion method. This suggests the need for further experimentation and exploration of more efficient technologies, such as tidal kites.

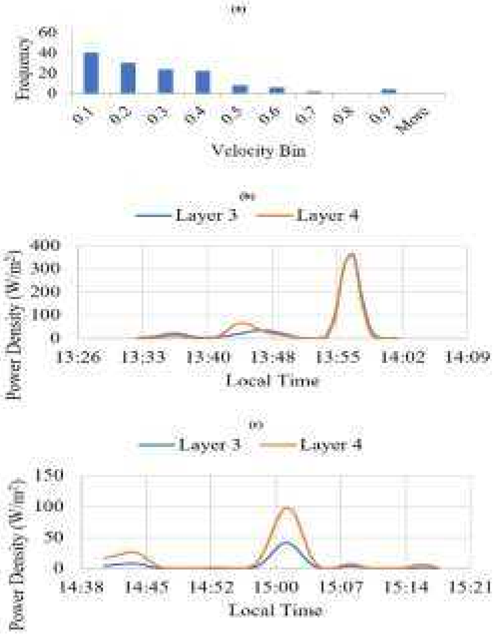

Figure 9. Site velocity histogram and PD: (a) velocity histogram for layers 3 and 4, (b) PD for layers 3 and 4 in time section A, and (c) PD for layers 3 and 4 in time section B.

Declaration of competing interest

The authors declare that they have no known competing financial interests or personal relationships that could have appeared to influence the work reported in this paper.

Acknowledgment

The authors would like to thank Dr. Noriaki Gohda and Prof. Arata Kaneko of Hiroshima University/Aqua Environmental Monitoring Limited Liability Partnership (AEM- LLP) for their strong support in constructing the CAT system.

Funding: This study was funded by Infrasound Research Laboratory (IRL) through grant No. IRL-TMO-1-202.

References

Bahaj, A. S. (2013). Marine current energy conversion: the dawn of a new era in electricity production. *Philosophical Transactions of the Royal Society A: Mathematical, Physical and Engineering Sciences*, *371*(1985), 20120500. https://doi.org/10.1098/rsta.2012.0500

Bahreinimotlagh, M., Kawanisi, K., Kavousi, A., Roozbahani, R., & Abbasi, M. (2020). Influence of Suspended Sediment Concentration and Particle Sizes on the Sound Attenuation of the Fluvial Acoustic Tomography Technique. *Journal of Water and Environment Technology*, *18*(5), 338–348. https://doi.org/10.2965/jwet.20-024

Gunawan, B., Neary, V. S., & Colby, J. (2014). Tidal energy site resource assessment in the East River tidal strait, near Roosevelt Island, New York, New York. *Renewable Energy*, *71*, 509–517. https://doi.org/10.1016/j.renene.2014.06.002

Huang, H., Guo, Y., Li, G., Arata, K., Xie, X., & Xu, P. (2020). Short-range water temperature profiling in a lake with coastal acoustic tomography. *Sensors (Switzerland)*, *20*(16), 1–14. https://doi.org/10.3390/s20164498

Jahromi, M. S. (2024). Tidal components along the north of Oman Gulf and Persian Gulf. *International Journal of Coastal, Offshore and Environmental Engineering*, *8*(4), 36–48.

Kaneko, A., Zhu, X.-H., & Lin, J. (2020). Coastal Acoustic Tomography. In *Elsevier*. Elsevier. https://doi.org/10.1016/B978-0-12-818507-0.00005-6

Kawanishi, K., BahrainiMotlagh, M., & Razaz, M. (2015). Energy flux measurement of tidal stream in a strait using two crossing ultrasonic transmission lines. *36th World Congress of the International Association of Hydro-Environment Engineering and Research (IAHR-APD 2015)*, 1–4.

khoshkholgh, A. (2023). Applying and Assessing the Performance of Projection Method in External Mode of Princeton Ocean Model by Simulating Tidal Currents in the Persian Gulf. *International Journal Of Coastal, Offshore And Environmental Engineering(Ijcoe)*, *8*(3), 22–31. https://doi.org/10.22034/ijcoe.2023.399301.1033

Li, G. (2018). *Flow velocity mapping in a circular experimental wave / current basin with small scale underwater acoustic tomography method* (Issue June). University of Edinburgh.

Li, G., Ingram, D., Kaneko, A., Chen, M., Gohda, N., & Polydorides, N. (2017). Vertical underwater acoustic tomography in an experimental basin. *The Journal of the Acoustical Society of America*, *141*(5), 3656–3656. https://doi.org/10.1121/1.4987918

Radfar, S., Panahi, R., Javaherchi, T., Filom, S., & Mazyaki, A. R. (2017). A comprehensive insight into tidal stream energy farms in Iran. In *Renewable and Sustainable Energy Reviews* (Vol. 79, pp. 323–338). Elsevier Ltd. https://doi.org/10.1016/j.rser.2017.05.037

Roberts, A., Thomas, B., Sewell, P., Khan, Z., Balmain, S., & Gillman, J. (2016). Current tidal power technologies and their suitability for applications in coastal and marine areas. *Journal of Ocean Engineering and Marine Energy*, *2*(2), 227–245. https://doi.org/10.1007/s40722-016-0044-8

Sellar, B., & Wakelam, G. (2018). Characterisation of Tidal Flows at the European Marine Energy Centre in the Absence of Ocean Waves. *Energies*, *11*(1), 176. https://doi.org/10.3390/en11010176

Syamsudin, F., Chen, M., Kaneko, A., Adityawarman, Y., Zheng, H., Mutsuda, H., Hanifa, A. D., Zhang, C., Auger, G., Wells, J. C., & Zhu, X. (2017). Profiling measurement of internal tides in Bali Strait by reciprocal sound transmission. *Acoustical Science and Technology*, *38*(5), 246–253. https://doi.org/10.1250/ast.38.246

Syamsudin, F., Taniguchi, N., Zhang, C., Hanifa, A. D., Li, G., Chen, M., Mutsuda, H., Zhu, Z., Zhu, X., Nagai, T., & Kaneko, A. (2019). Observing Internal Solitary Waves in the Lombok Strait by Coastal Acoustic Tomography. *Geophysical Research Letters*, *46*(17–18), 10475–10483. https://doi.org/10.1029/2019gl084595

Taniguchi, N., Huang, C.-F., Kaneko, A., Liu, C.-T., Howe, B. M., Wang, Y.-H., Yang, Y., Lin, J., Zhu, X.-H., & Gohda, N. (2013). Measuring the Kuroshio Current with ocean acoustic tomography. *The Journal of the Acoustical Society of America*, *134*(4), 3272–3281. https://doi.org/10.1121/1.4818842

Taniguchi, N., Takahashi, T., Yoshiki, K., Yamamoto, H., Hanifa, A. D., Sakuno, Y., Mutsuda, H., Huang, S. W., Huang, C. F., & Guo, J. H. (2021). A reciprocal acoustic transmission experiment for precise observations of tidal currents in a shallow sea. *Ocean Engineering*, *219*(June), 108292. https://doi.org/10.1016/j.oceaneng.2020.108292

Thiébaut, M., Filipot, J.-F., Maisondieu, C., Damblans, G., Jochum, C., Kilcher, L. F., & Guillou, S. (2020). Characterization of the vertical evolution of the three-dimensional turbulence for fatigue design of tidal turbines. *Philosophical Transactions of the Royal Society A: Mathematical, Physical and Engineering Sciences*, *378*(2178), 20190495. https://doi.org/10.1098/rsta.2019.0495

INTERNATIONAL JOURNAL OF
COASTAL, OFFSHORE & ENVIRONMENTAL ENGINEERING

IJCOE Vol. 10 / No. 2 / Spring 2025 (16-34)

Available online at: www.ijcoe.org

Probability density functions of the DoB in tubular KT-joints of jacket-type platforms under out-of-plane bending loads

Hamid Ahmadi*[,1], Esmaeil Zavvar[2], Vahid Mayeli[3]

[1] *National Centre for Maritime Engineering and Hydrodynamics, Australian Maritime College (AMC), University of Tasmania, Launceston, TAS 7248, Australia.*

[2] *Department of Civil Engineering, Faculty of Engineering, University of Porto, Porto, Portugal.*

[3] *Faculty of Civil Engineering, University of Tabriz, Tabriz 5166616471, Iran.*

*Corresponding Author

E-mail Addresses: hamid.ahmadi@utas.edu.au (H. Ahmadi); esmaeilzavvar@gmail.com (E. Zavvar); mayeli.vahid@gmail.com (V. Mayeli)

ARTICLE INFO

Article History:
Received: 11 Mar 2024
Accepted: 03 Jul 2025

Keywords:
Tubular KT-joint; Fatigue; Degree of bending (DoB); Out-of-plane bending (OPB) moment loading; Probability density function (PDF); Weibull distribution; Kolmogorov-Smirnov test.

ABSTRACT

The degree of bending (DoB) has a profound effect on the fatigue behavior of tubular joints commonly found in offshore jacket structures. The DoB characterizes the through-the-thickness stress distribution and its value is essential for improving the accuracy of fatigue life estimation. Probability density functions (PDFs) of the random variables involved are necessary for the fatigue reliability analysis of jacket structures. The objective of present research was the derivation of PDF for the DoB in tubular KT-joints commonly found in jacket-type platforms. A total of 243 finite element (FE) analyses were carried out on 81 FE models of KT-joints subjected to three types of out-of-plane bending (OPB) moment loading. Generated FE models were validated using experimental data, previous FE results, and available parametric equations. Based on the results of parametric FE study, a sample database was prepared for the DoB values and density histograms were generated for respective samples based on the Freedman-Diaconis rule. Thirteen theoretical PDFs were fitted to the developed histograms, and the maximum likelihood (ML) method was applied to evaluate the parameters of fitted PDFs. In each case, the Kolmogorov-Smirnov test was used to evaluate the goodness of fit. Finally, the Weibull model was proposed as the governing probability distribution function for the DoB. After substituting the values of estimated parameters, six fully defined PDFs were presented for the DoB at the saddle positions of central and outer braces in KT-joints subjected to three types of OPB moment loading.

1. Introduction

Jacket-type offshore platforms widely used for oil/gas production primarily consist of circular hollow section (CHS) members, also called tubulars. The intersection among tubulars, in which the prepared ends of branch members (braces) are welded onto the undisturbed surface of a main member (chord), is called a tubular joint (Fig. 1). As a result of the formation and propagation of cracks due to wave-induced cyclic loads, tubular joints are susceptible to fatigue-induced damage during their service life.

One of the widely accepted approaches to estimate the fatigue life of a tubular joint is the stress-life (S-N) method that is based on the hot-spot stress (HSS) calculation. However, the study of many fatigue test results has shown that tubular joints of different geometry or loading type but with similar HSSs often exhibit significantly different numbers of cycles to failure [1]. Such differences are thought to be attributable to changes in crack growth rate that is dependent on the through-the-thickness stress distribution which can be characterized by the degree of bending (DoB) defined as the ratio of bending stress to total external stress.

Fig. 2 depicts the typical stress distribution through the chord wall of a tubular joint. Through-the-thickness stress field is a combination of the linear stress due to the chord wall bending and the nonlinear stress concentration at the weld toe due to the section change at the intersection. The nonlinear stress distribution around the weld toe is dependent on the weld geometry and is difficult to predict during the design stage. Since for a deep crack, the weld-toe stress concentration has a relatively little effect on the through-the-thickness stress field [2], the stress distribution across the wall thickness is usually assumed to be a linear combination of membrane and bending stresses. Hence, the DoB can be expressed as:

$$\mathrm{DoB} = \frac{\sigma_B}{\sigma_T} = \frac{\sigma_B}{\sigma_B + \sigma_M} \qquad (1)$$

where σ_T is the total stress; and σ_B and σ_M are the bending and membrane stress components, respectively.

For the joints with low DoB, the standard stress-life approach may be unconservative. Hence, the current standard HSS-based S-N approach can be modified to include the effect of DoB in order to obtain more accurate fatigue life prediction. The other shortcoming of the S-N approach is that this method gives only the total life and can not be used to predict the fatigue crack growth and the remaining life of cracked joints. For the fatigue analysis of cracked joints, fracture mechanics (FM) should be used. The accurate determination of a stress intensity factor (SIF) is the key for FM calculations. Owing to the complexities introduced by the structural geometry and the nature of the local stress fields, it is impossible to calculate the SIFs analytically. This problem is often tackled by using simplified models, such as the flat plate solution and methods based on the T-Butt weight function with an appropriate load shedding model. To use these simplified SIF models to calculate the remaining fatigue life of tubular joints, the information is required again on the distribution of through-the-thickness stress acting on the anticipated crack path, which can be characterized by the DoB. Thus, DoB is an important input parameter for the calculation of fatigue crack growth in tubular welded joints.

Under any specific loading condition, the DoB value along the weld toe of a tubular joint is mainly determined by the joint geometry. To study the behavior of a tubular joint and to easily relate this behavior to the geometrical characteristics of the joint, a set of dimensionless geometrical parameters has been defined. Fig. 1 depicts a tubular KT-joint with the geometrical parameters τ, γ, β, α, and α_B for chord and brace diameters: D and d, and their corresponding wall thicknesses: T and t, and lengths: L and l. Critical positions along the weld toe of the central and outer braces for the calculation of the DoB values in a tubular joint, i.e. saddle, crown, toe, and heel have been shown in Fig. 1.

Since 1990s, a few research works has been devoted to the study of the DoB in simple tubular connections such as X- and K-joints. However, for tubular joints with complex geometry such as KT-joints which are quite common in offshore structures, the DoB has not been comprehensively investigated.

In a deterministic fatigue analysis, limiting assumptions should be made on numerous input parameters some of which exhibit considerable scatter. Consequently, deterministic analyses usually result in conservative designs. This fact emphasizes the significance of reliability-based fatigue analysis and design methods in which the key parameters of the problem can be modeled as random variables. The fundamentals of fatigue reliability assessment, if properly applied, can provide immense insight into the fatigue performance and safety of the structural system. Regardless of the method used for the reliability-based fatigue analysis and design of offshore structures, the probabilistic and statistical measures of the DoB are required as input parameters. DoB shows considerable scatter highlighting the significance of deriving its governing probability distribution function.

In the present research, initially, available literature on the DoB was surveyed (Sect. 2). Afterwards, a total of 243 finite element (FE) analyses were carried out on 81 FE models of tubular KT-joints which are among the most common joint types in jacket-type oil/gas production platforms. FE analyses were conducted under three types of out-of-plane bending (OPB) loads as shown in Fig. 3. Generated FE models were validated using the existing experimental data, FE results, and parametric equations. Based on a parametric FE investigation, a sample database was created for the DoB (Sect. 3); and density histograms were generated for respective samples (Sect. 4). Thirteen theoretical PDFs were fitted to the developed histograms, and the maximum likelihood (ML) method was applied to evaluate the parameters of fitted PDFs (Sect. 5). In each case, the Kolmogorov-Smirnov test was used to assess the goodness of fit (Sect. 6). Finally, a probability distribution model was proposed for the DoB; and after substituting the values of estimated parameters, six fully defined PDFs were presented for the DoB at the saddle positions of the central and outer braces in tubular KT-joints subjected to three types of OPB moment loading (Sect. 7).

2. Literature survey

2.1. Deterministic analysis of the DoB

Morgan and Lee [3] derived mean and design equations for DoB values at critical positions in axially loaded tubular K-joints from a previously established FE database of 254 joints. Design equations met all the acceptance criteria recommended by the UK DoE [4].

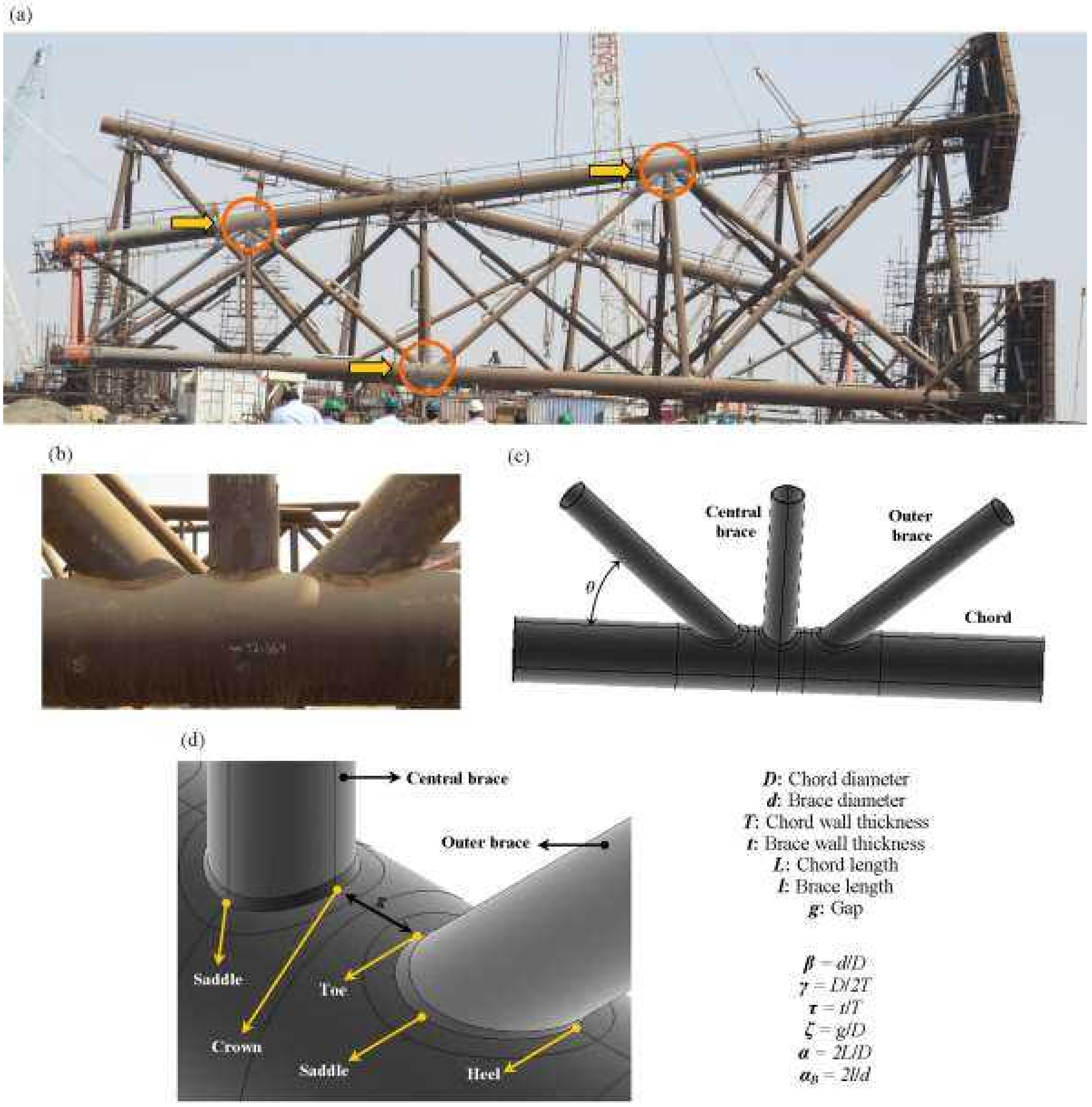

Fig. 1. (a) Tubular KT-joints in a jacket structure during the fabrication, (b) Close view of a welded tubular KT-joint, (c) Geometrical notation for a tubular KT-joint, (d) Critical positions along the weld toe of central and outer braces

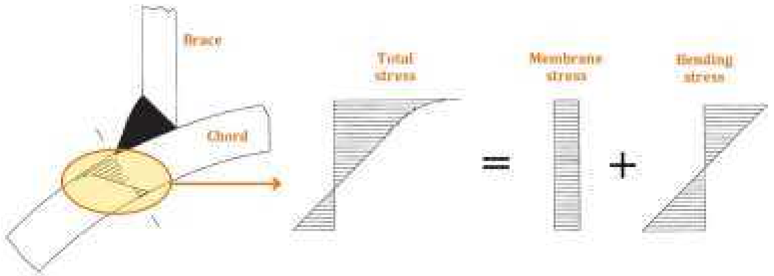

Fig. 2. Through-the-thickness stress distribution in a tubular joint

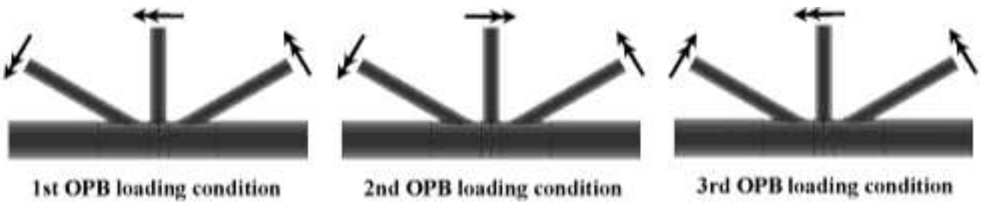

Fig. 3. Three applied OPB moment loading conditions

Chang and Dover [2] carried out a series of systematic thin-shell FE analyses for 330 tubular X- and DT-joints typically found in offshore structures under six different types of loading. Based on the results of nearly 2000 FE analyses, a set of parametric equations was developed to calculate the DoB at critical positions. Lee and Bowness [5] proposed an engineering methodology for estimating SIF solutions for semi-elliptical weld-toe cracks in tubular joints. The methodology uses the T-butt solutions proposed previously by the authors in conjunction with the stress concentration factors (SCFs) and the DoB values in uncracked tubular joints. Shen and Choo [6] determined the SIFs for a grouted tubular joint. They found that the fatigue strength of a grouted joint may be lower than that of as-welded joint, because when normalized with the HSS, the shape factor of grouted joint is higher than that of original as-welded joint due to the reduction in the DoB caused by the presence of in-filled grout in the chord. For grouted tubular joints, it is essential to consider the effect of DoB in practical fatigue assessment using HSS approach.

Ahmadi et al. [7] performed a set of parametric stress analyses on 81 K-joint FE models subjected to two different types of in-plane bending (IPB) loads. Analysis results were used to present general remarks on the effect of geometrical parameters on the DoB values at the toe and heel positions; and a new set of DoB parametric equations was developed. Ahmadi and Asoodeh [8] analyzed 81 K-joint FE models subjected to two types of OPB loading. Results were used to study the geometrical effects on the DoB at the saddle position; and two new DoB design formulas were proposed. Ahmadi and Asoodeh [9] studied the DoB in uniplanar tubular KT-joints subjected to axial loads. Their study was limited to the central brace DoB values and no design equation was proposed for the DoB along the weld toe of the outer braces. Also, IPB and OPB loadings were not included. Ahmadi and Amini Niaki [10] studied the degree of bending in two-planar tubular DT-joints under axial and bending loads. They developed a set of parametric equations to predict the DoB values at the saddle and crown positions.

2.2. Probabilistic analysis of the DoB

Ahmadi and Ghaffari [11] proposed a set of probability density functions for the DoB in tubular X-joints subjected to bending loads. Ahmadi and Ghaffari [12] developed probability distribution models for the DoB and SIF values in axially loaded tubular K-joints.

2.3. Remarks

Based on the above discussion, it is concluded that:

1. Despite the comprehensive research carried out on the study of SCFs and SIFs in tubular joints (e.g. [13-24] for SCFs, and [25, 26] for SIFs, among many others), the research works on the DoB in tubular joints are scarce and the studied joint types are limited to simple connections. Although tubular KT-joints are commonly found in steel offshore structures, the DoB in such joints has not been comprehensively investigated.
2. Results of research work reported in the literature are mostly suitable for deterministic analyses; and probabilistic studies are only limited to K- and X-joints. No probabilistic investigation has been carried out on the DoB of KT-joints; and there is no probability density function available for the DoB values to be used in reliability-based fatigue analysis and design of this type of joint.

3. Preparation of the DoB sample database

3.1. Details of FE modeling and analysis

FE-based software package ANSYS Ver. 11 was used in the present research for the FE modeling and analysis of tubular KT-joints subjected to OPB loadings in order to extract the DoB values for the probabilistic study.

3.1.1. Modeling of the weld profile

Accurate modeling of the weld profile is one of the important factors affecting the accuracy of the DoB results. In the present research, the welding size along the brace-to-chord intersection satisfies the AWS D 1.1 [27] specifications. The weld sizes at the crown, saddle, toe, and heel positions can be determined as follows:

$$
\begin{aligned}
& H_w(\text{mm}) = 0.85t(\text{mm}) + 4.24 \\
& L_w = \frac{t}{2}\left[\frac{135^\circ - \psi\ (\text{deg.})}{45^\circ}\right] \\
& \psi = \begin{cases} 90^\circ & \text{Crown} \\ 180^\circ - \cos^{-1}\beta\ (\text{deg.}) & \text{Saddle} \\ 180^\circ - \theta\ (\text{deg.}) & \text{Toe} \\ \theta\ (\text{deg.}) & \text{Heel} \end{cases}
\end{aligned}
\qquad (2)
$$

The parameters used in Eq. (2) are defined in Fig. 4. As an example, the weld profiles generated for the central and outer braces of the joint model SKTJ1 ($\alpha = 16$, $\alpha_B = 8$, $\zeta = 0.3$, $\tau = 0.4$, $\beta = 0.4$, $\gamma = 12$, $\theta = 30^\circ$) are shown in Fig. 5. For details of the weld profile modeling according to AWS D 1.1 [27], the reader is referred to Lie et al. [28] and Ahmadi et al. [29].

3.1.2. Definition of boundary conditions

The chord end fixity conditions in offshore tubular joints may range from almost fixed to almost pinned with generally being closer to almost fixed [30]. In practice, the value of the parameter α in over 60% of tubular joints is more than 20 and it is bigger than 40 in 35% of the joints [31]. Changing the end restraint from fixed to pinned results in a maximum increase of 15% in the HSS at crown position for the joints with $\alpha = 6$; and this increase reduces to only 8% for $\alpha = 8$ [3]. In the view of the fact that the effect of chord end restraints is only significant for joints with $\alpha < 8$ and high β and γ values, which do not commonly occur in practice, both chord ends were assumed to be fixed, with the corresponding nodes restrained.

Under each of the three considered loading conditions, only an appropriate portion of the entire tubular KT-joint is required to be modeled. The reason is the symmetry in geometry, material properties, and chord-end boundary conditions of the joint, as well as loading symmetry/antisymmetry. This allowed us to consider a reduced FE problem instead of the actual one. Thus, the order of the global stiffness matrix and total number of stiffness equations were reduced, and computer solution time was substantially decreased. Table 1 and Fig. 6 describe the required portion to be modeled for each load case. Appropriate symmetric/antisymmetric boundary conditions were defined for the nodes located on the symmetry/antisymmetry planes.

3.1.3. Generation of the FE mesh

ANSYS element type SOLID95 was used in present research to model the chord, braces, and the weld profiles. These elements have compatible displacements and are well-suited to model curved boundaries. The element is defined by 20 nodes having three degrees of freedom per node and may have any spatial orientation. Using this type of 3-D brick elements, the weld profile can be modeled as a sharp notch. This method will produce more accurate and detailed stress distribution near the intersection in comparison with a shell analysis.

To guarantee the mesh quality, a sub-zone mesh generation method was used during the FE modeling. In this method, the tubular KT-joint was divided into several sub-zones according to computational requirements. The mesh of each sub-zone was then generated separately, and the meshing of the joint was finally completed by merging the meshes of the sub-zones. Quality and quantity of the mesh can be feasibly controlled by this method, and badly distorted elements can be avoided. The mesh generated by this method for a tubular KT-joint is shown in Fig. 7.

In the present paper, nodal stresses were used to extract the HSSs. When ANSYS solves stress, it does so on an element-by-element basis. Unless otherwise prompted, ANSYS will solve for the stresses at the Gauss points and extrapolate to the nodes. However, many elements share nodes. Thus, ANSYS averages the nodal stresses computed from each of the adjacent elements. If the mesh is sufficiently small, the averaged stresses will not be very different from the un-averaged stresses. In fact, there will be no big difference among stresses at a common node computed from adjacent elements. Hence, if one observes in the plot of un-averaged stresses that the stress changes drastically from a specific element to the next one, the generated mesh is not small enough. In the present research, the mesh generated for the critical zones such as the extrapolation region was sufficiently fine to avoid such problems.

It is explained in Sect. 3.1.4 that the geometric stresses perpendicular to the weld toe are required to be calculated to determine the DoB at the weld toe position based on Eq. (1). As shown in Fig. 8a, to extract the geometric stresses perpendicular to the weld toe, the region near the weld toe was meshed finely. The width of this region is discussed in Sect. 3.1.4.

To make sure that the results of the FE analysis are not affected by the inadequate quality or the size of the generated mesh, convergence test was conducted and meshes with different densities were used in this test, before generating the 81 models. Based on the results of convergence test, the number of elements through the chord and brace thickness was 2 (Fig. 8b); the number of elements on the surface, base, and back of the weld profile was 2 (Fig. 8c); the number of elements along the ½ of entire brace-to-chord intersection was selected to be 10 and 15 for the central and outer braces, respectively (Fig. 8d); and the number of elements inside the extrapolation region was selected to be 16 (Fig. 8a).

3.1.4. Analysis and extraction of DoB values

To obtain the DoB values in a tubular joint, static analysis of the linearly elastic type is suitable. The Young’s modulus and Poisson’s ratio were taken to be 207 GPa and 0.3, respectively.

To determine the weld-toe DoB values, according to Eq. (1), bending and membrane stress components should be known. These components can be calculated as follows:

$$\sigma_B = \frac{\sigma_O - \sigma_I}{2} \tag{3}$$

$$\sigma_M = \frac{\sigma_O + \sigma_I}{2} \tag{4}$$

where σ_O and σ_I are the hot-spot stresses (HSSs) at the weld toe on the outer and inner surfaces of the chord, respectively.

Eqs. (1), (3), and (4) lead to the following relation for the DoB based on the HSSs:

$$\mathrm{DoB} = \frac{1}{2}\left(1 - \frac{\sigma_I}{\sigma_O}\right) \tag{5}$$

To determine the HSSs, the stress at the weld-toe position should be extracted from the stress field outside the region influenced by the local weld-toe geometry. The location from which the stresses have to be extrapolated, called extrapolation region, depends on the dimensions of the joint and on the position along the intersection. According to the recommendations of IIW-XV-E [32], the first extrapolation point should be at a distance of 0.4*T* from the weld toe, and the second point must be 1.0*T* further from the first point (Fig. 9a). The HSS is obtained by the linear extrapolation of the geometric stresses at these two points to the weld toe.

To extract and extrapolate the stresses perpendicular to the weld toe, as shown in Fig. 8a, the region between the weld toe and the second extrapolation point was meshed in such a way that each extrapolation point was placed between two nodes located in its immediate vicinity. These nodes are located on the element-generated lines which are perpendicular to the weld toe ($X_{\perp}$ direction in Fig. 9b).

At an arbitrary node inside the extrapolation region, the stress component in the direction perpendicular to the weld toe can be calculated, through the transformation of primary stresses in the global coordinate system, using the following equation:

$$\sigma_{\perp N} = \sigma_x {l_1}^2 + \sigma_y {m_1}^2 + \sigma_z {n_1}^2 + 2\left(\tau_{xy} l_1 m_1 + \tau_{yz} m_1 n_1 + \tau_{zx} n_1 l_1\right) \tag{6}$$

where σ_a and τ_{ab} $(a, b = x, y, z)$ are components of the stress tensor which can be extracted from ANSYS analysis results; and l_1, m_1, and n_1 are transformation components.

At the saddle, crown, toe, and heel positions, Eq. (6) is simplified as:

$$\sigma_{\perp N} = \sigma_x {l_1}^2 + \sigma_y {m_1}^2 + 2\tau_{xy} l_1 m_1 \quad \text{(Saddle)} \quad ;$$
$$\sigma_{\perp N} = \sigma_z \quad \text{(Crown, Toe, and Heel)} \tag{7}$$

Transformation components can be obtained as follows:

$$l_1 = \cos\left(X_{\perp}, x\right) = \left(x_w - x_n\right) / \delta \ ;$$
$$m_1 = \cos\left(X_{\perp}, y\right) = \left(y_w - y_n\right) / \delta \tag{8}$$

$$\delta = \sqrt{\left(x_w - x_n\right)^2 + \left(y_w - y_n\right)^2 + \left(z_w - z_n\right)^2} \tag{9}$$

where $X_{\perp}$ is the direction perpendicular to the weld toe (Fig. 9b); *x*, *y*, and *z* are the axes of global Cartesian coordinate system; (x_n , y_n , z_n) and (x_w , y_w , z_w) are coordinates of the considered node inside the extrapolation region and its corresponding node at the weld toe position, respectively; and δ is the distance between the weld toe and the considered node inside the extrapolation region.

Stress at an extrapolation point is obtained as follows:

$$\sigma_{\perp E} = \frac{\sigma_{\perp N1} - \sigma_{\perp N2}}{\delta_1 - \delta_2}\left(\Delta - \delta_2\right) + \sigma_{\perp N2} \tag{10}$$

where $\sigma_{\perp Ni}$ (i = 1 and 2) is the nodal stress in the immediate vicinity of the extrapolation point in a direction perpendicular to the weld toe (Eq. (7)); δ_i (i = 1 and 2) is obtained by Eq. (9); and Δ equals to 0.4*T* and 1.4*T* for the first and second extrapolation points, respectively (Fig. 9b).

The extrapolated stress at the weld toe position, HSS, is calculated by the following equation:

$$\sigma_{\perp W} = 1.4\sigma_{\perp E1} - 0.4\sigma_{\perp E2} \tag{11}$$

where $\sigma_{\perp E1}$ and $\sigma_{\perp E2}$ are the stresses at the first and second extrapolation points in the direction perpendicular to the weld toe, respectively (Eq. (10)).

If the considered nodes in the calculations of Eqs. (7)−(11) are located on the outer surface of the chord, the value of $\sigma_{\perp W}$ obtained from Eq. (11) is used as σ_O in Eq. (5); and if the considered nodes are located on the inner surface of the chord, the result of Eq. (11) is equivalent to σ_I which is required for the calculation of the DoB in Eq. (5).

To facilitate the calculation of DoB values, above formulation was implemented in a macro file developed by the ANSYS parametric design language (APDL). The input data required to be provided by the user of the macro file are the chord thickness, label number of the node located at the weld toe, and the label numbers of the nodes inside the extrapolation region. These nodes can be introduced using the graphic user interface (GUI).

3.1.5. Verification of the FE modeling

As far as the authors can tell, there is no experimental data available in the literature on the DoB values in tubular KT-joints. However, previous research works offer some experimental data, FE results, and parametric equations that can be used to validate the FE model developed in the present study.

3.1.5.a. Comparison with HSS experimental data

According to Eq. (5), DoB is a function of σ_O and σ_I that are the HSSs at the weld toe on the outer and inner surfaces of the chord, respectively. Hence, if the proposed FE model could predict the HSS accurately, then undoubtedly it can result in accurate DoB values.

To verify the developed FE modeling procedure, a validation FE model was generated, and its results were compared with the results of experimental tests carried out by the first author on a KT-joint (Figs. 10 and 11). Details of the test setup and program presented by Ahmadi [33] are not repeated here for the sake of brevity. Results of verification process are presented in Table 2. There is good agreement between the results of present FE model and experimental data; and the average difference is about 10%. Hence, the developed FE models can be considered accurate enough to provide valid results.

Table 1. Appropriate portion of an entire tubular KT-joint required to be modeled for each load case

Load case (Fig. 3)	Required portion to be modeled
1st OPB moment loading condition	¼ (Fig. 6b)
2nd OPB moment loading condition	¼ (Fig. 6b)
3rd OPB moment loading condition	½ (Fig. 6a)

Table 2. Results of FE model verification based on experimental data

Loading	Position	HSS value of the chord's outer surface (σ_O)		Difference
		Present FE model	Experimental test [33]	
Axial	Saddle	5.48e+6	5.89e+6	6.96%
	Crown	2.94e+6	3.38e+6	13.02%

Table 3. Geometrical properties of the tubular K-joint specimen used for the verification of FE models

Loading	Joint ID	D (mm)	τ	β	γ	α	θ	ζ
Axial	JISSP 3.3 [34]	508	1.0	0.5	20.3	12.6	45°	0.15
IPB	KJ-1 [7]	500	0.4	0.4	12.0	12.0	30°	0.15
OPB	KJ-1 [8]	500	0.4	0.4	12.0	12.0	30°	0.15

Table 4. Results of the FE model verification based on available parametric equations/FE results

Loading	Position	DoB values		Difference
		Present FE model	Available data	
Axial (Fig. 12a)	Saddle	0.6666	0.5529 (Morgan and Lee [3] Eq. (3d))	20.56%
	Toe	0.8727	0.8989 (Morgan and Lee [3] Eq. (3f))	2.91%
	Heel	0.7728	0.6997 (Morgan and Lee [3] Eq. (3b))	10.45%
IPB (Fig. 12b)	Toe	0.5991	0.5742 (Ahmadi et al. [7] FE model)	4.16%
OPB (Fig. 12c)	Saddle	0.8920	0.8045 (Ahmadi and Asoodeh [8] FE model)	10.87%

Table 5. Values assigned to each dimensionless parameter

Parameter	Definition	Value(s)
β	d/D	0.4, 0.5, 0.6
γ	$D/2T$	12, 18, 24
τ	t/T	0.4, 0.7, 1.0
θ		30°, 45°, 60°
ζ	g/D	0.3
α	$2L/D$	16
α_B	$2l/d$	8

Table 6. Statistical measures of the generated DoB samples at the saddle positions of central and outer braces under the OPB loadings (LC: loading condition)

Statistical measure	DoB samples					
	Sample 1	Sample 2	Sample 3	Sample 4	Sample 5	Sample 6
	Central brace, 1st OPB LC	Central brace, 2nd OPB LC	Central brace, 3rd OPB LC	Outer brace, 1st OPB LC	Outer brace, 2nd OPB LC	Outer brace, 3rd OPB LC
n	81	81	81	81	81	81
μ	0.7677	0.7554	0.8031	0.7300	0.7672	0.7112
σ	0.0406	0.0534	0.0406	0.0858	0.0684	0.0774
α_3	-0.2557	-0.5833	-0.3283	0.5302	-0.9654	-0.2877
α_4	2.4892	2.7189	2.2563	1.5652	4.0385	1.9325

3.1.5.b. Comparison with available DoB parametric equations and FE results

A set of FE parametric studies have been conducted by Morgan and Lee [3], Ahmadi et al. [7], and Ahmadi and Asoodeh [8] for the prediction of DoB values in tubular K-joints under the axial, IPB, and OPB loadings, respectively. Results of these studies were used in present research to validate the developed FE model. To so, three K-joint FE models were generated having typical geometrical characteristics (Table 3) and they were analyzed under the axial, IPB, and OPB loadings shown in Fig. 12. Geometrical properties of the axially-loaded FE model were selected based on the data provided by HSE OTH 354 [34] for a steel specimen tested to determine the SCFs; and geometrical properties of the IPB- and OPB-loaded FE models were selected in accordance with the validity range of the FE study conducted by Ahmadi et al. [7] and Ahmadi and Asoodeh [8].

The method of geometrical modeling (introducing the chord, braces, and weld profiles), the mesh generation procedure (including the selection of element type and size), analysis method, and the method of DoB extraction are identical for the validating models and the KT-joint models used for parametric study. Hence, the verification of DoB values derived from validating FE models with the results of equations proposed by Morgan and Lee [3], FE results of Ahmadi et al. [7], and FE results of Ahmadi and Asoodeh [8] lends support to the validity of DoB values derived from the KT-joint FE models.

Results of verification process are presented in Table 4. It can be seen that there is a good agreement among the results of present FE model and equations proposed by Morgan and Lee [3], FE results of Ahmadi et al. [7], and FE results of Ahmadi and Asoodeh [8]. The average difference is less than 10%. Hence, the generated FE models can be considered to be accurate enough to provide valid results.

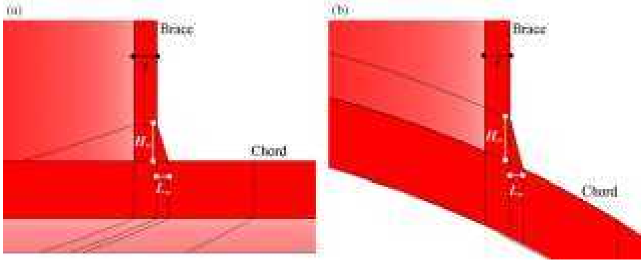

Fig. 4. Weld dimensions: (a) Crown position, (b) Saddle position

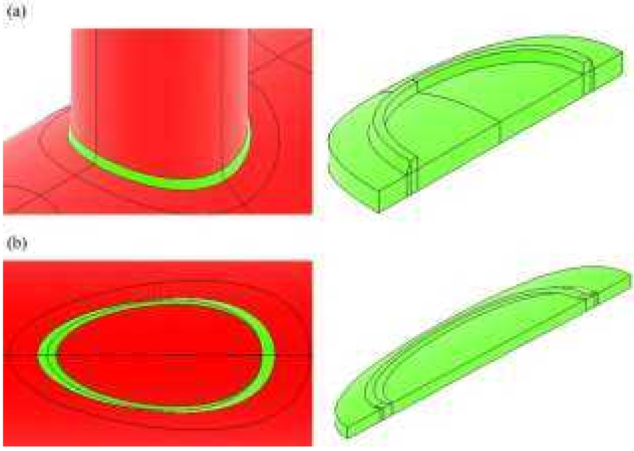

Fig. 5. Simulated weld profile: (a) Central brace, (b) Outer brace

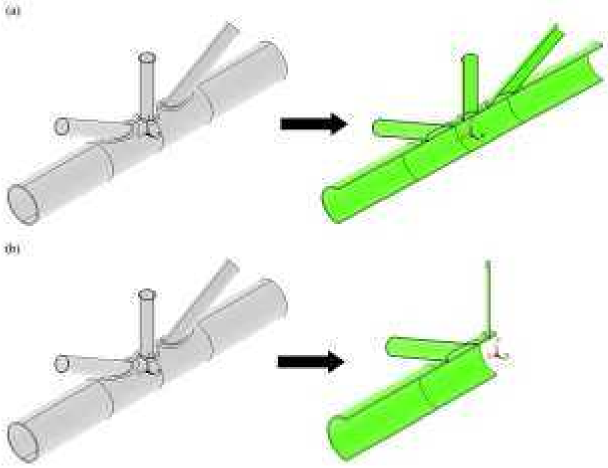

Fig. 6. Appropriate portion of the entire tubular KT-joint required to be modeled for each load case based on Table 1: (a) ½, (b) ¼

Fig. 7. Generated mesh for a tubular KT-joint using the sub-zone method

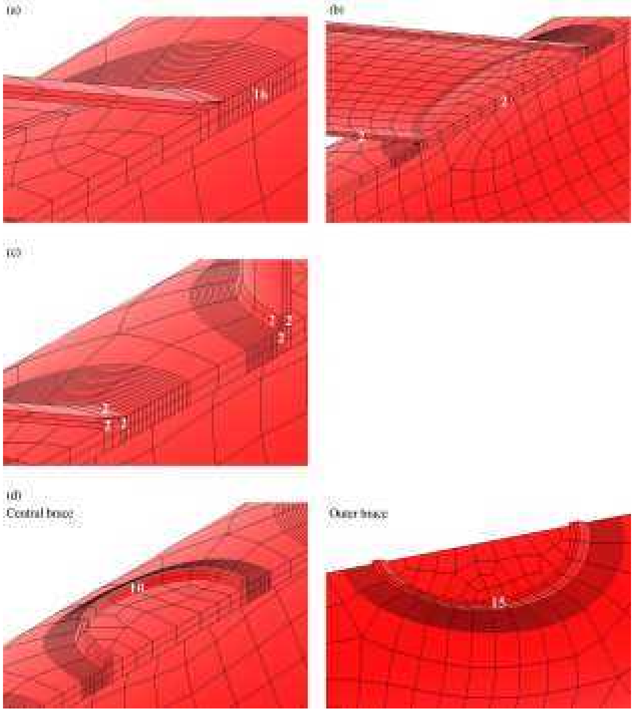

Fig. 8. The mesh density of: (a) Extrapolation region, (b) Chord and brace members, (c) Weld profile, (d) Brace-to-chord intersection

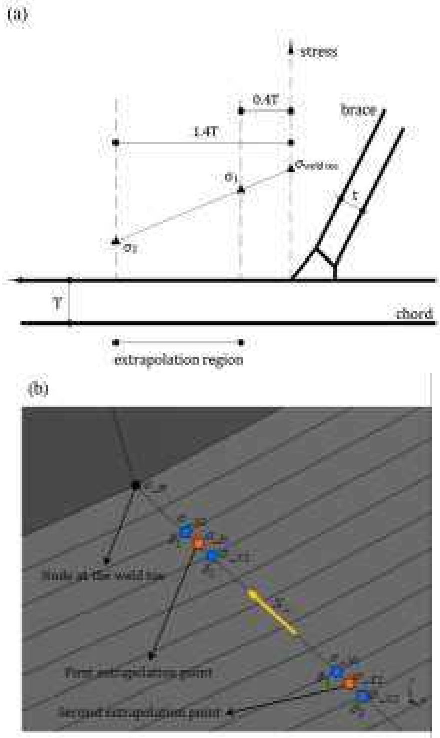

Fig. 9. (a) Extrapolation method recommended by IIW-XV-E [32], (b) Interpolations and extrapolations necessary to compute the DoB value based on the HSSs at the weld toe

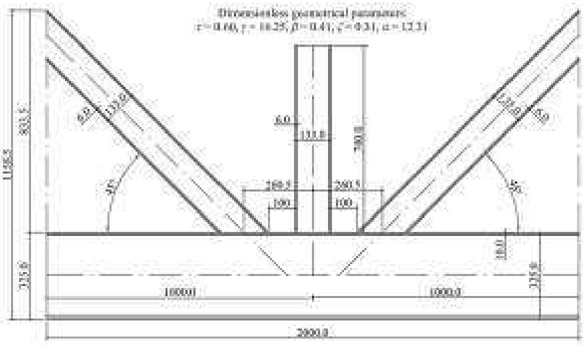

Fig. 10. Geometrical characteristics of tested tubular KT-joint specimen (unit: mm)

Fig. 11. Test setup: (a) View of the test rig and KT-joint specimen, (b) Strain gauges attached along the brace-to-chord intersection, (c) Connecting the strain gauges to the data logger

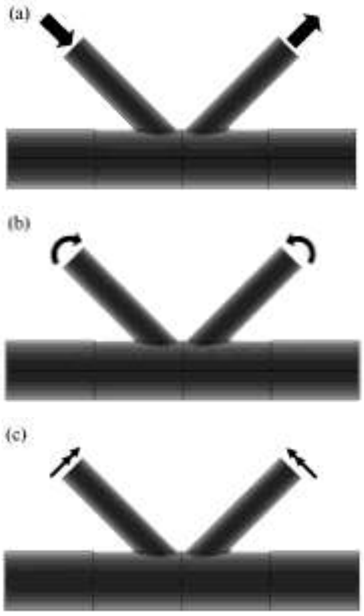

Fig. 12. Load cases for FE model validation: (a) Balanced axial loading studied by Morgan and Lee [3], (b) Balanced IPB loading studied by Ahmadi et al. [7], (c) Balanced OPB loading studied by Ahmadi and Asoodeh [8]

3.2. Details of parametric study

Altogether, 243 stress analyses were carried out on 81 FE models using ANSYS Ver. 11 to investigate the effects of dimensionless geometrical parameters on the DoB values at the saddle positions of the central and outer braces in tubular KT-joints subjected to three different types of OPB moment loading (Fig. 3).

Different values assigned to the parameters β, γ, τ, and θ have been presented in Table 5. These values cover the practical ranges of the dimensionless parameters typically found in tubular joints of offshore jacket structures. Providing that the gap between the braces is not very large, the relative gap ($\zeta = g / D$) has no considerable effect on stress and strain distribution. The validity range for this statement is $0.2 \leq \zeta \leq 0.6$ [19]. Hence, a typical value of $\zeta = 0.3$ was designated for all joints. Sufficiently long chord greater than six chord diameters (i.e. $\alpha \geq 12$) should be used to ensure that the stresses at the brace/chord intersection are not affected by the chord's boundary conditions [13]. The brace length has no effect on the HSSs when the parameter α_B is greater than critical value [16]. According to Chang and Dover [35], this critical value is about 6. In the present study, to avoid the effect of short brace length, a realistic value of $\alpha_B = 8$ was selected for all joints.

The 81 generated models span the following ranges of geometrical parameters:

$$\begin{array}{l} 0.4 \leq \beta \leq 0.6 \\ 12 \leq \gamma \leq 24 \\ 0.4 \leq \tau \leq 1.0 \\ 30^\circ \leq \theta \leq 60^\circ \end{array} \qquad (12)$$

3.3. Organization of the DoB samples

The DoB values extracted from the results of 243 FE analyses were organized as six samples for further statistical and probabilistic analyses. Samples 1−3 included the DoB values at the saddle position of the central brace under the 1st–3rd OPB loading conditions, respectively; while samples 4−6 included the DoB values at the saddle position of the outer brace under the 1st–3rd OPB loading conditions, respectively. Values of the size (n), mean (μ), standard deviation (σ), coefficient of skewness (α_3), and coefficient of kurtosis (α_4) for these samples are listed in Table 6.

The value of α_3 for the sample 4, that included the outer-brace DoB values under the 1st OPB load case, is positive which means that the probability distribution for this sample is expected to have a longer tail on the right, which is toward increasing values, than on the left. However, the value of α_3 for the other samples is negative meaning that the probability distribution for these samples is expected to have a longer tail on the left, which is toward decreasing values, than on the right.

The value of α_4 for the sample 5, that included the outer-brace DoB values under the 2nd OPB load case, is greater than three meaning that the probability distribution is expected to be sharp-peak (leptokurtic) for this sample; while the value of α_4 for the other DoB samples is smaller than three which means that for these samples, the probability distribution is expected to be mild-peak (platykurtic).

4. Application of the Freedman-Diaconis rule to generate the density histograms

To generate a density histogram, the range of data (R) is divided into several classes and the number of occurrences in each class is counted and tabulated. These are called frequencies. Then, the relative frequency of each class can be obtained through dividing its frequency by the sample size. Afterwards, the density is calculated for each class through dividing the relative frequency by the class width. The width of classes is usually made equal to facilitate interpretation.

Care should be exercised in the choice of the number of classes (n_c). Too few will cause an omission of some important features of the data; too many will not give a clear overall picture because there may be high fluctuations in the frequencies. One of the widely accepted rules to determine the number of classes is the Freedman-Diaconis rule expressed as follows [36]:

$$n_c = \frac{R\left(n^{1/3}\right)}{2\left(\mathrm{IQR}\right)} \tag{13}$$

where R is the range of sample data, n is the sample size, and IQR is the interquartile range calculated as:

$$\mathrm{IQR} = Q_3 - Q_1 \tag{14}$$

where Q_1 is the lower quartile which is the median of the lower half of the data; and likewise, Q_3 is the upper quartile that is the median of the upper half of the data.

Density histograms of generated samples are shown in Fig. 13. This figure shows that, as it was expected from the values of α_3 and α_4 in Table 6, the right tail is longer than the left one in the histogram of sample 4; while in the histograms of other samples, the left tail is longer. Moreover, the histogram of sample 5 is leptokurtic, while the histograms of other samples are platykurtic

5. PDF fitting based on the ML method

Thirteen different PDFs were fitted to the density histograms to assess the degree of fitting of various distributions to the DoB samples. In each case, distribution parameters were estimated using the maximum likelihood (ML) method. Results are given in Table 7. The ML procedure is an alternative to the method of moments. As a means of finding an estimator, statisticians often give it preference. For a random variable X with a known PDF, $f_X(x)$, and observed values $x_1, x_2, \ldots, x_n$, in a random sample of size n, the likelihood function of ω, where ω represents the vector of unknown parameters, is defined as:

$$L(\omega) = \prod_{i=1}^{n} f_X\left(x_i \mid \omega\right) \tag{15}$$

The objective is to maximize $L(\omega)$ for the given data set. It is done by taking m partial derivatives of $L(\omega)$, where m is the number of parameters, and equating them to zero. Then the maximum likelihood estimators (MLEs) of the parameter set ω can be found from the solutions of equations. In this way the greatest probability is given to the observed set of events, provided that the true form of the probability distribution is known.

6. Assessing the goodness-of-fit based on the Kolmogorov-Smirnov test

The Kolmogorov-Smirnov goodness-of-fit test is a nonparametric test that relates to the cumulative distribution function (CDF) of a continuous variable. The test statistic, in a two-sided test, is the maximum absolute difference (which is usually the vertical distance) between the empirical and hypothetical CDFs. For a continuous variate X, let $x_{(1)}, x_{(2)}, \ldots, x_{(n)}$ represent the order statistics of a sample of the size n, that is, the values arranged in increasing order. The empirical or sample distribution function $F_n(x)$ is a step function. This gives the proportion of values not exceeding x and is defined as:

$$\begin{aligned} F_n(x) &= 0, && \text{For } x < x_{(1)} \\ &= k/n, && \text{For } x_{(k)} \le x < x_{(k+1)} \\ & && \quad k = 1, 2, \ldots, n-1 \\ &= 1, && \text{For } x \ge x_{(n)} \end{aligned} \tag{16}$$

Empirical distribution functions for generated DoB samples have been shown in Fig. 14.

Let $F_0(x)$ denote a completely specified theoretical continuous CDF. The null hypothesis H_0 is that the true CDF of X is the same as $F_0(x)$. That is, under the null hypothesis:

$$\lim_{n\to\infty} \Pr\left[F_n(x) = F_0(x)\right] = 1 \tag{17}$$

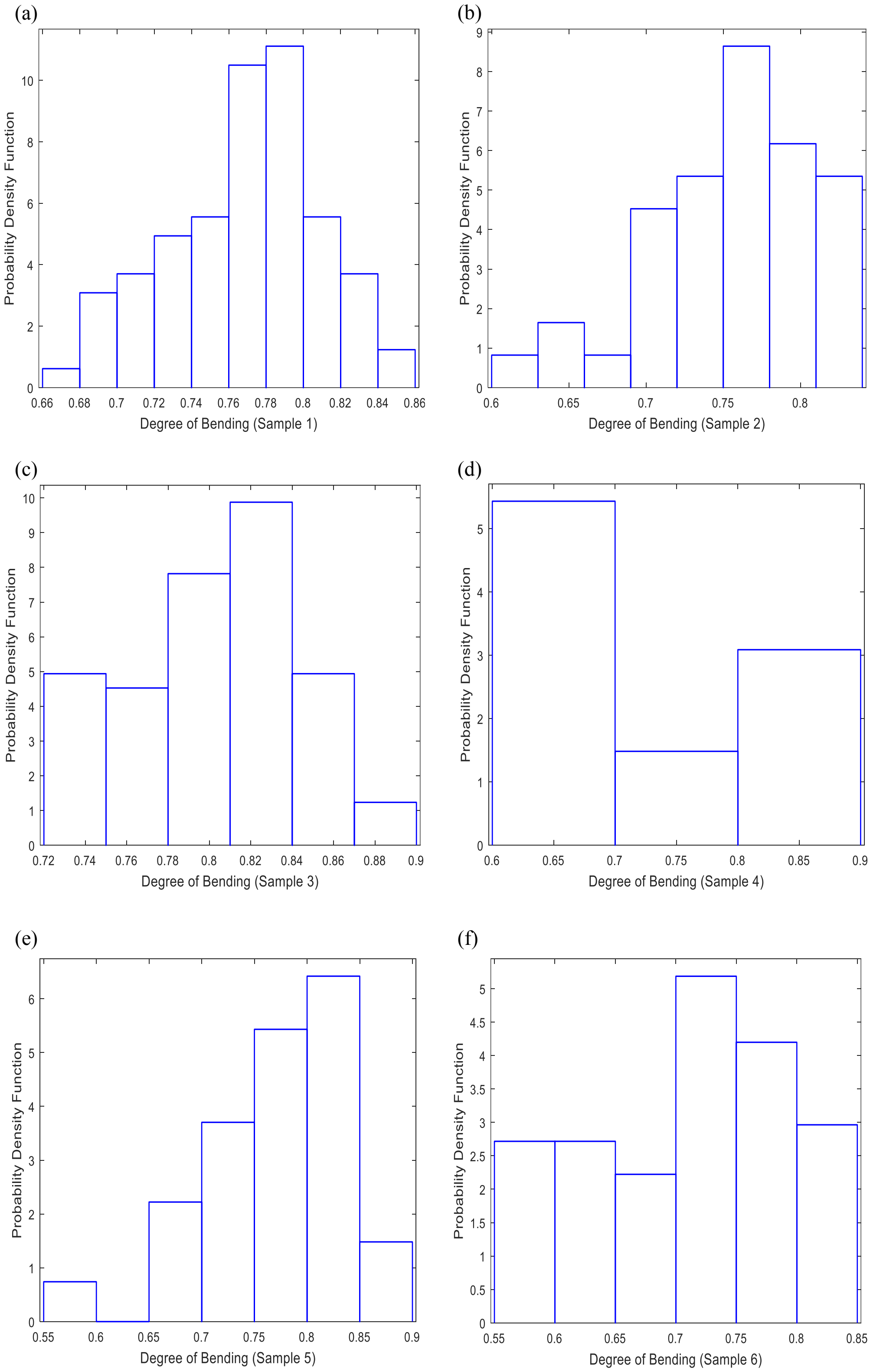

Fig. 13. Density histograms generated for the DoB samples: (a) Sample 1 (Saddle position of the central brace−1st OPB loading condition), (b) Sample 2 (Saddle position of the central brace−2nd OPB loading condition), (c) Sample 3 (Saddle position of the central brace−3rd OPB loading condition), (d) Sample 4 (Saddle position of the outer brace−1st OPB loading condition), (e) Sample 5 (Saddle position of the outer brace−2nd OPB loading condition), (f) Sample 6 (Saddle position of the outer brace−3rd OPB loading condition)

The test criterion is the maximum absolute difference between $F_n(x)$ and $F_0(x)$, formally defined as:

$$d_n = \sup_{x} \left| F_n(x) - F_0(x) \right| \tag{18}$$

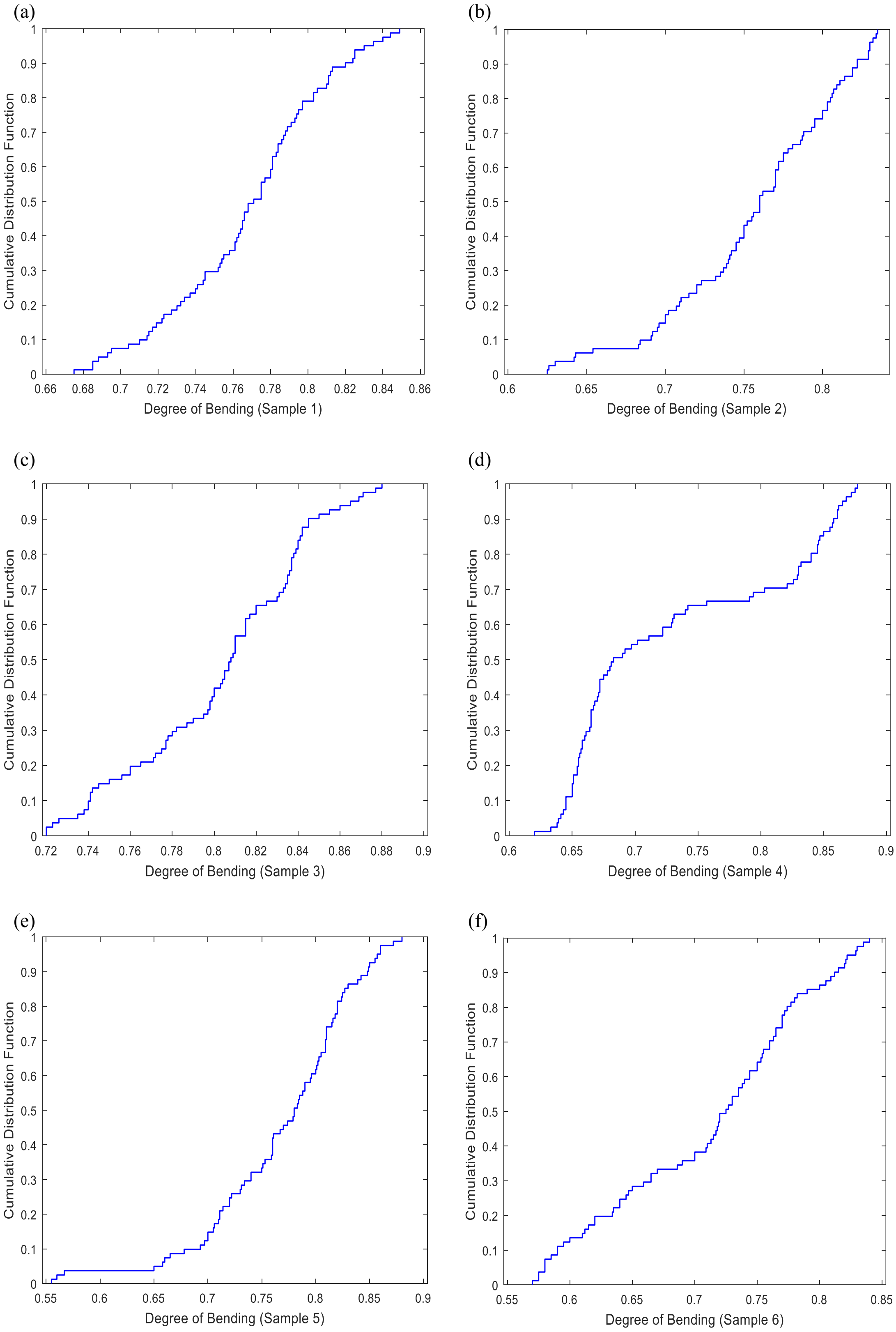

Fig. 14. Empirical cumulative distribution functions for generated DoB samples: (a) Sample 1 (Saddle position of the central brace−1st OPB loading condition), (b) Sample 2 (Saddle position of the central brace−2nd OPB loading condition), (c) Sample 3 (Saddle position of the central brace−3rd OPB loading condition), (d) Sample 4 (Saddle position of the outer brace−1st OPB loading condition), (e) Sample 5 (Saddle position of the outer brace−2nd OPB loading condition), (f) Sample 6 (Saddle position of the outer brace−3rd OPB loading condition)

Theoretical continuous CDFs fitted to the empirical distribution functions of generated DoB samples have been shown in Fig. 15.

A large value of this statistic (d_n) indicates poor fit. Hence, acceptable values should be known. The critical values $D_{n,\xi}$ for large samples, say $n > 35$, are ($1.3581/\sqrt{n}$) and ($1.6276/\sqrt{n}$) for $\xi = 0.05$ and 0.01, respectively [36] where ξ is the significance level.

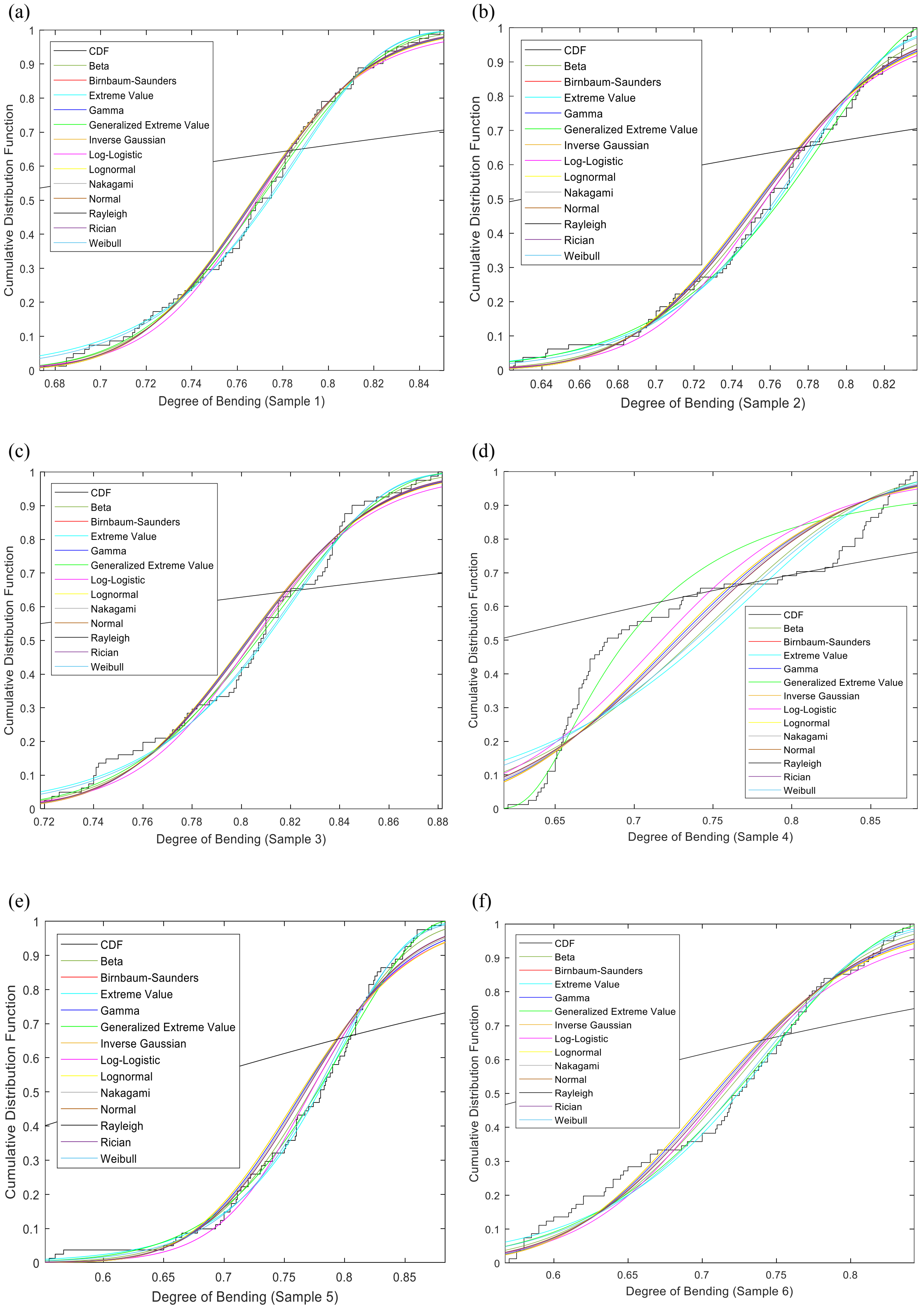

Fig. 15. Theoretical continuous CDFs fitted to the empirical CDFs of generated DoB samples: (a) Sample 1 (Saddle position of the central brace−1st OPB loading condition), (b) Sample 2 (Saddle position of the central brace−2nd OPB loading condition), (c) Sample 3 (Saddle position of the central brace−3rd OPB loading condition), (d) Sample 4 (Saddle position of the outer brace−1st OPB loading condition), (e) Sample 5 (Saddle position of the outer brace−2nd OPB loading condition), (f) Sample 6 (Saddle position of the outer brace−3rd OPB loading condition)

Results of the Kolmogorov-Smirnov test for the six prepared samples are given in Tables 8−13. It is evident in these tables that the Weibull distribution has the smallest d_n value for samples 2, 3, and 5; while the Beta distribution has the smallest d_n for samples 1 and 6; and the Generalized Extreme Value distribution has the smallest d_n value for sample 4. Hence, they are the best-fitted distributions for the corresponding DoB samples (Fig. 16).

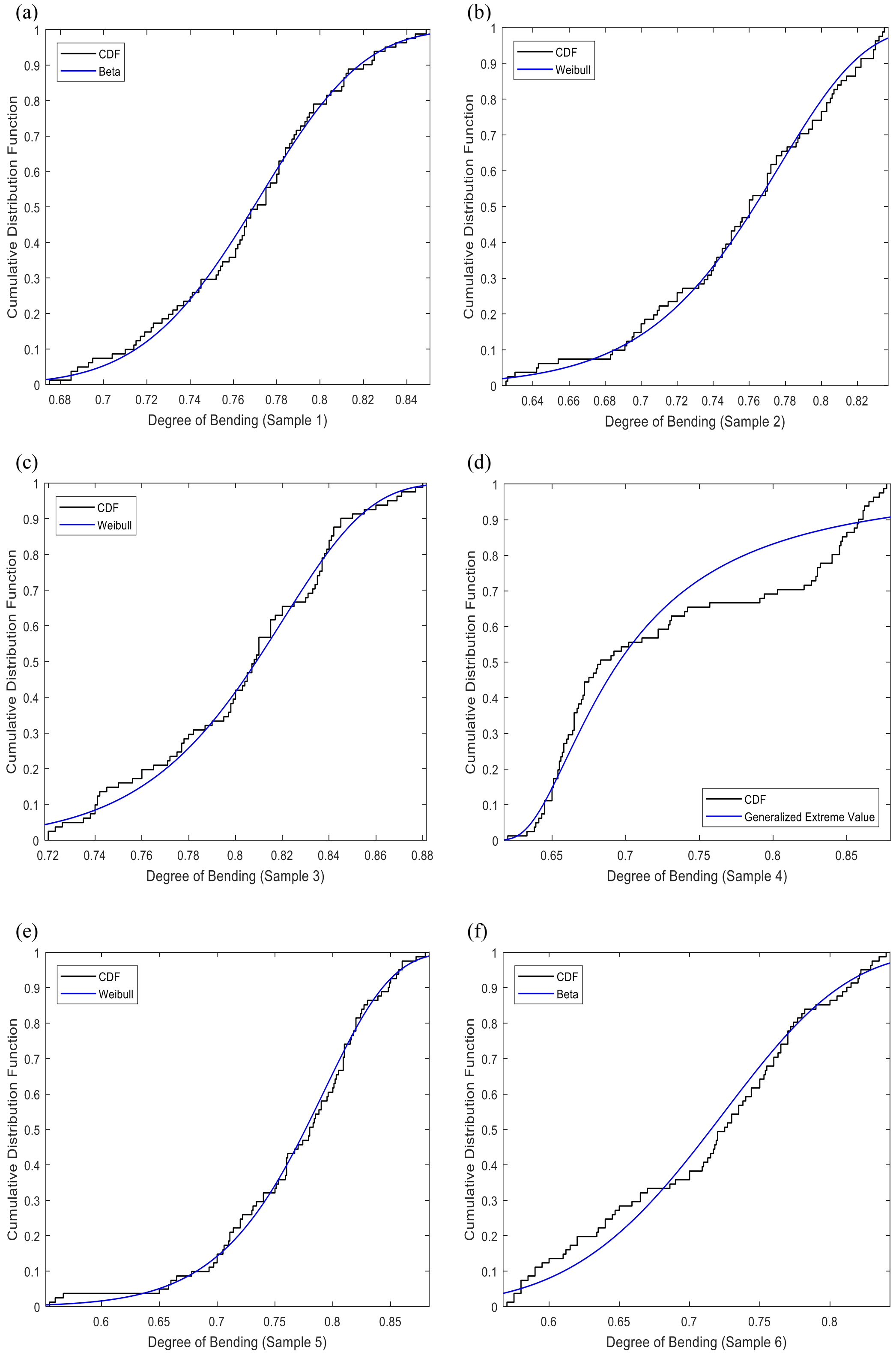

Fig. 16. The best-fitted distributions according to the Kolmogorov-Smirnov test: (a) Sample 1 (Saddle position of the central brace−1st OPB loading condition), (b) Sample 2 (Saddle position of the central brace−2nd OPB loading condition), (c) Sample 3 (Saddle position of the central brace−3rd OPB loading condition), (d) Sample 4 (Saddle position of the outer brace−1st OPB loading condition), (e) Sample 5 (Saddle position of the outer brace−2nd OPB loading condition), (f) Sample 6 (Saddle position of the outer brace−3rd OPB loading condition)

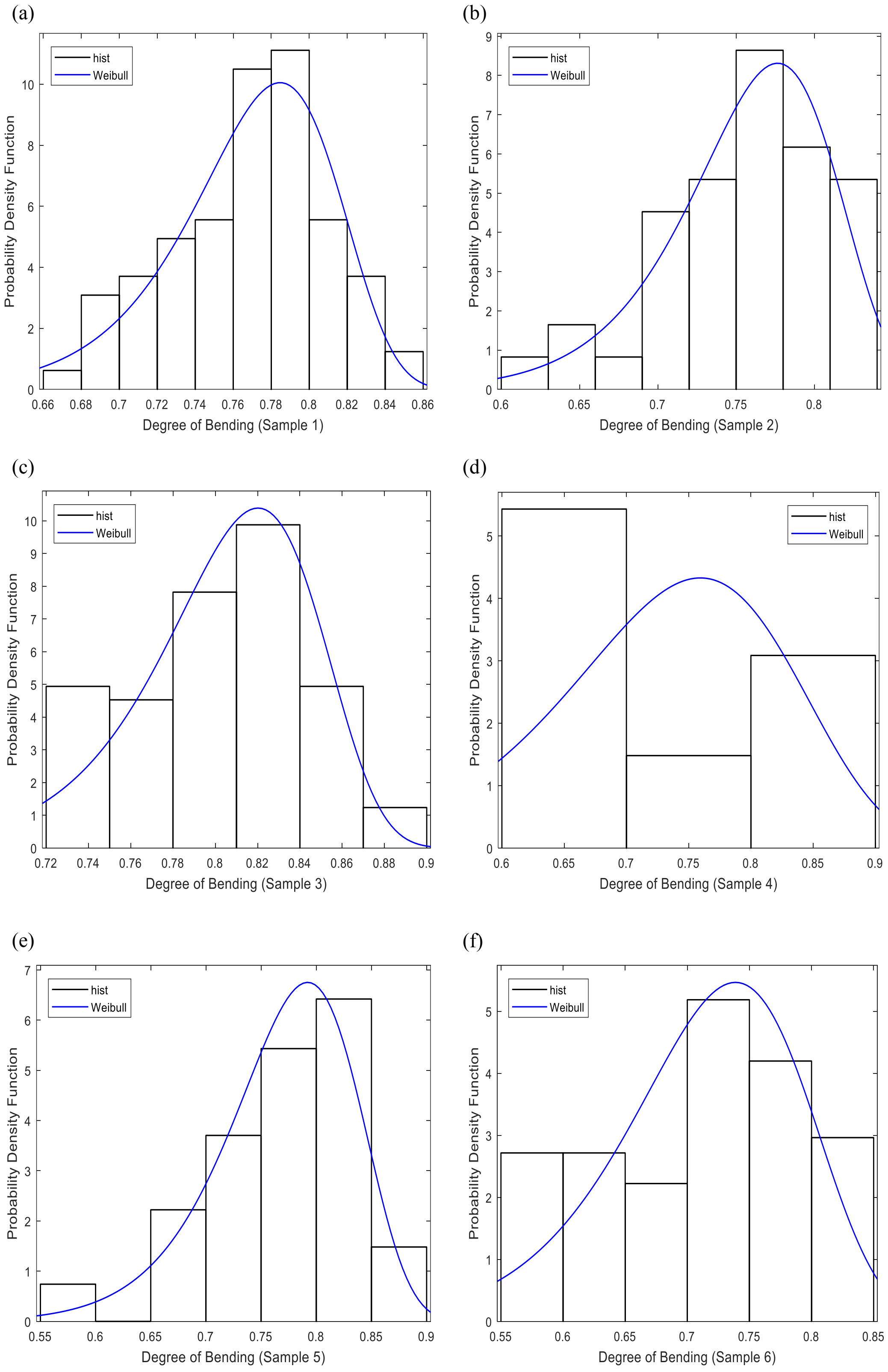

Fig. 17. Proposed PDFs for generated DoB samples: (a) Sample 1 (Saddle position of the central brace−1st OPB loading condition), (b) Sample 2 (Saddle position of the central brace−2nd OPB loading condition), (c) Sample 3 (Saddle position of the central brace−3rd OPB loading condition), (d) Sample 4 (Saddle position of the outer brace−1st OPB loading condition), (e) Sample 5 (Saddle position of the outer brace−2nd OPB loading condition), (f) Sample 6 (Saddle position of the outer brace−3rd OPB loading condition)

7. Proposed probability distribution model for the DoB

The best-fitted distributions for the generated DoB samples were introduced in Sect. 6. According to the results of the Kolmogorov-Smirnov test, the best-fitted distributions for the six samples studied include three different models: Weibull, Beta, and Generalized Extreme Value distributions. Results of the test for sample 1 are given in Table 8 as an example. The diversity of the best-fitted probability models derived for the studied DoB values may practically result in the confusion and difficulty of their application for the fatigue reliability analysis and design. Hence, reducing the number of distribution types proposed for the DoB values might be a good idea. To do so, the top three distribution functions for each DoB sample were identified (Table 9). The aim was to propose a single probability model to cover all the DoB samples.

Table 7. Estimated parameters for PDFs fitted to the density histograms of DoB samples at the saddle positions of central and outer braces under the OPB loadings

Fitted PDF	Parameters	Estimated values					
		Sample 1	Sample 2	Sample 3	Sample 4	Sample 5	Sample 6
		Central brace, 1st OPB LC	Central brace, 2nd OPB LC	Central brace, 3rd OPB LC	Outer brace, 1st OPB LC	Outer brace, 2nd OPB LC	Outer brace, 3rd OPB LC
Beta	a	83.8823	50.743	78.3375	17.5857	31.1492	24.5695
	b	25.3897	16.4367	19.2069	6.47731	9.46798	9.97889
Birnbaum-Saunders	β_0	0.766573	0.753467	0.802076	0.725243	0.763867	0.706875
	γ_0	0.0531083	0.0722212	0.0508064	0.114098	0.0940614	0.111056
Extreme Value	μ	0.787314	0.780396	0.822556	0.774508	0.798101	0.748376
	σ	0.0364656	0.0433962	0.0351623	0.0841897	0.0530766	0.0656653
Gamma	a	357.355	195.681	390.627	75.8396	118.292	82.8304
	b	0.00214815	0.00386053	0.00205595	0.00962509	0.00648605	0.00858664
Generalized Extreme Value	k	-0.391922	-0.646434	-0.435386	0.481081	-0.559969	-0.531689
	σ	0.042301	0.0598337	0.0428433	0.0472531	0.0737407	0.0840801
	μ	0.755539	0.746487	0.791866	0.676441	0.752732	0.693635
Inverse Gaussian	μ	0.767654	0.755432	0.803111	0.729963	0.767247	0.711235
	λ	271.979	144.644	310.928	55.8902	86.5272	57.4896
Log-logistic	μ	-0.263184	-0.277077	-0.217255	-0.332146	-0.259053	-0.338664
	σ	0.0305197	0.0408412	0.0295985	0.069967	0.0499815	0.0659058
Lognormal	μ	-0.265816	-0.283023	-0.220543	-0.321369	-0.269179	-0.346802
	σ	0.0534228	0.0726227	0.05111	0.114712	0.0944668	0.111631
Nakagami	μ	90.0914	49.9548	98.5318	18.8403	30.8618	21.232
	ω	0.590922	0.573497	0.646616	0.54012	0.593291	0.511776
Normal	μ	0.767654	0.755432	0.803111	0.729963	0.767247	0.711235
	σ	0.0406125	0.0534259	0.0406088	0.0858191	0.0684187	0.0774278
Rayleigh	b	0.543563	0.535489	0.568602	0.519673	0.544652	0.505854
Rician	s	0.76659	0.753555	0.802094	0.724892	0.764204	0.707009
	σ	0.0403892	0.0531614	0.040383	0.0855907	0.0681317	0.0771814
Weibull	a	0.786417	0.779049	0.821756	0.76943	0.796071	0.745173
	b	21.4633	17.5732	23.183	8.99524	14.5745	11.0243

Table 8. Results of the Kolmogorov-Smirnov goodness-of-fit test for DoB sample 1 (Central brace−1st OPB LC)

Fitted distribution	Test statistic (d_n)	Critical value ($D_{n,\xi}$)		Test result	
		$\xi = 0.05$	$\xi = 0.01$	$\xi = 0.05$	$\xi = 0.01$
Beta	0.037064	0.1509	0.180844444	Accept	Accept
Birnbaum-Saunders	0.062642			Accept	Accept
Extreme Value	0.067938			Accept	Accept
Gamma	0.058971			Accept	Accept
Generalized Extreme Value	0.042086			Accept	Accept
Inverse Gaussian	0.062647			Accept	Accept
Log-logistic	0.054059			Accept	Accept
Lognormal	0.062892			Accept	Accept
Nakagami	0.05544			Accept	Accept
Normal	0.052209			Accept	Accept
Rayleigh	0.537469			Reject	Reject
Rician	0.051817			Accept	Accept
Weibull	0.058837			Accept	Accept

Table 9. Best-fitted distributions for the DoB samples at the saddle positions of the central and outer braces based on the results of the Kolmogorov-Smirnov test

Best-fitted distributions	DoB samples					
	Sample 1 Central brace, 1st OPB LC	Sample 2 Central brace, 2nd OPB LC	Sample 3 Central brace, 3rd OPB LC	Sample 4 Outer brace, 1st OPB LC	Sample 5 Outer brace, 2nd OPB LC	Sample 6 Outer brace, 3rd OPB LC
#1	Beta	Weibull	Weibull	Generalized Extreme Value	Weibull	Beta
#2	Generalized Extreme Value	Beta	Generalized Extreme Value	-	Extreme Value	Generalized Extreme Value
#3	Rician	Extreme Value	Extreme Value	-	Generalized Extreme Value	Extreme Value

Table 10. Comparison of the test statistics for the proposed and the best-fitted distributions based on the results of the Kolmogorov-Smirnov test

	Test statistic					
	Sample 1 Central brace, 1st OPB LC	Sample 2 Central brace, 2nd OPB LC	Sample 3 Central brace, 3rd OPB LC	Sample 4 Outer brace, 1st OPB LC	Sample 5 Outer brace, 2nd OPB LC	Sample 6 Outer brace, 3rd OPB LC
Best-fitted distribution	0.037064 (Beta)	0.044443 (Weibull)	0.056591 (Weibull)	0.142567 (Generalized Extreme Value)	0.045182 (Weibull)	0.076427 (Beta)
Proposed distribution	0.058837 (Weibull)	0.044443 (Weibull)	0.056591 (Weibull)	- (Weibull)	0.045182 (Weibull)	0.0851 (Weibull)
Difference	58.74%	0%	0%	-	0%	11.35%

After surveying the data presented in Table 9, the Weibull model is proposed as the governing probability distribution function for DoB values. The difference between the test statistics of the proposed distribution and the best-fitted one for each sample is presented in Table 10. Using the information presented in these tables, the analyst can make a choice, based on the engineering judgment, between the best-fitted and the proposed probability models for each of the studied cases.

The PDF of Weibull distribution is expressed as:

$$f_X(x|a,b) = \frac{b}{a}\left(\frac{x}{a}\right)^{b-1} e^{-(x/a)^b} \tag{19}$$

After substituting the values of estimated parameters from Table 7, following probability density functions are proposed for the DoB values in tubular KT-joints subjected to the three considered OPB load cases defined in Fig. 3:

Saddle position of the central brace−1st load case:

$$f_X(x) = 27.292\left(\frac{x}{0.7864}\right)^{20.463} e^{-(x/0.7864)^{21.463}} \tag{20}$$

Saddle position of the central brace−2nd load case:

$$f_X(x) = 22.557\left(\frac{x}{0.7791}\right)^{16.573} e^{-(x/0.7791)^{17.573}} \tag{21}$$

Saddle position of the central brace−3rd load case:

$$f_X(x) = 28.211\left(\frac{x}{0.8218}\right)^{22.183} e^{-(x/0.8218)^{23.183}} \tag{22}$$

Saddle position of the outer brace−1st load case:

$$f_X(x) = 11.691\left(\frac{x}{0.7694}\right)^{7.9952} e^{-(x/0.7694)^{8.9952}} \tag{23}$$

Saddle position of the outer brace−2nd load case:

$$f_X(x) = 18.308\left(\frac{x}{0.7961}\right)^{13.574} e^{-(x/0.7961)^{14.575}} \tag{24}$$

Saddle position of the outer brace−3rd load case:

$$f_X(x) = 14.794\left(\frac{x}{0.7452}\right)^{10.024} e^{-(x/0.7452)^{11.024}} \tag{25}$$

where X denotes the DoB as a random variable and x represents its values.

Developed PDFs, shown in Fig. 17, can be adapted in the fatigue reliability analysis and design of OPB-loaded tubular KT-joints commonly found in offshore jacket structures.

8. Conclusions

A total of 243 FE analyses were carried out in the present research on 81 models of KT-joints subjected to three types of OPB moment loading. Generated FE models were validated using experimental data, previous FE results, and available parametric equations. FE analysis results were used to develop a set of PDFs for the DoB in OPB-loaded KT-joints. Based on the results of parametric FE study, a sample database was prepared for the DoB values and density histograms were generated for respective samples based on the Freedman-Diaconis rule. Thirteen theoretical PDFs were fitted to the developed histograms, and the ML method was applied to evaluate the parameters of fitted PDFs. In each case, the Kolmogorov-Smirnov test was used to evaluate the goodness of fit. Finally, the Weibull model was proposed as the governing probability distribution function for the DoB. After substituting the values of estimated parameters, six fully defined PDFs were presented for the DoB at the saddle positions of the central and outer braces in tubular KT-joints subjected to three types of OPB moment loading.

References

[1] Connolly MPM. A fracture mechanics approach to the fatigue assessment of tubular welded Y and K-joints. PhD Thesis, University College London, UK; 1986.

[2] Chang E, Dover WD. Prediction of degree of bending in tubular X and DT joints. International Journal of Fatigue 1999;21(2):147–61.

[3] Morgan MR, Lee MMK. Prediction of stress concentrations and degrees of bending in axially loaded tubular K-joints. Journal of Constructional Steel Research 1998;45(1):67–97.

[4] UK Department of Energy (DoE). Background to new fatigue design guidance for steel joints and connections in offshore structures. London, UK; 1995.

[5] Lee MMK, Bowness D. Estimation of stress intensity factor solutions for weld toe cracks in offshore tubular joints. International Journal of Fatigue 2002;24:861–75.

[6] Shen W, Choo YS. Stress intensity factor for a tubular T-joint with grouted chord. Engineering Structures 2012;35:37–47.

[7] Ahmadi H, Lotfollahi-Yaghin MA, Asoodeh Sh. Degree of bending (DoB) in tubular K-joints of offshore structures subjected to in-plane bending (IPB) loads: Study of geometrical effects and parametric formulation. Ocean Engineering 2015;102:105–16.

[8] Ahmadi H, Asoodeh Sh. Parametric study of geometrical effects on the degree of bending (DoB) in offshore tubular K-joints under out-of-plane bending loads. Applied Ocean Research 2016;58:1–10.

[9] Ahmadi H, Asoodeh Sh. Degree of bending (DoB) in tubular KT-joints of jacket structures subjected to axial loads. International Journal of Maritime Technology 2015;4(2):65–75.

[10] Ahmadi H, Amini Niaki M. Effects of geometrical parameters on the degree of bending (DoB) in two-planar tubular DT-joints of offshore jacket structures subjected to axial and bending loads. Marine Structures 2019;64(C):229−245.

[11] Ahmadi H, Ghaffari AR. Probabilistic assessment of degree of bending (DoB) in tubular X-joints of offshore structures subjected to bending loads. Advances in Civil Engineering 2015;1–12.

[12] Ahmadi H, Ghaffari AR. Probabilistic analysis of stress intensity factor (SIF) and degree of bending (DoB) in axially loaded tubular K-joints of offshore structures. Latin American Journal of Solids and Structures 2015;12(11):2025–2044.

[13] Efthymiou M. Development of SCF formulae and generalized influence functions for use in fatigue analysis. OTJ 88, Surrey, UK; 1988.

[14] Hellier AK, Connolly M, Dover WD. Stress concentration factors for tubular Y and T-joints. International Journal of Fatigue 1990;12:13–23.

[15] Morgan MR, Lee MMK. Parametric equations for distributions of stress concentration factors in tubular K-joints under out-of-plane moment loading. International Journal of Fatigue 1998;20:449–61.

[16] Chang E, Dover WD. Parametric equations to predict stress distributions along the intersection of tubular X and DT-joints. International Journal of Fatigue 1999;21:619–35.

[17] Shao YB. Geometrical effect on the stress distribution along weld toe for tubular T- and K-joints under axial loading. Journal of Constructional Steel Research 2007;63:1351–60.

[18] Shao YB, Du ZF, Lie ST. Prediction of hot spot stress distribution for tubular K-joints under basic loadings. Journal of Constructional Steel Research 2009;65:2011–26.

[19] Lotfollahi-Yaghin MA, Ahmadi H. Effect of geometrical parameters on SCF distribution along the weld toe of tubular KT-joints under balanced axial loads. International Journal of Fatigue 2010;32:703–19.

[20] Ahmadi H, Lotfollahi-Yaghin MA, Aminfar MH. Geometrical effect on SCF distribution in uni-planar tubular DKT-joints under axial loads. Journal of Constructional Steel Research 2011;67:1282–91.

[21] Lotfollahi-Yaghin MA, Ahmadi H. Geometric stress distribution along the weld toe of the outer brace in two-planar tubular DKT-joints: parametric study and deriving the SCF design equations. Marine Structures 2011;24:239–60.

[22] Ahmadi H, Lotfollahi-Yaghin MA. Geometrically parametric study of central brace SCFs in offshore three-planar tubular KT-joints. Journal of Constructional Steel Research 2012;71:149–61.

[23] Ahmadi H, Lotfollahi-Yaghin MA, Shao YB. Chord-side SCF distribution of central brace in internally ring-stiffened tubular KT-joints: A geometrically parametric study. Thin-Walled Structures 2013;70:93−105.

[24] Ahmadi H, Zavvar E. The effect of multi-planarity on the SCFs in offshore tubular KT-joints subjected to in-plane and out-of-plane bending loads. Thin-Walled Structures 2016;106:148−165.

[25] Shao YB, Lie ST. Parametric equation of stress intensity factor for tubular K-joint under balanced axial loads. International Journal of Fatigue 2005;27:666–79.

[26] Shao YB. Analysis of stress intensity factor (SIF) for cracked tubular K-joints subjected to balanced axial load. Engineering Failure Analysis 2006;13:44–64.

[27] American Welding Society (AWS). Structural welding code: AWS D 1.1. Miami (FL), US; 2002.

[28] Lie ST, Lee CK, Wong SM. Modeling and mesh generation of weld profile in tubular Y-joint. Journal of Constructional Steel Research 2001;57:547–67.

[29] Ahmadi H, Lotfollahi-Yaghin MA, Shao YB, Aminfar MH. Parametric study and formulation of outer-brace geometric stress concentration factors in internally ring-stiffened tubular KT-joints of offshore structures. Applied Ocean Research 2012;38:74–91.

[30] Wordsworth AC, Smedley GP. Stress concentrations at unstiffened tubular joints. Proceedings of the European Offshore Steels Research Seminar, Paper 31, Cambridge, UK; 1978.

[31] Smedley P, Fisher P. Stress concentration factors for simple tubular joints. Proceedings of the International Offshore and Polar Engineering Conference (ISOPE), Edinburgh; 1991. p. 475–83.

[32] IIW-XV-E. Recommended fatigue design procedure for welded hollow section joints, IIW Docs, XV-1035-99/XIII-1804-99. International Institute of Welding, France; 1999.

[33] Ahmadi H. Experimental and numerical investigation of the SCF distribution in unstiffened and stiffened uniplanar tubular KT-joints of steel platforms and the extension of numerical study to multi-planar joints. PhD Thesis, Faculty of Civil Engineering, University of Tabriz, Tabriz, Iran; 2012 (In Farsi).

[34] UK Health and Safety Executive. OTH 354: Stress concentration factors for simple tubular joints-assessment of existing and development of new parametric formulae. Prepared by Lloyd’s Register of Shipping, UK, 1997.

[35] Chang E, Dover WD. Stress concentration factor parametric equations for tubular X and DT joints. International Journal of Fatigue 1996;18(6):363–87.

[36] Kottegoda NT, Rosso R. Applied statistics for civil and environmental engineers. 2nd Edition, Blackwell Publishing Ltd, UK; 2008.

INTERNATIONAL JOURNAL OF
COASTAL, OFFSHORE & ENVIRONMENTAL ENGINEERING IJCOE Vol.10/No. 2/ Spring 2025 (35-44)

Available online at: www. Ijcoe.org

Comparative Analysis of Distorted Froudian and Equivalent Single Degree of Freedom Models in Offshore Jacket Platform Seismic Simulation

Mohamadhosein Mohasel[1*], **Ahmad Reza Mostafa Gharabaghi**[2], **Mohamad Reza Chenaghlou**[3]

[1*] *Ph.D. Candidate, Department of Coasts, Ports and Marine Structures, Sahand University of Technology, Tabriz, Iran; m_mohasel@sut.ac.ir*
[2] *Professor, Department of Coasts, Ports and Marine Structures, Sahand University of Technology, Tabriz, Iran*
[3] *Professor, Faculty of Civil Engineering, Sahand University of Technology, Tabriz, Iran*

ARTICLE INFO

Article History
Received: 24 July 2024
Accepted: 21 July 2025

Keywords:
Offshore Jacket Platform
Physical Modeling
Distorted Froudian Model
Equivalent Single Degree of Freedom
Time History Response

ABSTRACT

The techniques of modeling are a very powerful way to simulate offshore platforms. For situations where the numerical modelling of structure process is very complex, these methods are preferred, and the model cannot be expressed in precise mathematical formulas. Dynamic characteristics of the structure shall be taken into account in order to determine simulation specifications. In this article, two methods of distorted Froudian models and an equivalent single degree of freedom system were used to model the platform. In the distorted Froudian method, by allocating different scale coefficients for geometric features and other specifications, the problem of modeling members that suffer from problems such as unreality due to applying some scale coefficients (such as the thickness of tubular members) is solved. In the second method, due to the more significant effect of the first mode on the vibration of the system (more than 90% mass participation), the structure becomes an equivalent single degree of freedom model and the construction of the platform in the laboratory becomes very simple. The obtained results showed the excellent accuracy of both methods and the excellent efficiency of the equivalent system with an equivalent single degree of freedom in the specific conditions in this research.

1. Introduction

For oil and gas exploitation, steel jacket platforms are frequently used. At a depth of 100 to 150 meters, these platforms are typically used. The steel jacket platforms have a low vibration frequency of 0.125 to 0.5 Hz [1]. If the frequency of the jacket platform is in the range of earthquake loading frequency, it may induce resonance and increase the dynamic responses of the structure. Due to the difficulty of obtaining data from prototypes, it is important to develop and test offshore platform models. Therefore, it is necessary to ensure that the model accurately replicates the behavior of the original sample. It is not easy to draw accurate analytical expressions for the modelling of structure behavior, as offshore platforms dynamics and description of their mechanical properties are complex. However, this behavior can be modeled using similarity techniques. Similarity analysis is a partial analysis that leads to the extraction of dimensionless equations or π expressions. The advantage of this method is that it simplifies the problem and provides the scale of the model. Each dimensionless parameter of a functional equation or π term shall have the same numeric value for both models and prototypes when modelling with simulation methods [2]. Using simulation theory, it is necessary to fulfill geometric, kinematic and dynamic simulations. Experimental modeling has an important effect in evaluating the dynamic behavior of offshore platforms. In fact, it is fundamental for the validation and calibration of numerical models and the evaluation of design procedures. In the offshore industry, Froudian scaling lows are adopted because this method usually keeps the ratio between the hydrodynamic and gravitational forces on the prototype and the model constant [3]. However, this traditional scaling approach does not take into account several phenomena that arise in many practical cases. The seismic behavior of offshore jacket platforms has been discussed by many researchers using different methods [4–8]. Trung [9] present a new Ensemble Empirical Mode Decomposition-Hilbert transform (EEMD-HT)-based analysis structures under an artificial and natural excitation. Walia et al. [10] address the setup of the scaled model testing as carried out at the offshore basin of the Ecole Centrale de Nantes, as well as the numerical model for the GICON®-TLP[1], and shows good agreements for the tank tests and the numerical models. In Erfani's research [11], results of buckling analysis of 384 finite element models, verified using three different test results obtained from three separate experimental investigations, were used to study the effects of five parameters such as D/t, L/D, imperfection, mesh size and mesh size ratio. Ou et al. [12] showed that for an offshore platform, if the mass contribution coefficient of the first mode is more than 90%, the structure can be considered as an Equivalent Single Degree of Freedom (ESDOF) system. In another study, Hosseinlou et al. [13] presented static and dynamic compression methods to determine the dynamic characteristics of the offshore jacket platform in terms of uncertainty. Also, Leng et al. [14] achieved favorable results of the dynamic control of the structure by physically modeling a jacket platform with three degree of freedom and another jacket platform with five degree of freedom as an equivalent single degree of freedom structure.

The purpose of this article is to present two modeling methods for offshore platforms. These two methods are: (i) Distorted Froudian (DF) [15] and (ii) ESDOF model [16]. The scales of thickness, length and modulus of elasticity are limited due to the Froudian conditions. This is leading to modelling problems, and certain scales have to be distorted. The length scale may not be as similar to the modulus of elasticity scale, e.g. In the past, all models have been built on the basis of equal internal and external forces inside or outside the members. Therefore, under those conditions the distorted Froudian models developed in this area are also defined. In the undistorted Froudian model, which is not applicable for modeling offshore platforms, each scale is fixed according to the ratio of modulus of elasticity or the equivalent length scale (because the length scale is fixed based on the ratio of modulus of elasticity). In the second method, an MDOF[2] system is modeled as an ESDOF structure based on the first mode. It is necessary to explain, since in offshore platforms the first mode is the dominant mode and the participation coefficient of the first mode is greater than 90% [17], the assumption of the SDOF system of the simplified jacket platform is confirmed. In the following, a jacketed offshore platform is modeled using these two methods and the advantages and disadvantages of each method is discussed.

2. Methodology

Laboratory modeling of an offshore platform is of great importance for predicting the behavior of the structure due to the high cost of marine projects. This modeling, when the loading is dynamic (such as an earthquake), the complexity of predicting the behavior of the structure multiplies. But due to the many limitations that exist for modeling (such as model dimensions, behavior of materials, behavior of external loads, etc.), it is necessary for this modeling to be accurate. In this section, the rules governing the similarity between the model and the prototype are explained. The distorted Froudian model is defined as a model that satisfies the conditions of equal internal and external forces and equality of the Distorted Froudian number. Generally, in this model, the speed scale defined by the Froudian condition λ_{vw} is considered equal to the structure speed scale λ_v. The equality of the Distorted Froudian number in the main structure and the model requires that [18]:

$$\left(\frac{v}{\sqrt{gl}}\right)_m = \left(\frac{v}{\sqrt{gl}}\right)_p \tag{1}$$

Where the index m is defined for the model and p for the main structure. Also, l represents the length (or dimension), v is the velocity of the structure, and g is the acceleration of the earth's gravity. If the length scale of a structural member is as $\lambda_l = l_m/l_p$, the modulus of elasticity (E) is as $\lambda_E = E_m/E_p$, the thickness scale of members (t) is as $\lambda_t = t_m/t_p$ and the density scale of members (ρ) is as $\lambda_\rho = \rho_m/\rho_p$ are defined, it can be written:

$$\lambda_v = \sqrt{\lambda_l} \tag{2}$$

Since $\lambda_v = \lambda_\rho^{-0.5} \lambda_E^{0.5}$, therefore by placing it in Eq. (2) it can be shown that:

$$\lambda_l = \lambda_\rho^{-1} \lambda_E \tag{3}$$

For tubular members with diameter D and thickness t, considering the moment of inertia of the section ratio and Eq. (3), the following thickness scale factor is obtained:

$$\lambda_t = \lambda_l^2 \lambda_E^{-1} = \lambda_l \lambda_\rho^{-1} \tag{4}$$

If the model is without distortion ($\lambda_\rho = 1$), from Eqs. (3) and (4) we can write: $\lambda_E = \lambda_l$ and $\lambda_t = \lambda_l$. This case is defined as a Froudian model without distortion. Therefore, for a Froudian model without distortion, the relationships are presented as follows [15]:

$$\lambda_\rho = 1, \lambda_l = \lambda_E, \lambda_t = \lambda_l \tag{5}$$

In the case of the distorted Froudian model, Eq. (5) is not met, while Eq. (4) is met. In this case, the length scale may not be the same as the modulus of elasticity or the thickness scale. But this scale coefficient is associated with Eq. (4). Therefore, the length and

---

[1] Tension Leg Platform

[2] Multi Degree of Freedom

thickness of scales may differ according to the modulus of elasticity.

According to Eq. (4), the density and thickness scale coefficients are limited by the scale coefficient of the modulus of elasticity in the distorted Froudian model. Usually the designer decides on a length scale in that case. However, it is theoretically possible to select a scale factor for thickness and modulus of elasticity from Eq. (4), then calculate the length scale factor accordingly. Alternatively, Eq. 4 shows a density scale coefficient when the thickness and length coefficients have been selected. As a result, mass must be corrected in order to satisfy the Eqs. of (3) and (4). For the distorted Froudian model, Eqs. (3) and (4) need to be fulfilled. The results suggest that a scale factor of internal and foreign forces should be identical. Considering these requirements, it can be written: (i) Eqs. (3) or (4) do not need to be fulfilled at the same time. (ii) Scale factor is different for internal and external forces. (iii) In addition to the precise determination of the structure speed and force scales, it is provided to select the thickness, length and modulus of elasticity scales λ_t, λ_l, and λ_E separately.

In the undistorted Froudian model, the length scale coefficients and the modulus of elasticity are equal. In practical terms, however, it is not possible to build such a model due to the very small, perhaps unrealistic thickness required for the model and the use of a material whose modulus of elasticity is in line with the length scale factor. Low thickness may cause buckling of the structure. These problems are solved by selecting the various scales for length and modulus of elasticity according to a distorted Froudian model. Therefore, despite the fact that with this method, suitable values can be assigned for the thickness and modulus of elasticity of the model, Eqs. (3) and (4) cannot be satisfied simultaneously [15].

3. Jacket Platform Prototype

In this project, the platform model defined in the article [19] was used for modeling. In the oil and gas industry, the structures of this type of platforms are prevalent and even similar to real platforms [20–22]. The steel structure of this platform is 90 meters high and 80 meters deep. The platform jacket has four legs with symmetrical dimensions of 32×32 (m^2) on the seabedand 20×20 (m^2) on the topside. The total dead and live load of the topside is 4850 tons. On the vertical side, the platform has an inverted V shape steel bracing with similar mechanical properties to the footings and horizontal bracing. To consider the effects of soil-pile interaction, the equivalent pile length method was used at a height equal to 8 times the diameter of the pile [23]. Figure 1 displays the perspective of the jacket platform, while Table 1 provides the detailed geometric and mechanical characteristics of the jacket components.

Table 1. Mechanical and geometric characteristics of jacket members [19]

Mechanical	Modulus of elasticity of steel	200,000	MPa
	Poisson ratio	0.3	-
	Yield stress	320	MPa
	Ultimate tension	405	MPa
	Topside mass	4800	tos
	Steel density	7.8n	tons/m^3
Geometric	Horizontal members diameter	1	m
	Horizontal members thickness	0.012	m
	Braces diameter	1.1	m
	Braces thickness	0.012	m
	Legs diameter	1.5	m
	Legs thickness	0.025	m

According to the dynamic equation of motion presented in Eq. (1), the dynamic characteristics of the 5DOF jacket platform system were given in Table 2. By performing modal analysis, the frequencies and contribution coefficients of the first five modes were presented in Table 3. As shown in Figure 3, the natural frequency of the first mode is equal to 1.98 (rad/s).

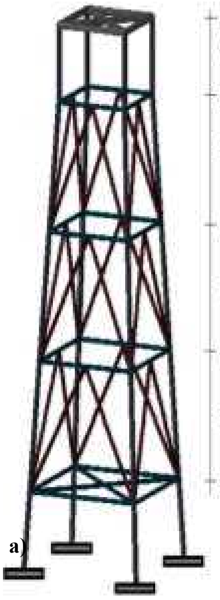

Figure 1. Jacket platform [19]

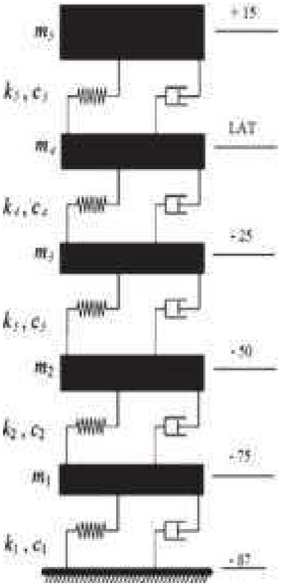

Figure 2. Platform model with an ideal 5DOF system

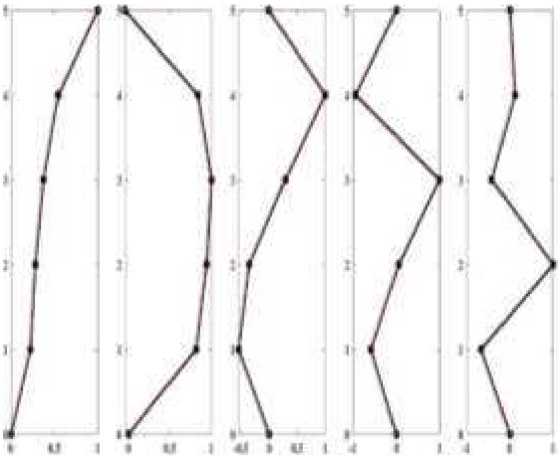

Figure 3. Vibration mode and frequencies of the jacket platform [19]

Table 2. Dynamic characteristics of the 5DOF system of the jacket platform [19]

	Level 1	Level 2	Level 3	Level 4	Level 5
Mass (tons)	220	200	195	130	4850
Stiffness (MN/m)	90	350	210	115	42

$$[M]\{\ddot{x}\}+[C]\{\dot{x}\}+[K]\{x\}=F_e \tag{6}$$

In Eq. 6, the matrices $[M]$, $[C]$ and $[K]$ are the matrices of the mass, damping and stiffness of the jacket structure, and $\{\ddot{x}\}$, $\{\dot{x}\}$ and $\{x\}$ are the acceleration, velocity and displacement vectors, respectively; and F_e is the external force of the earthquake.

Table 3. Modal mass participation percentage (cumulative)

Mode	Frequency (rad/s)	UX	UY	UZ	RX	RY	RZ
1	1.98	45	45	0	0	0	0
2	12.83	90	90	0	0	0	0
3	30.96	90	90	0	0	0	73
4	46.43	92	92	0	6	6	73
5	66.34	94	94	0	8	8	77

To numerically solve Eq. (6), the Simulink module of MATLAB software was used, using the fourth order Runge-Kutta method. In this research, in order to validate and define the jacket platform model (Figure 4), Mousavi et al.'s numerical research [24] has been used.

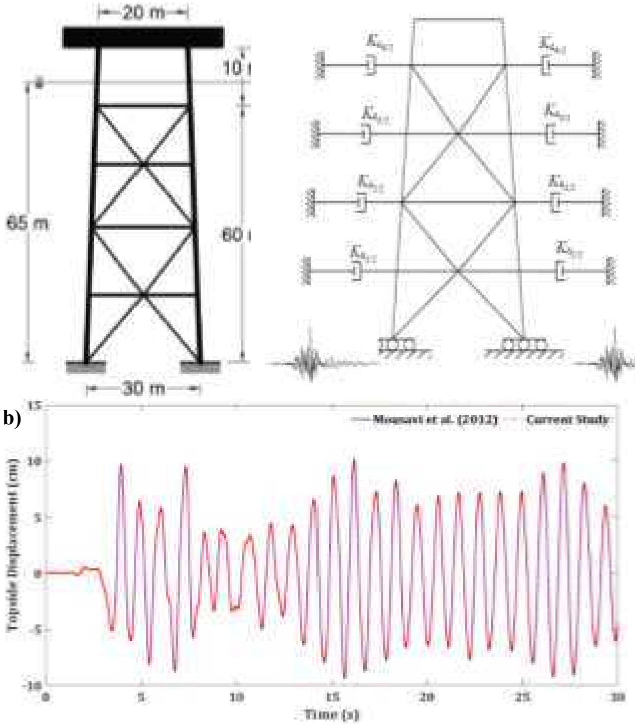

Figure 4. a) Mousavi et al.'s Jacket platform model [24] and b) Comparison of platform topside displacement time history under Kern County earthquake

The density of water was assumed to be 1024 kg/m^3, and the density of steel was 7800 kg/m^3 respectively. The mass and stiffness matrices of the structure as a model of a 5DOF system are presented in Table 4.

Table 4. Dynamic characteristics of the 5DOF system of the research jacket platform [24]

	Level 1	Level 2	Level 3	Level 4	Level 5
Mass (tons)	157	154	151	137	1087
Stiffness (MN/m)	556	444	375	286	67

This jacket platform was investigated with three earthquake accelerations (San Fernando 1971, El Centro, 1940, Kern County 1952 and Northridge 1992). For the structure to be in the linear range during the analysis, the value of earthquake accelerations was scaled to PGA = 0.3g factor. Figure 4b shows the time history of platform topside displacement under the Kern County earthquake. The RMS[3] time histories of platform topside displacement are listed in Table 5 for research [24] and the present study.

According to the results of the analysis of the desired platform with the codes written using MATLAB software (Figure 4b) and according to Table 5, an insignificant difference (less than 5%) was observed between the results, which indicates the accuracy of the method used in this research.

Table 5. RMS response of platform topside

Earthquake	Mousavi et al. (cm)	Current research (cm)	Difference (%)
Kern County	4.89	4.72	3.5
San Fernando	4.38	4.28	2.3
Northridge	5.42	5.36	1.1
El Centro	3.96	3.88	1

4. Modeling of Jacket Platform

For the modeling of the structure, due to the existing limitations for the dimensions of the seismic table, a sample platform made of steel was considered. Based on the dimensions of the shaking table, the first limitation is determining the length scale factor (λ_l). Knowing the λ_l, it is possible to calculate the thickness of the tubular components in a platform model and this will give very small value for its size. On the other hand, for modeling the thickness (λ_t) of the pipe sections used in the platform, due to the lack of construction in very small dimensions, the same length scale factor can not be used. So, it is necessary to increase λ_t as much as possible using the distorted Froudian model. The second important limitation is the determination of the materials of the modeled platform. In order to choose the type of material for the model, it is necessary to use the proportional scaling factor for the modulus of elasticity (λ_E) according to the similarity rules of the distorted Froudian model based on the nature of the problem. Availability, quick and easy construction, strength and low cost are the most important characteristics of model materials. In desktop FDM[4] 3D printing, the most commonly used materials are ABS[5], PLA[6] and PETG[7] 3D printing filaments. The three materials ABS, PLA and PETG differ in many aspects. The difference between them can include tensile strength, density or even application. Table 6 compares the important properties and characteristics of these three filaments [25]. Availability and simplicity of construction and implementation are important factors when choosing materials. In this report, according to Table 6, ABS material was used to build a small-scale platform model [25]. As mentioned earlier, two limitations were raised for platform modeling. The first limitation was the longitudinal scale factor and the second was the material type. However, the third limitation is the amount of thickness of the tubular members of the platform, which is very challenging due to the limitation of making the thickness of the tubes, due to their very small thickness as a result of small scaling. Therefore, it is necessary to distinguish the length scale factor from the scale factor for the thickness of the tubular members. This problem is solved using the method of distorted Froudian modeling.

Table 6. Differences among ABS, PLA and PETG [25]

Properties	ABS	PLA	PETG
Tensile strength	27 MPa	37 MPa	37 MPa
Strain	3.5-50 %	6 %	6 %
Flexural modulus	6.1-7.2 GPa	4 GPa	4 GPa
Density	g/cm^3 4.1-1	1.3 g/cm^3	1.3 g/cm^3
Melting point	200 ℃	173 ℃	173 ℃
Biodegradability	No	Yes, under the right conditions	Yes, under the right conditions
Glass transition temperature	105 ℃	160 ℃	160 ℃
Advantages	More ductility and higher bending strength	Easier to print	High strength and less brittleness
Disadvantages	Harder to print	Low heat resistance	Possibility of scratching

With the coefficients of modulus of elasticity and thickness being known, according Eqs. (1) to (5), density and length coefficients are calculated. These coefficients are presented in Table 7.

Table 7. Modeling scale coefficients

---

[3] Root Mean Square

[4] Fused Deposition Modeling

[5] Acrylonitrile Butadiene Styrene

[6] Polylactic Acid

[7] Polyethylene Terephthalate Glycol

λ_t	λ_E	λ_l	λ_T	λ_p	λ_m
1:35.714	1:70	1:50	1:7.071	1:1.4	1:125000

In Table 7, λ_T is the time scale coefficient and λ_m is the mass scale coefficient. For a better and simpler modeling of the platform structure, the platform model of the article [19] presented in Figure 1 was used. According to the dynamic equation of motion, the dynamic characteristics of the original and modeled jacket platform are given in Table 8. As shown in Figure 3, the frequency of the first vibration mode of the main platform is e qual to 1.98 (rad/s).

Table 8. Dynamic characteristics of the 5DOF system of the jacket platform

Prototype					
	Level 1	Level 2	Level 3	Level 4	Level 5
Mass (tons)	220	200	195	130	4850
Stiffness (MN/m)	90	350	210	115	42
Model					
Mass (kg)	1.76	1.6	1.56	1.04	38.8
Stiffness (KN/m)	36	140	84	46	17

The damping matrix is calculated through the Rayleigh damping equation by considering 2% damping ratios for all vibration modes of the platform [26]. The dynamic characteristics of the original and modeled structure used as equivalent SDOF in the longitudinal direction are presented in Table 9.

Table 9. Dynamic characteristics of the platform of Enferadi et al. [19] as ESDOF

	Fundamental frequency (rad/s)	Mass (kg)	Stiffness (KN/m)	Damping (KN.s/m)
Prototype	1.98	4.94×10^7	1.95×10^5	3929.6
Model	14.05	395.4102	78.1	0.222

5. Results

At first, to check the results of using the ESDOF method for the prototype platform, by applying the four earthquake records mentioned earlier, the time history analysis was performed in the Simulink module of MATLAB software using the fourth order Runge-Kutta method and the results The following was obtained. According to Figures 5 and 6, which are respectively the time history of displacement and acceleration of the platform topside for four earthquake records, a good match was observed between the MDOF and the ESDOF platform.

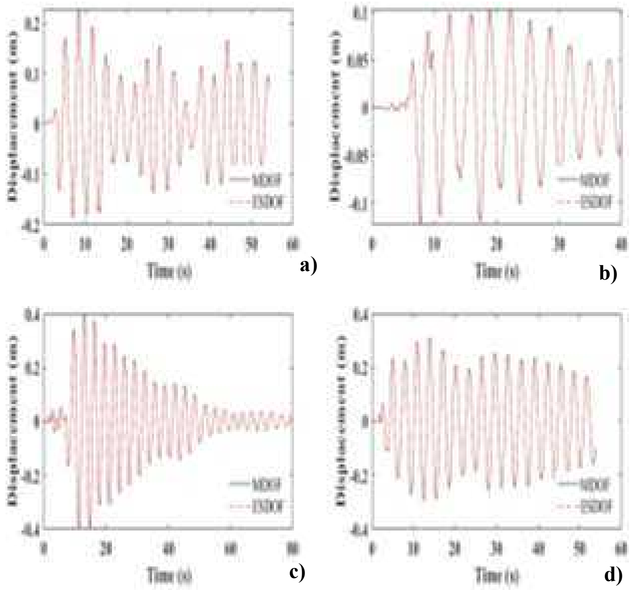

Figure 5. Time history of topside displacement for (a) Kern County, (b) Northridge, (c) San Fernando and (d) El Centro earthquakes

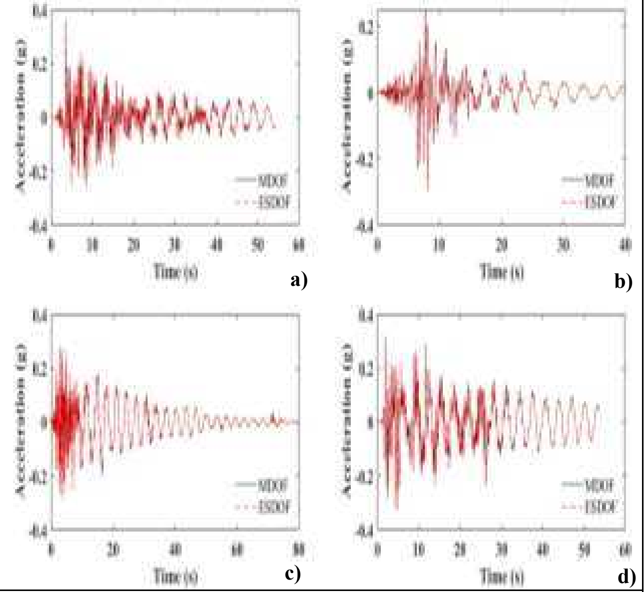

Figure 6. Time history of topside acceleration for (a) Kern County, (b) Northridge, (c) San Fernando and (d) El Centro earthquakes

In order to quantitatively check and compare the results of the time history analysis of the MDOF system and the ESDOF system, the Max[8] and RMS values of the displacement and acceleration of the topside for each of the four earthquake records were averaged and shown in Table 10.

Table 10. Comparison of the prototype MDOF system with the ESDOF system

	MDOF	ESDOF	Error (%)
Max displacement (m)	0.26	0.25	3.8
RMS displacement (m)	0.11	0.105	4.5
Max acceleration (m/s^2)	0.3	0.291	3.3
RMS acceleration (m/s^2)	0.06	0.06	0

According to figures 5 and 6 as well as table 10, it can be seen that a good match is observed for the results of the structure analysis of an equivalent degree of freedom. The errors between the obtained results are below 5%, which is negligible from an engineering point of view.

By using the modeling method of the ESDOF structure, the dynamic characteristics of the modeled structure are presented in Table 9, in Figures 7 and 8, respectively, the time history of the displacement and acceleration of the modeled platform topside with a longitudinal scale factor of 1 to 50, for four Earthquake record is drawn. Since the coefficient of numerical longitudinal scale is smaller than one, therefore, in the modeling of the structure, the duration of the earthquake excitation is also reduced in proportion to λ_l (equal to λ_T). A good match between the MDOF platform and the modeled ESDOF platform is observed.

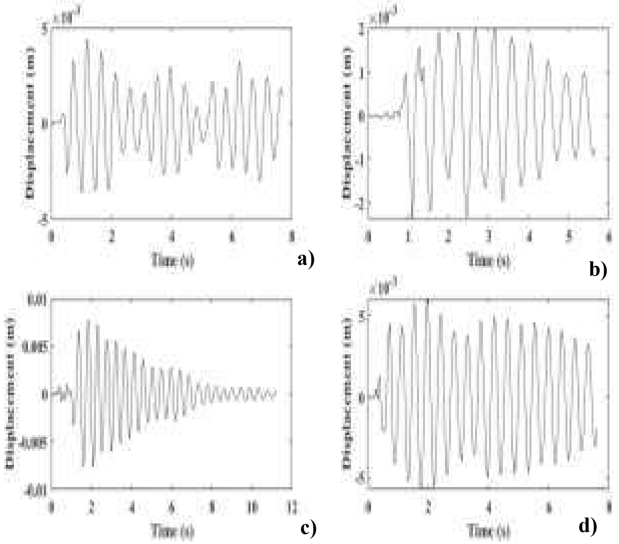

Figure 7. Modeled topside displacement time history for (a) Kern County, (b) Northridge, (c) San Fernando and (d) El Centro earthquakes

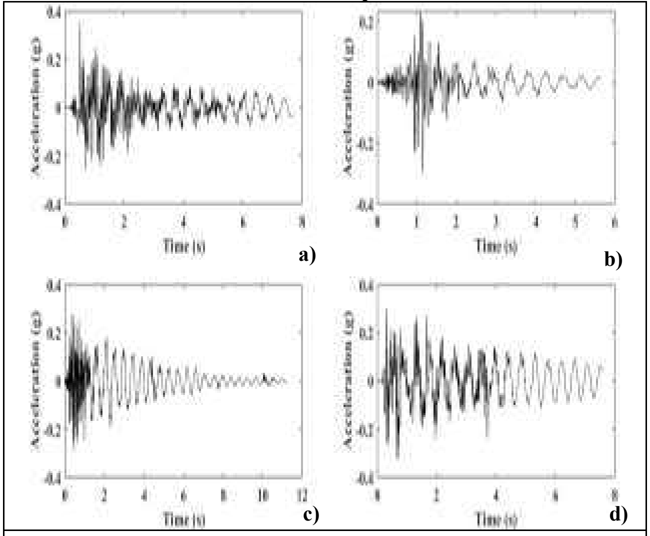

Figure 8. Modeled topside acceleration time history for (a) County, (b) Northridge, (c) San Fernando and (d) El Centro earthquakes

---

[8] Maximum

As can be seen in Figures 7 and 8, the values of the range of changes in the diagrams are proportional to the scale factor defined for the main model of the platform. To investigate this issue quantitatively, the Max and RMS values of displacement and acceleration of the topside for each of the four earthquake records were averaged and shown in Table 11.

Table 11. Responses of the modeled ESDOF system

	Max. displacement (m)	RMS displacement (m)	Max. acceleration (m/s^2)	RMS acceleration (m/s^2)
ESDOF	0.005	0.0021	0.291	0.06

For a more detailed investigation and comparison of the structure modeling method using the distorted Froudian method (DF) with the modeled ESDOF structure, in Figures 9 and 10, respectively, the time history of the displacement and acceleration of the modeled platform topside is drawn for four earthquake records, which indicates the good agreement of the results obtained with both methods.

For quantitative analysis, the Max and RMS values of displacement and topside acceleration for both modeling methods under each of the earthquake records were averaged and shown in Table 12.

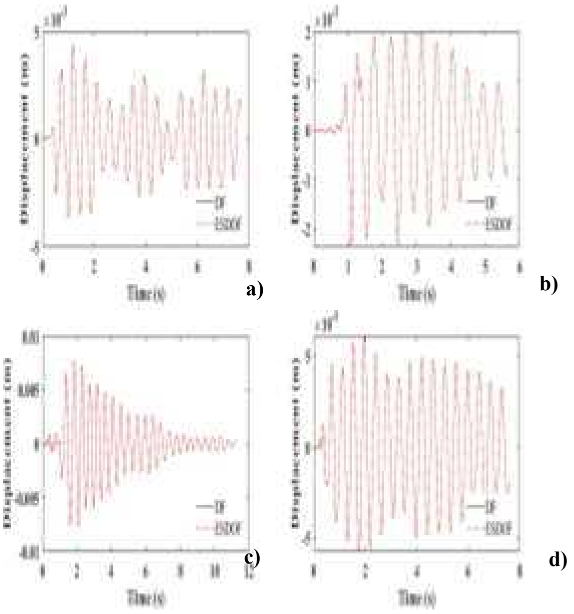

Figure 9. Comparison of the topside displacement time history of the DF with the ESDOF for the (a) Kern County, (b) Northridge, (c) San Fernando and (d) El Centro earthquakes

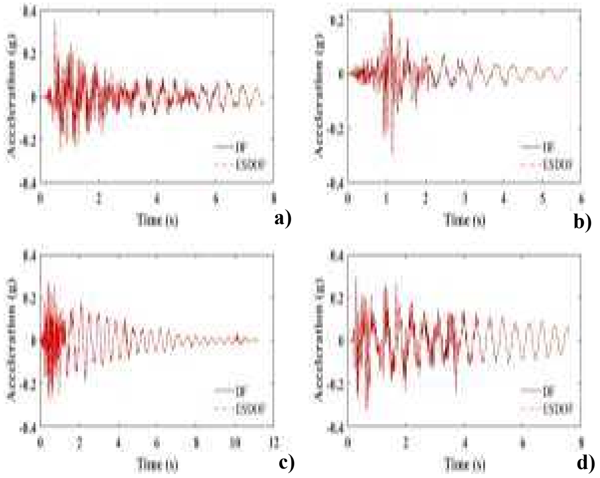

Figure 10. Comparison of the topside acceleration time history of the DF with the ESDOF for the (a) Kern County, (b) Northridge, (c) San Fernando and (d) El Centro earthquakes

Table 12. Comparison of the results of the modeled platform

	DF	ESDOF	Difference
Max displacement (m)	0.0052	0.005	3.8 %
RMS displacement (m)	0.002	0.0021	4.5 %
Max acceleration (m/s^2)	0.3	0.291	3.3 %
RMS acceleration (m/s^2)	0.06	0.06	0

As mentioned earlier, to use the technique of an ESDOF system, it is very important and decisive to determine the vibration modes and the corresponding frequencies. In Figure 11, the mode shapes for both the DF and the ESDOF are drawn and compared with each other. As shown in Figure 11, a perfect match is observed for the mode shapes for both methods.

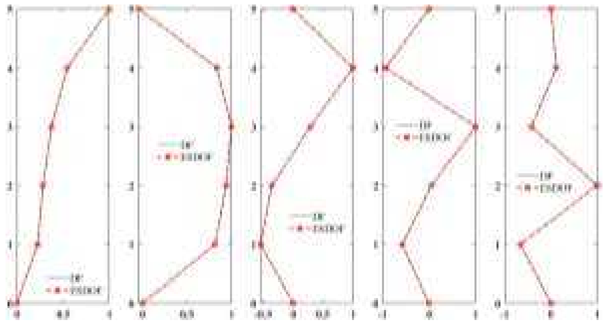

Figure 11. Vibration mode shapes and frequencies of the DF and ESDOF jacket platform

6. Conclusion

In this article, two methods were proposed for the physical modeling of the offshore jacket platform. In the first method, which is called Distorted Froudian (DF) modeling, the modeling parameters for an offshore platform under seismic loading were investigated and the platform was modeled in a small scale. For three parameters: length geometry, thickness geometry, and material geometry, and corresponding coefficients for time, mass, and stiffness of the members, the DF model method has been used due to operational constraints on the construction of tubular members of the platform, in particular for thickness. In the second modeling method, which is called the Equivalent Single Degree of Freedom (ESDOF) system method, the structure is modeled as a single degree of freedom system for simplicity of analysis and especially model construction. It is necessary to explain that the use of the ESDOF method has a very important condition that the mass contribution coefficient of the first mode should be more than 90%. A verification of the Mousavi's platform model [24] was used, and by analyzing the mentioned structure, the accuracy of the numerical analysis method, which was with Simulink of MATLAB, and the accuracy of the written codes were obtained. To verify that the two proposed modelling methods are accurate, Enferadi et al.'s offshore jacket platform model [19] was used. For modeling, scale factors of 1 to 50 for length, 1 to 70 for modulus of elasticity, 1 to 35.714 for thickness, 1 to 1.4 for density, and 1 to 71.071 for time were used. The qualitative and quantitative results showed the correctness and precision of the physical modeling methods for this study. Since the construction of the accompanying laboratory model has many problems and complications, for the structures that have a mass contribution coefficient of more than 90% for the first mode, for the simplicity of the model construction, the entire structure can be a simple ESDOF structure is modeled where the frequency of the first mode of the MDOF structure is equal to the frequency of the SDOF structure. Finally, the results of this research can be summarized as follows:

1) Distorted Froudian (DF) Model:
   - These models address issues related to geometric features and other specifications.
   - By allocating different scale coefficients, they solve problems like unreality due to applying certain scale factors (e.g., thickness of tubular members).
2) Equivalent Single Degree of Freedom (ESDOF) System:
   - In this method, the structure is simplified to behave like a single mass-spring-damper system.
   - The first mode (vibration mode) dominates the system response (more than 90% mass participation).
   - This simplification makes laboratory construction easier.

Both methods demonstrated excellent accuracy and ESDOF system proved efficient under defined specific conditions.

7. Acknowledgement

The authors highly appreciate the assistance of Pars Oil and Gas Company of Iran (Contract No. 03-01-د ف پ) regarding.

8. References

[1] Xu Y, Liu Y, Kan C, Shen Z, Shi Z. Experimental research on fatigue property of steel rubber vibration isolator for offshore jacket platform in cold environment. Ocean Eng 2009;36:588–94. https://doi.org/10.1016/j.oceaneng.2009.02.002.

[2] Sharp JJ. Hydraulic modelling. Butterworth Co Ltd 1981. https://doi.org/10.1201/9780429440816-8.

[3] Boccotti P. Wave mechanics for ocean engineering. Elsevier.; 2000.

[4] Asgarian B, Lesani M. Pile-soil-structure interaction in pushover analysis of jacket offshore platforms using fiber elements. J Constr Steel Res 2009;65:209–18. https://doi.org/10.1016/j.jcsr.2008.03.013.

[5] Gomathinayagam S, Vendhan CP, Shanmugasundaram J. Dynamic effects of wind loads on offshore deck structures - A critical evaluation of provisions and practices. J Wind Eng Ind Aerodyn 2000;84:345–67. https://doi.org/10.1016/S0167-6105(99)00113-0.

[6] Winsor F. Evaluation of methods to remove inertial force from measured model wave impact force signals. Ocean Eng 2003;30:47–84. https://doi.org/10.1016/S0029-8018(02)00012-4.

[7] Elshafey AA, Haddara MR, Marzouk H. Dynamic response of offshore jacket structures under random loads. Mar Struct 2009;22:504–21.https://doi.org/10.1016/j.marstruc.2009.01.001.

[8] Bargi K, Hosseini SR, Tadayon MH, Sharifian H. Seismic Response of a Typical Fixed Jacket-Type Offshore Platform (SPD1) Under Sea Waves. Open J Mar Sci 2011;01:36–42. https://doi.org/10.4236/ojms.2011.12004.

[9] Trung NT. EEMD-HT transform for identifying modal parameters of fixed offshore jacket platforms using vibration response measurement. J Civ Struct Heal Monit 2020 ;10:883–97. https://doi.org/10.1007/s13349-020-00422-3.

[10] Walia D, Schünemann P, Hartmann H, Adam F, Großmann J. Numerical and physical modeling of a tension-leg platform for offshore wind turbines. Energies 2021;14. https://doi.org/10.3390/en14123554.

[11] Erfani MH. Structural Integrity Assessment of Offshore Jackets Considering Proper Modeling of Buckling in Tubular Members—a Case Study of Resalat Jacket. J Mar Sci Appl 2022; 21:145–67. https://doi.org/10.1007/s11804-022-00307-5.

[12] Ou J, Long X, Li QS, Xiao YQ. Vibration

control of steel jacket offshore platform structures with damping isolation systems. Eng Struct 2007;29:1525–38. https://doi.org/ 10.1016/j.engstruct.2006.08.026.

[13] Hosseinlou F, Hokmabady H, Mojtahedi A, Mohammadyzadeh S. Seismic Analysis of an Offshore Structure in Persian Gulf Utilizing a Physical Model. Int J Marit Technol 2019;11 :21–31. https://doi.org/10.29252/ijmt .11.21.

[14] Leng D, Zhu Z, Xu K, Li Y, Liu G. Vibration control of jacket offshore platform through magnetorheological elastomer (MRE) based isolation system. Appl Ocean Res 2021;114: 102779. https://doi.org/10.1016/j.apor.2021.102779.

[15] Shumin C, Swamidas ASJ, Sharp JJ. Similarity method for modelling hydroelastic offshore platforms. Ocean Eng 1996;23:575–95. https://doi.org/10.1016/0029-8018(95)00050-X.

[16] Leng D, Lv P, Zhu Z, Li Y, Liu G. Experimental study on semi-active magnetorheological elastomer based isolation system for offshore platform using wave tank. Ocean Eng 2024;292. https://doi.org/10.1016 /j.oceaneng.2023.116467.

[17] Leng D, Zhu Z, Liu G, Li Y. Neuro fuzzy logic control of magnetorheological elastomer isolation system for vibration mitigation of offshore jacket platforms. Ocean Eng 2022 ;253:111293.https://doi.org/10.1016/j.oeaneng. 2022.111293.

[18] Chakrabarti SK. Offshore Structure Modeling. vol. 9. 1994.

[19] Enferadi MH, Ghasemi MR, Shabakhty N. Wave-induced vibration control of offshore jacket platforms through SMA dampers. Appl Ocean Res 2019;90:101848. https://doi.org/ 10.1016/j.apor.2019.06.005.

[20] Edalat P, Bagherinia M. A Knowledge Based Decommissioning Alternative Selection System for Fixed Offshore Oil and Gas Platforms in Persian Gulf. Int J Coast Offshore Eng 2018;2:45–55. https://doi.org/10.29252 /ijcoe.2.2.45.

[21] Sadian R, Taheri A. In-Place Strength Evaluation of Existing Fixed Offshore Platform Located in Persian Gulf with Consideration of Soil-Pile Interactions. Int J Coast Offshore Eng 2016;2:35–42.

[22] Mohasel M, Mostafa Gharabaghi AR, Chenaghlou MR. Presenting an optimal design procedure for a variety of TLCDs to improve the seismic response of offshore platforms. Comput Eng Phys Model 2023;6. https://doi.org/10.22115/CEPM.2024.428789.1265.

[23] N.D.P. Barltrop and A.J. Adams. Dynamics of Fixed Marine Structures. 1991. https://doi.org /10.1016/c2013-0-04571-9.

[24] Mousavi SA, Zahrai SM, Bargi K. Optimum geometry of tuned liquid column-gas damper for control of offshore jacket platform vibrations under seismic excitation. Earthq Eng Eng Vib 2012;11:579–92. https://doi.org/ 10.1007/s11803-012-0143-z.

[25] https://madatech.co/ n.d. https://madatech.co/.

[26] Sarrafan A, Zareh SH, Khayyat AAA, Zabihollah A. Neuro-fuzzy control strategy for an offshore steel jacket platform subjected to wave-induced forces using magnetorheological dampers. J Mech Sci Technol 2012;26:1179–96. https://doi.org/10 .1007/s12206-012-0212-2.

Available online at: www. Ijcoe.org

Analyzing the Impact of Non-Dimensional Hydrodynamic Coefficients on the Performance of Oscillating Wave Surge Converters

Ghazale Sadripour[1], Rouzbeh Shafaghat[2*], Behrad Alizadeh Kharkeshi[3]

[1] PhD student in Mechanical Engineering, Sea-Based Energy Research Group, Babol Noshirvani University of Technology, Babol, Iran, ghazale.sadripour@gmail.com

[2] Professor in Mechanical Engineering, Sea-Based Energy Research Group, Babol Noshirvani University of Technology, Babol, Iran, rshafaghat@nit.ac.ir*

[3] Assistant Professor in Mechanical Engineering, Sea-Based Energy Research Group, Babol Noshirvani University of Technology, Babol, Iran, b.alizadeh@nit.ac.ir

ARTICLE INFO

Article History:
Received:26 Oct 2024
Accepted: 06 Aug 2025
Available online ….

Keywords:
Renewable energy
Caspian Sea
OWSC
Experimental study
Frequency

ABSTRACT

Applying renewable energy could decrease the side effects of fossil fuels, therefore wave energy converters are crucial for implementing. This study focuses on the experimental investigation of an OWSC (1:8) by considering Caspian Sea for installation. After defining the significant hydrodynamic coefficients that impact the performance of the OWSC, including damping, pressure, and transmission coefficients, this study identified the parameters influencing these coefficients and investigated how these parameters affected them. The experiments were designed within the range of wave heights [0.04-0.1] m, wave frequency [0.4-0.63] Hz and water depths [0.8-1.5] m. Previous studies have shown that draft depth, wave height, and wave frequency are parameters affecting the performance of WEC. In this paper, the effect of these parameters on the hydrodynamic coefficients of the WEC was investigated. The results showed that increasing the wave height decreases the damping coefficient of the WEC, it was also shown that the effect of the dimensionless draft depth on the damping coefficient has a non-linear behavior and the WEC has the lowest damping coefficient at the optimal draft depth. An increase in the wave height leads to a decrease in the pressure coefficient (Cp), the Cp decreases by approximately 40% when the wave height changes from 0.04 to 0.1 m. The effect of the dimensionless wave frequency on the Cp is insignificant. Increasing the dimensionless draft depth leads to an increase in the transfer coefficient (Ct). Furthermore, the results of the correlation between parameters and Hydrodynamic coefficients indicate correlation of approximately -1 between wave height and Cp, close to -1 between wave height and Cd, and a close to 0 between wave height and Ct.

1. Introduction

In recent years, several energy sources have been introduced and are being exploited. The growth in population, the rise in energy demand, limitations of fossil fuel resources, and the problems associated with their consumption, such as increased CO2 emissions in the atmosphere, climate change, global warming, etc., have led scientists to utilize clean and renewable energy sources. Among these sources such as solar energy, wind energy, biomass energy, geothermal energy, and wave energy can be mentioned. Between the mentioned renewable energies, wave energy is particularly notable due to its advantages such as high energy density, significant storage capacity, lack of pollution, and preservation of underground resources [1]. With two-thirds of the Earth's surface covered by oceans, harnessing ocean energy could be an important source of green energy for coastal communities [2]. The essential requirement for absorption of wave energy is the presence of a device capable of absorbing the maximum amount of energy from the waves upon their impact. In the world of renewable energies, WECs are among the newest technologies [3]. WECs come in various types, and each of these WECs utilizes a different range of power generation mechanisms. OWSC is a novel WEC designed to be installed in near shore and shallow water areas (depth of 10-20 m). In shallow waters, the motion of water particles is predominantly horizontal. OWSCs are specifically designed to effectively interact with the horizontal movement of particles, allowing for a large amplitude of motion working surface area and minimizing energy losses. The OWSC consists of a flap that rotates around a horizontal axis, either above the water surface or near the seabed, perpendicular to the direction of wave propagation [4]. Lots of research has been carried out on wave energy, and in most cases, energy extraction systems have been developed on a laboratory scale. These systems have been tested under simulated ocean conditions, and some of them have progressed to the operational phase. Drew et al. [5] in 2009, investigated the overall status of wave energy, specifically focusing on the various WEC technologies, with an emphasis on projects being carried out in the United Kingdom. Babarit et al. [6] in 2012, by analyzing the annual power output of several converters, were able to extract cost-related performance parameters. Renzi and Dias [7] in 2013 conducted an analytical study of an OWSC, utilizing a semi-analytical model of the potential flow. They derived correlations between the hydrodynamic parameters of the system through their study. Their parametric study showed that the excitation torque and added moment of inertia increase with a growing in flap width. Their results also demonstrated that an increase in flap width has a significant impact on the energy absorption coefficient. Sarkar et al. [8] in 2013 analytically investigated the OWSC efficiency by considering six different wave conditions. The modeling was performed using the potential flow theory and Green's theorem. They conducted a comparison between the performances of two WECs with different widths. The results indicate the importance of width on the power capture. A WEC with a smaller width has a higher power capture coefficient under the effect of waves with a shorter wavelength. This is because the excessive widening of a WEC limits its energy absorption under the effect of waves with a short wavelength. Furthermore, due to increased added moment of inertia, a flap with a larger width has a higher power capture coefficient under the effect of waves with longer wavelengths. Wei et al. [9] in 2013 proposed the use of finite volume and dynamic mesh methods to simulate wave forces on an OWSC exposed to waves. The outcomes revealed that the numerical model with dynamic mesh can be used for modeling the motion large amplitude of a flap. Renzi et al. [10] in 2014 performed numerical and semi-analytical modeling (inviscid potential flow theory) OWSC arrays in wave energy farm. They calculated the hydrodynamic parameters and system performance in different configurations using both models. They found that using the second model allows for the investigation of resonance phenomena. They also showed using the second model that the symmetrical arrangement of transducers has a higher performance than their asymmetrical model in a wave farm. Chang et al. [11] in 2015 conducted a theoretical study (two-dimensional potential theory) on wave energy absorption by an OWSC in order to examine it. They utilized the obtained results to validate their SPH simulations, demonstrating that the SPH method is a reliable approach for the design and optimization of an OWSC. Ferrer et al. [12] in 2016 conducted a numerical investigation on the slamming wave effect on the OWSC using the OpenFOAM software. They investigated the effects of fluid compressibility in the flow by employing both compressible and incompressible flow assumptions and compared the obtained results. The results indicated that the incompressible flow assumption provided sufficient accuracy, and there was no need to use the compressible flow assumption, given appropriate discretization. Wilkinson et al. [13] in 2017 conducted an experimental investigation on an an OWSC (1:30) with a modular flap under regular waves, comparing it with an OWSC with a rigid flap. In this model, they used the simplest form of damping, which is uniform damping for each module (each component of the flap). They demonstrated that the modular structure for the OWSC has advantages such as improved WEC performance, reduced forces on the foundation, and decreased construction and installation costs. The modular flap generates 23% more total power compared to the equivalent rigid flap. Jiang et al. [14] in 2018 investigated the hydrodynamic response of an OWSC along with various linear and nonlinear PTO systems. They also optimized the performance of the PTO systems aiming to enhance the performance of an OWSC, for this purpose, they employed a PTO simulation platform capable of generating different types of damping forces. The comparison of the WEC's efficiency under linear and nonlinear PTO damping has shown that the nonlinear PTO does not provide a significant advantage in power output. However, it exhibits better stability. Brito et al. [15] in 2019 examined the performance of an OWSC using numerical simulations in the SPH software, taking into account existing mechanical constraints, including the PTO system's compliance and flap inertia. The results indicated that the simulated numerical model accurately predicts the dynamics of the WEC. Brito et al [16] also in 2020 studied the 1:10 scale OWSC experimentally, taking into account the effects of the PTO system. Additionally, they proposed a mathematical model for PTO, The results indicated a weak correlation between the WEC's performance and its hydrodynamic response. Therefore, it does not necessarily imply that the maximum performance coincides with the peak hydrodynamic response. Liu et al. [17] in 2020 conducted a numerical investigation on cylindrical OWSC under the influence of regular waves using the SPH method. They initially performed a comparison between the performance of cylindrical and rectangular flaps. It was determined that cylindrical flaps exhibit higher efficiency. Then, they proceeded to investigate the effects of five parameters on the WEC's performance, these parameters included the total mass of the flap, the distance between the Hinge and seabed, the damping of the PTO system, and the thickness of the flap. The numerical results indicated that the higher mass of the flap, thinner thickness, and more distance between the hinge and seabed contribute to improving the performance of the WEC. They also demonstrated that by increasing the damping of the PTO system, the WEC's performance initially increases and then decreases. Cheng et al. [18] in 2020 conducted a numerical study on an OWSC, including power extraction, efficiency, and hydrodynamic response. They found that as the wave amplitude increases, the hydrodynamic response amplitude operator (RAO) and performance decrease. Their results also showed that appropriate design of the hydrodynamic coefficients can create a resonance region, which can be beneficial in achieving maximum effective performance. Liu et al. [19] in 2022 studied the resonance phenomenon in an OWSC under regular waves using the boundary element method and investigated the correlation between the resonance phenomenon and the WEC's capture width ratio (CWR). The results showed that the maximum power absorption period is closer to the maximum angular velocity period than the natural period of the flap, and thus the maximum CWR does not occur during the resonance phenomenon. This paper provides an experimental analysis of the performance of an OWSC (1:8) specifically designed for the Caspian Sea. Given that most studies are conducted without accounting for scaling factors, this study investigates the performance and hydrodynamic behavior of the WEC at optimized draft depth by analyzing the pressure, damping, and transmission coefficients. Furthermore, the effect of wave characteristics and draft depth on the hydrodynamic coefficients were also investigated in terms of correlation.

2. System Description

2.1. Physical model

OWSC system has been designed and constructed. A schematic view of the system located in the wave flume of the Sea-Based Energy Research Group at Babol Noshirvani University of Technology has been shown in figure 1 [20] wave prob and system's dimensions have been presented by authors in [21, 22]. The PTO system and it's components are also showed in figure 2.

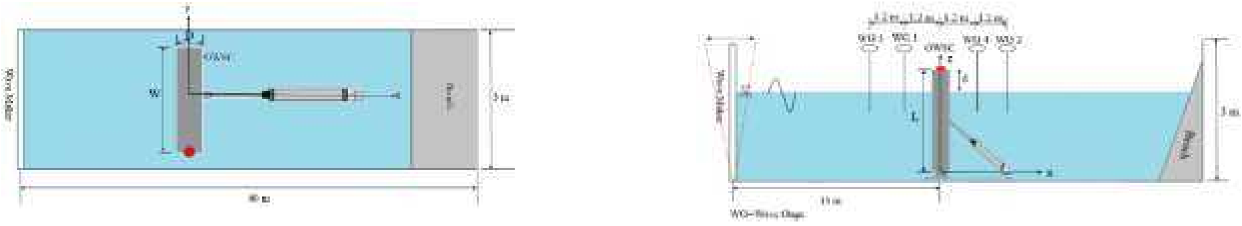
(a)
(b)

Figure 1. a model of an OWSC in a wave flume. a) top view b) side view


(a)
(b)

Figure 2. a) a view showing the OWSC model b) schematic of OWSC and PTO system

To measure the angular displacement of the flap (θ), a tracker index has been used on the flap and a camera. It should be noted that the camera is installed in a suitable location with sufficient range to capture the large range of flap displacements. The location of the camera and other measuring equipment can be seen in Figure 3.

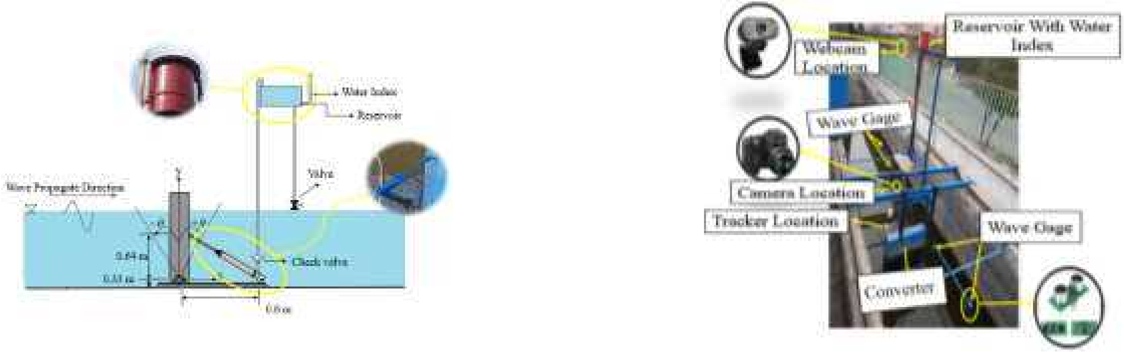

Figure 3. Location of camera and other measuring equipment

Figure 4. Views showing the OWSC model

In Figure 4, views of the OWSC model can be seen. For get more information about the system description, can refer to another work of the author [23].

3. Experimental Study

Froude scaling can be used to simulate the conditions of sea waves on a laboratory scale; according to the study conducted by Alamian et al. [24] on the conditions of waves in Caspian Sea, the selected wave conditions were a wave period range of [4-6] s and a wave height range of [0.5-1] meters, representing waves with the highest energy density.

Table 1. Laboratory conditions of waves

Frequency (Hz)	Wave height (m)	Depth (m)
0.4		0.8
0.43		0.9
0.47	0.04	1
0.50	0.06	1.1
0.53	0.08	1.2
0.57	0.1	1.3
0.60		1.4
0.63		1.5

Using Froude scaling, these conditions were converted to laboratory scale, the design parameters of the test were considered as Table 1.

4. Experimental Modeling

Based on the conducted studies, the parameters that affect the performance of an OWSC have been identified as the wave height (Hi), the pressure difference created in the PTO system (Δp), the flow rate in PTO system (Q), and the angular displacement (θ) (Eq.(1)):

$$P_{OWSC} = f(h, H_i, \theta, g, \rho, \Delta p, Q, d) \tag{1}$$

Where d represents the hydraulic cylinder diameter, ρ denotes the water density, and g refers to the gravitational acceleration. After the non-dimensionalization of the variables using the Pi-Buckingham theory, the following dimensionless hydrodynamic coefficients were extracted.

$$C_d = \frac{d^2 \sqrt{\frac{\Delta P}{\rho}}}{Q} \tag{2}$$

$$C_P = \frac{\Delta P}{\rho g H_i} \tag{3}$$

$$C_t = \frac{h\theta}{H_i} \tag{4}$$

Dimensionless damping coefficient of the OWSC (Cd), Where Cd is the dimensionless damping coefficient of the OWSC; the Cd shows the relationship between flow rate and pressure in the PTO system. Dimensionless pressure coefficient has been shown by Cp and indicates the relationship between pressure inside the PTO system and incidence wave conditions, and the dimensionless transmission coefficient (Ct) shows the relationship between flap motion range and incidence wave conditions.

5. Governing Equations

In this section, the equations used to calculate each of the parameters are presented. In order to calculate the pressure difference created in the PTO system, Eq. (5) is used.

$$\Delta P = \frac{1}{2}\rho\left({V_1}^2 - {V_2}^2\right) + \rho g h' \qquad (5)$$

Where V_1 is the water velocity at the reservoir inlet, V_2 is the water velocity in the reservoir, and h' is the distance between the reservoir and the fluem bed. The equations used to calculate Q (the flow rate pumped by the PTO system) are presented in another paper of this study [23]. To calculate θ, the Tracker software, which is a software for analyzing physical motion in video files, was used; since the displacement obtained by the Tracker software is in centimeter, Eq. (6) was used to find the displacement angle in radians from the rotation radius (r):

$$\theta(rad) = \frac{y(cm)}{r(cm)} \qquad (6)$$

6. Laboratory Equipment and Data Collection

The equipment used in this study includes the ultrasonic sensor US-100, a camera, and a webcam. The specifications of these equipment are listed in Table 2; more information about these equipment, as well as their calibration and uncertainty, can be found in reference [23].

Table 2. Specifications of measurement equipment used

Image	Accuracy	Measurement Equipment
	Zoom: ×34 Precision: 921000 pixels Focal range: 5.22 to 765 millim	Video camera Nikon coolpix L830
	Distance: 2 to 450 cm precision: 1 mm	US-100 sensor
	Film speed: 30 FPS	ROTEL-RW120 web camera

7. Results and Discussion

In this section, three important dimensionless hydrodynamic coefficients, including the damping, pressure, and transmission coefficients, are evaluated to investigate the performance of an OWSC. These coefficients are calculated at each draft depth and the effects of changing the draft depth and wave conditions including wave height and frequency, are examined. For this purpose, the dimensionless parameters of draft depth $(\frac{d}{h})$ and wave frequency $(f = \frac{H\omega^2}{g})$ were used. The results indicate [23] that the WEC has higher performance at wave frequency and dimensionless draft depth (water depth) of 0.4 Hz and 0.59 (0.9 m). Therefore, in this section, with the aim of investigate the effects of changing water depth and wave height on the hydrodynamic coefficients of the WEC, the wave frequency is considered constant at 0.4 Hz. Furthermore, to evaluate the effect of wave frequency and wave height on these coefficients, the water depth was fixed at 0.9 meters. Damping coefficient is a measure of flow rate in PTO system. Figure 5 shows the effect of dimensionless draft depth on the C_d at different wave heights; as shown in Figure 5, there is a parabolic nonlinear relationship between the dimensionless draft depth and the C_d. Also it can be observed that at the optimal dimensionless draft, The value of C_d is minimum. This point indicates that reducing the damping coefficient at the optimal draft depth leads to improved performance of the WEC. Alternatively, rising the height of the wave results in a decrease in the C_d. The important point is that in the characteristic range of Caspian Sea waves, meaning low wave height, the damping coefficient of the WEC is higher than in seas with high wave height.

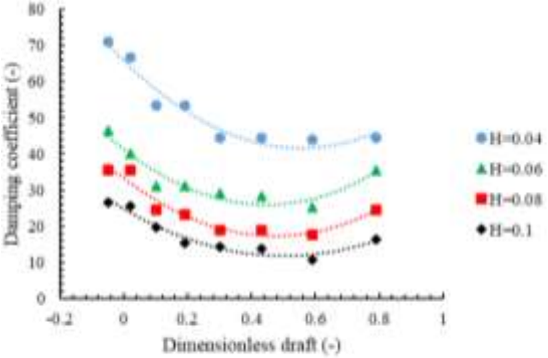

Figure 5. Dimensionless draft depth effect on damping coefficient

Figure 6 shows the variations of the pressure coefficient of the WEC with the change of dimensionless draft depth in different wave heights. As can be seen from the figure, the effect of the dimensionless draft depth on C_p is negligible, but the increase in wave height leads to a decrease in the C_p; the reason for this is that the pressure coefficient is inversely related to wave height and directly related to pressure changes within the WEC. Since the effect of the wave height is greater than the effect of pressure changes within the WEC, an increase in the wave height leads to a change in the pressure coefficient. The reason for this is that the C_p has an inverse relationship with the wave height and a direct relationship with the pressure change inside the WEC, since the effect of wave height is greater than the effect of pressure changes within the WEC, an increase in wave height results in a change in the C_p.

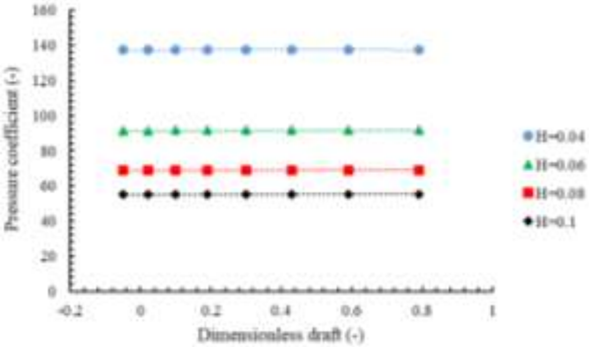

Figure 6. Dimensionless draft depth effect on pressure coefficient

One of the important dimensionless hydrodynamic coefficients in this study is the transmission coefficient of the WEC. Figure 7 shows the changes in the transmission coefficient with the change of dimensionless draft depth in different wave heights. As can be seen from Figure 7, an increase in the dimensionless draft depth leads to an increase in the transmission coefficient of the WEC. It is important to note that the C_t at the optimal dimensionless draft depth has larger values compared to other draft depth.

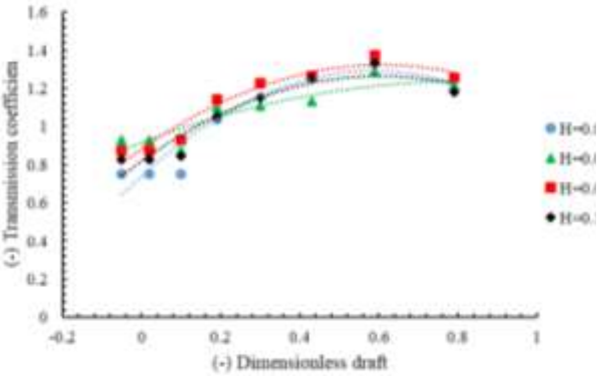

Figure 7. Dimensionless draft depth effect on transmission coefficient

In the following, the water depth is constant; the relationship between the dimensionless wave frequency and the C_d is shown in Figure 8. The results show that as the dimensionless wave frequency increases, C_d increases, one of the reasons for this is that with an increase in frequency, the WEC loses its ability to adapt to the wave and cannot complete a full Course of rotation.

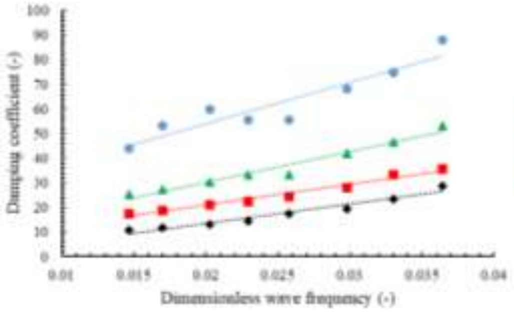

Figure 8. Dimensionless wave frequency effect on damping coefficient

Figure 9 examines the effect of dimensionless wave frequency on the C_p. It can be concluded that the dimensionless wave frequency has not much effect on the C_p, but the change in the wave height can be effective by considering the wave height in the denominator. As a result, the pressure coefficient decreases by approximately 40% when the wave height changes from 0.04 m to 0.1 m.

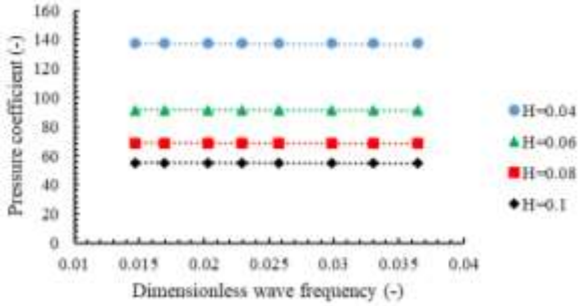

Figure 9. Dimensionless wave frequency effect on pressure coefficient

Figure 10 shows the effect of dimensionless wave frequency on the transmission coefficient. From Figure 10, it can be seen that the C_t decreases with increasing dimensionless wave frequency. This decrease is more severe at the lowest wave height than at other heights. On the other hand, if the wave height is between 0.06 m and 0.08 m, the transmission coefficient has higher values than at other wave heights.

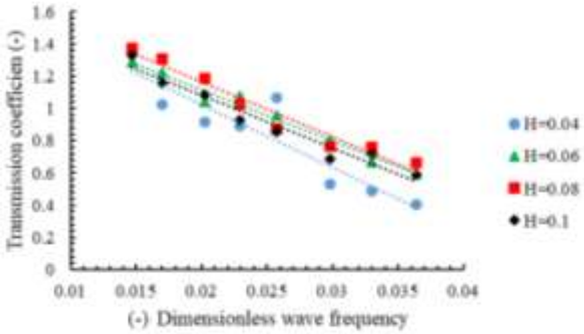

Figure 10. The effect of the dimensionless wave frequency on the transmission coefficient

Given the importance of the transmission coefficient of the WEC, its average values at different wave heights have been calculated and are presented in Figure 11. It is found that changes in wave height can cause nonlinear behavior in the C_t. The C_t is small for both low and high wave heights, while it reaches its maximum value in the range of 0.07-0.08 m wave height. This point is essential from a structural considerations as it indicates that in the design of the structure, the flap displacement should be considered for this range of wave heights, rather than only for the maximum wave height.

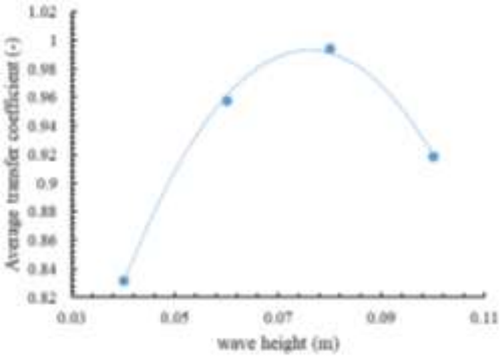

Figure 11. Variation of the transmission coefficient with wave height

To investigate the relationship between two parameters, their correlation can be examined. As shown, if the correlation is close to one, the two parameters are strongly directly related, meaning that an increase in one parameter or variable leads to an increase in the other variable. If the correlation is close to -1, the two parameters have an inverse relationship. This section presents the correlation between dimensionless draft depth, wave height, and the damping, pressure, and transmission coefficients, as shown in Table 3. Table 3(a) shows the negative correlation between the dimensionless draft depth and the C_d, indicating that an increase in draft depth results in a decrease in damping. Additionally, a stronger negative correlation is observed between wave height and C_d, which is 54% stronger. In Table 3 (b), the correlation between the dimensionless draft depth, wave height, and pressure coefficient is shown. The C_p has a very low correlation with the draft depth, almost equal to zero, meaning that the change in the dimensionless draft depth does not have much effect on the C_p. However, the correlation between wave height and the C_p is negative, near -1, indicating that the C_p decreases significantly as wave height increases.

Table 3. The correlation between the dimensionless submergence depth and collision wave height with coefficients a) transmission, b) pressure, c) damping

(a)

	d/h	**Ct**	**H**
d/h	1.000		
Ct	0.813	1.000	
H		0.070	1.000

(b)

	d/h	**Cp**	**H**
d/h	1.000		
Cp	0.001	1.000	
H		-0.965	1.000

(c)

	d/h	**Cd**	**H**
d/h	1.000		
Cd	-0.337	1.000	
H		-0.844	1.000

To better examine the correlation values for wave height and dimensionless draft depth separately, Figure 12 has been plotted; it is clear that the correlation between wave height and C_t is close to zero, and between wave height and C_d and C_p is close to -1. This indicates the importance of the wave height for the C_d and C_p and its low importance for the C_t. One of the important points in this figure is the high dependence of the transmission coefficient and damping coefficient (compared to the C_p) on the dimensionless draft depth and the lack of correlation between the C_p and the dimensionless draft depth.

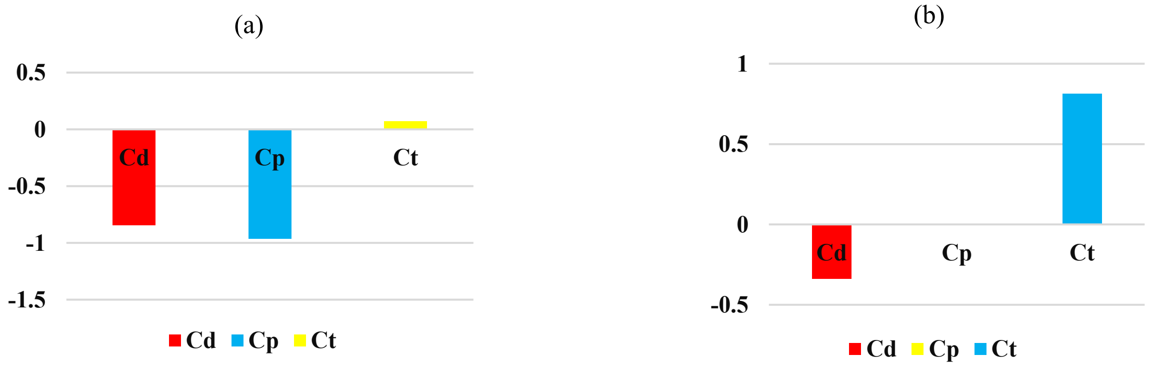

Figure 12. The correlation between a) wave height with damping, pressure, and transmission coefficients, b) dimensionless draft depth with damping, pressure, and transmission coefficients

8. Conclusions

In the evaluation of a WEC's performance, extracting dimensionless hydrodynamic coefficients is of great importance. Furthermore, investigating the effective parameters on these dimensionless coefficients can contribute to a better understanding of the WEC's performance and help identify conditions in which the WEC achieves its highest level of performance. In this paper, after defining the important dimensionless hydrodynamic coefficients of a model of the OWSC, including the damping, pressure, and transmission coefficients, they were calculated at different water depths. The effect of parameters such as dimensionless draft depth and wave conditions on these coefficients has been discussed. Finally, in order to examine the relationship of each coefficient with the draft depth and wave height, the correlation of dimensionless draft depth and wave height with each coefficient has been calculated and evaluated.

The results show that by analyzing these dimensionless coefficients, a better understanding of the performance of an OWSC can be achieved, and the analysis of the stated coefficients can be used in the design of this WEC, the analysis of these dimensionless coefficients can be utilized in summary, the main results of the study are as follows:

- As the wave height increases, the damping of the WEC decreases; the WEC exhibits higher damping coefficients for lower wave heights compared to higher wave heights.
- Water depth can affect the Cd has a nonlinear effect of the parabolic type and the minimum damping of the OWSC occurs at the optimized water depth, which shows that reducing the damping coefficient leads to better performance of the WEC.
- An increase in the wave height leads to a decrease in the dimensionless pressure coefficient; the reason for this is that the pressure coefficient has an inverse relationship with the wave height and a direct relationship with the pressure difference inside the WEC, and since the effect of the wave height is greater than the effect of the pressure changes in the OWSC, as a result, increasing wave height causes to a change in the pressure coefficient. The pressure coefficient decreases by approximately 40% when the wave height changes from 0.04 m to 0.1 m.
- The increase in dimensionless draft depth has resulted in an increase in the transmission coefficient; an important point to note is that the transfer coefficient at the optimum draft depth primarily has a larger value compared to other draft depths.
- Wave frequency can make damping coefficient rising; because it could be that with the increase in the wave frequency, the WEC loses the opportunity to adapt itself to the wave and consequently it cannot complete a full course, which increases the WEC's damping coefficient
- Wave frequency can decrease the transmission coefficient; but this decrease is more intense at the lowest wave height compared to other wave heights, on the other hand, if the wave height is between 0.06 to 0.08 m, the transmission coefficient has larger values compared to other wave heights.
- The wave height can lead to a non-linear behavior in the transmission coefficient, the transmission coefficient at small wave heights and large wave heights has a small amount while the transmission coefficient in the range of 0.07 to 0.08 m has reached its maximum value, from a structural considerations of view, this can be very important.

9. References

[1] A. J. Henry, "The hydrodynamics of small seabed mounted bottom hinged wave energy conerverters in shallow water," Queen's University Belfast, 2009.

[2] M. H. Jahangir, M. Mazinani, and Z. Ranji, "The Application of Energy Absorbers to Harness Wave Energy in the Caspian Sea: A Feasibility Study," *International Journal Of Coastal, Offshore And Environmental Engineering (ijcoe),* vol. 6, no. 5, pp. 39-50, 2021.

[3] M. Aghanezhad, R. Shafaghat, and R. Alamian, "Experimental Performance Evaluation of a Hydraulic PTO System for Centipede Wave Energy Converter," *International Journal Of Coastal, Offshore And Environmental Engineering (ijcoe),* vol. 5, no. 4, pp. 35-46, 2020.

[4] M. Folley, T. Whittaker, and M. Osterried, "The oscillating wave surge converter," in *ISOPE International Ocean and Polar Engineering Conference*, 2004: ISOPE, pp. ISOPE-I-04-073.

[5] B. Drew, A. R. Plummer, and M. N. Sahinkaya, "A review of wave energy converter technology," ed: Sage Publications Sage UK: London, England, 2009.

[6] A. Babarit, J. Hals, M. J. Muliawan, A. Kurniawan, T. Moan, and J. Krokstad, "Numerical benchmarking study of a selection of wave energy converters," *Renewable energy,* vol. 41, pp. 44-63, 2012.

[7] E. Renzi and F. Dias, "Hydrodynamics of the oscillating wave surge converter in the open ocean," *European Journal of Mechanics-B/Fluids,* vol. 41, pp. 1-10, 2013.

[8] D. Sarkar, E. Renzi, and F. Dias, "Wave power extraction by an oscillating wave surge converter in random seas," in *International*

Conference on Offshore Mechanics and Arctic Engineering, 2013, vol. 55423: American Society of Mechanical Engineers, p. V008T09A008.

[9] Y. Wei, A. Rafiee, B. Elsaesser, and F. Dias, "Numerical simulation of an oscillating wave surge converter," in *International Conference on Offshore Mechanics and Arctic Engineering*, 2013, vol. 55317: American Society of Mechanical Engineers, p. V001T01A012.

[10] E. Renzi, A. Abdolali, G. Bellotti, and F. Dias, "Wave-power absorption from a finite array of oscillating wave surge converters," *Renewable Energy,* vol. 63, pp. 55-68, 2014.

[11] Y.-C. Chang, D.-W. Chen, Y.-C. Chow, S.-Y. Tzang, C.-C. Lin, and J.-H. Chen, "Theoretical analysis and sph simulation for the wave energy captured by a bottom-hinged owsc," *Journal of Marine Science and Technology,* vol. 23, no. 6, p. 9, 2015.

[12] P. Ferrer, D. Causon, L. Qian, C. Mingham, and Z. Ma, "Numerical simulation of wave slamming on a flap type oscillating wave energy device," *Proceedings of the Twentysixth,* 2016.

[13] L. Wilkinson, T. Whittaker, P. R. Thies, S. Day, and D. Ingram, "The power-capture of a nearshore, modular, flap-type wave energy converter in regular waves," *Ocean Engineering,* vol. 137, pp. 394-403, 2017.

[14] X. Jiang, S. Day, and D. Clelland, "Hydrodynamic responses and power efficiency analyses of an oscillating wave surge converter under different simulated PTO strategies," *Ocean Engineering,* vol. 170, pp. 286-297, 2018.

[15] M. Brito *et al.*, "A numerical tool for modelling oscillating wave surge converter with nonlinear mechanical constraints," *Renewable Energy,* vol. 146, pp. 2024-2043, 2020.

[16] M. Brito, R. M. Ferreira, L. Teixeira, M. G. Neves, and R. B. Canelas, "Experimental investigation on the power capture of an oscillating wave surge converter in unidirectional waves," *Renewable Energy,* vol. 151, pp. 975-992, 2020.

[17] Z. Liu, Y. Wang, and X. Hua, "Numerical studies and proposal of design equations on cylindrical oscillating wave surge converters under regular waves using SPH," *Energy Conversion and Management,* vol. 203, p. 112242, 2020.

[18] Z. Liu, Y. Wang, and X. Hua, "Prediction and optimization of oscillating wave surge converter using machine learning techniques," *Energy Conversion and Management,* vol. 210, p. 112677, 2020.

[19] Y. Cheng, G. Li, C. Ji, T. Fan, and G. Zhai, "Fully nonlinear investigations on performance of an OWSC (oscillating wave surge converter) in 3D (three-dimensional) open water," *Energy,* vol. 210, p. 118526, 2020.

[20] Y. Liu, Y.-H. Cho, N. Mizutani, and T. Nakamura, "Study on the resonant behaviors of a bottom-hinged oscillating wave surge converter," *Journal of Marine Science and Engineering,* vol. 10, no. 1, p. 2, 2022.

[21] G. Sadripour, R. Shafaghat, B. Alizadeh Kharkeshi, and S. Sadeqi, "Experimental Study on The Effect of Water Depth and Incident Wave Frequency on The Performance of a OWSC Imposed to Caspian Sea Wave Conditions," *Modares Mechanical Engineering,* vol. 22, no. 9, pp. 603-613, 2022.

[22] G. Sadripour, R. Shafaghat, B. Alizadeh Kharkeshi, R. Tabassom, and A. Mahmoudi, "Installation Depth and Incident Wave Height Effect on Hydrodynamic Performance of a Flap Type Wave Energy Converter: Experimental Analysis," *International Journal of Engineering,* vol. 35, no. 12, pp. 2283-2290, 2022.

[23] R. Alamian, R. Shafaghat, S. S. Hosseini, and A. Zainali, "Wave energy potential along the southern coast of the Caspian Sea," *International journal of marine energy,* vol. 19, pp. 221-234, 2017.

INTERNATIONAL JOURNAL OF
COASTAL, OFFSHORE & ENVIRONMENTAL ENGINEERING
IJCOE Vol.10/No. 2/ Spring 2025 (54-66)

Available online at: www. Ijcoe.org

The Impact of Westward Currents in the Indian Ocean on Precipitation in Western and Southwestern Iran

Ali Sadeghi[1], Farzaneh Jafari Hombari[2], Farshad Pazhoh[3*], Mohammadreza Rozbahany[4]

[1] *Associate Professor, Department of Humanities and Social Sciences, Farhangian University, Tehran, Iran;* a.*sadeghi@cfu.ac.ir*
[2] *PhD in Climatology, Department of Natural Geography, Faculty of Earth Sciences, Shahid Beheshti University, Tehran, Iran; farzaneh.jafari1992@gmail.com*
[3] *PhD in Climatology, Department of Natural Geography, Faculty of Geographical Sciences, Kharazmi University, Tehran, Iran; farshad.pazhooh44@gmail.com*
[4] *Assistant Professor, Department of History, Farhangian University, Tehran, Iran;* Rozbahany12@yahoo.com

ARTICLE INFO

Article History:
Received: 04 Nov 2024
Accepted: 20Aug 2025
Available online ….

Keywords:
Sudanese Low Pressure
Indian Ocean
Trough
Jet Stream
Widespread Rainfall

ABSTRACT

In this study, to identify the source of moisture for the widespread and heavy rainfall that occurred on 21 and 22 January 2007 in the western and southwestern regions of the country. To achieve this, we conducted a synoptic and thermodynamic analysis of the rainfall. Daily precipitation data from 45 synoptic stations across 7 provinces were obtained from the Iranian Meteorological Organization and analyzed. First, we identified the rainfall through data from ground stations. Then, using upper atmosphere data and relevant maps, we analyzed the widespread and heavy rainfall in the west and southwest of the country. The results show that on the day of the onset of precipitation, the Sudanese and Mediterranean low-pressure troughs merged on the eastern edge of the Mediterranean, and on the day of the peak of precipitation, the Sudanese low-pressure system independently caused the rainfall of this period. The study of moisture flow maps showed that the Indian ocean and Red, Oman and Persian Gulf Seas played a major role in strengthening and providing moisture to the Sudanese low-pressure system during the occurrence of precipitation. At high levels, on the day of the onset of precipitation, the establishment of blocking in the west of the study area and the displacement of the trough associated with it over the study area and the expansion of the trough axis resulting from it to southern Arabia and the location of the western half of Iran in the east and in front of the trough and its association with low surface pressure have advanced simultaneously. The establishment of the subtropical jet stream on the front of the trough and high divergence played a major role in strengthening the Sudanese low-pressure system, sucking moisture from southern water resources, and as a result, widespread rainfall in the west and southwest of the country.

1. Introduction

Synoptic climatology is a science that studies the relationship between atmospheric circulations and the surface environment of a region (Masoudian, 2006, 1). Synoptic and thermodynamic analysis of atmospheric circulation patterns, in identifying factors affecting the occurrence and behavior of precipitation, provides the possibility of planning based on it. This kind of attention to precipitation is of particular importance, especially in various areas of a water-scarce land such as Iran, whose water resources rely on precipitation and are accompanied by an increasing demand from a growing population (Asakereh and Razmi, 2011, 138). Since atmospheric instability and precipitation occurrence in southwestern Iran are generally affected by Sudanic systems, therefore, studying the dynamics of the formation, evolution and decline of this system, predicting and knowing the status of precipitation and planning for the exploitation of these precipitations as reserves for the reservoirs of the region's dams, can be effective and efficient in the management and planning of water resources. (Mohammadi et al., 2012, 8). Numerous studies have been conducted in Iran and around the world with different approaches and goals regarding synoptic and thermodynamic analysis of heavy precipitation, which shows the importance of studies and their applications. Among them, the following can be mentioned.

(Littman, 2000, 170) classified the pressure and geopotential height data at the 500 hectopascal (hPa) level using cluster analysis and examined the relationship of the resulting weather types with Mediterranean precipitation. (Kahn et al., 2004, 881) In "Interpretation and study of changes in hourly heavy precipitation in Tokyo from 1980 to 1999", they concluded that heavy precipitation occurred in the 1940s and 1990s. (Siebert et al., 2005, 16) studied the regional and synoptic patterns of heavy precipitation in Australia and defined seven synoptic patterns for heavy precipitation in Australia using the path ranking method using daily precipitation from 31 climate stations during the years (1993 to 1997). (Mahras et al., 2004, 4) studied the circulation patterns of 500 hPa in Greece. In his research, he identified six anticyclonic patterns, eight cyclonic patterns, two mixed cyclonic and anticyclonic patterns, and four special weather patterns. (McGarrick et al., 1998, 116) The term plume has been used to mean the explosion of tropical moisture from the tropical part of equatorial Africa and the Gulf of Guinea towards the Middle East and southern Iran, which is a kind of attention to the interaction of the tropical and extratropical regions; that is, the location of the mid-latitude trough axis at the exit of the subtropical jet stream causes clouds from the tropical region of Africa to the Middle East and especially southwest Iran, causing heavy and flooding rainfall. (Keith Busher, 1994, 77) has mentioned something similar for the subtropical region of North America. The transfer of clouds from the equatorial part of Africa and the Gulf of Guinea to the Middle East and southwestern Iran and the occurrence of heavy rainfall due to the location and shape or type of curvature of the subtropical jet stream axis and the unification of the mid-latitude trough axis at the outlet of the subtropical jet stream in the northern Red Sea has been demonstrated by examining satellite images of several large storms and observing a very high density of clouds over an area of several thousand kilometers from the subtropical convergence belt (equatorial Africa) towards the Caspian Sea (Dayan and Abramsky, 1983, 63).

(Sabziparvar, 1991, 9) has studied the synoptic of flood-causing systems in southwestern Iran. He considers the main factor of heavy and flood-causing rainfall in southwestern Iran to be the presence of a deep trough at high level (so that the trough axis extends southward to the south of the Red Sea). According to their research, the dynamic Mediterranean low pressure, while moving east and southeastward, through the injection of cold air into the low pressure of the Sudan region, causes this low pressure to become dynamic and a combined system called the Mediterranean-Sudanese system is formed, which is an example of the interaction of a polar air mass with a tropical air mass and brings relatively significant rainfall in Iran. (Lashkeri, 2003) has studied the Sudanese low pressure and its role in rainfall in the south and southwest of Iran. He introduces the Sudanese low pressure system as one of the elements of the general atmospheric circulation in North Africa, which is formed over western Ethiopia and Sudan most of the year, and four general patterns resulting from the arrangement of the Siberian systems, the North African anticyclone, and the Arabian Peninsula, the North African trough, and the Sudanese low pressure in the lower and middle levels of the atmosphere, lead to the occurrence of heavy rainfall in the south and southwest of Iran. (Mafidi, 2004, 92) introduced a synoptic study of flood-causing rainfall in the Middle East, which appeared from the convergence zone on the western side of the Ethiopian plateau and then moved towards Iran or the eastern Mediterranean under the influence of the topographic factors of the Red Sea and the thermodynamic and dynamic conditions governing the atmosphere of the surrounding areas. (Alijani, 2002, 131) used the calculation of vorticity to identify the rain-causing masses of Tehran. He stated that the effect of the 500 hpa level is more important than other levels and that cyclone types produce heavier rainfall.

(Mafidi and Zarrin, 2005, 135) studied the effect of Sudanese low-pressure systems on the occurrence of heavy and flood-causing rainfall in Iran from a synoptic perspective and stated that the main role in flood-causing rainfall is attributed to the influence of the polar vortex at the level of 500 hPa, which acts as the main source of turbulence for the emergence of anomalous circulation patterns and strengthening of the Hadley cell or subtropical jet over the Mediterranean and North Africa. (Masoudian, 2005, 163) analyzed the Karun flood rainfall by analyzing the mid-level circulation patterns and showed the role of Mediterranean thoughts in causing such rainfall. (Omidvar, 2007, 97) studied and analyzed the synoptic and thermodynamic conditions of rainfall occurrence in the Shirkuh region and concluded that the rainfall in this region is caused by three synoptic systems: 1- The establishment of Sudanese low pressure over the Arabian Peninsula; 2- Combined Sudanese and Mediterranean systems; 3- Mediterranean systems. Akbari et al, 2016: 591 In examining the role of the Blocking system in the January 2008 precipitation event in southeastern Iran, they showed that during the precipitation, the penetration of the Sudanese low pressure at the ground surface and the Blocking system in the middle atmosphere caused the dynamics of low pressure and the occurrence of torrential rainfall in the region. (Ghavidel & Jafari, 2020: 17) In analyzing the extremely heavy rainfall on April 1, 2019 in western Iran, they concluded that at the ground surface, the presence of low pressure in northern Arabia and at mid-levels of the troposphere, the establishment of a cut-off low blocking in western Asia provided the conditions for the spread of unstable flows from the Red Sea and Mediterranean to the western half of Iran. (Ghassabi etal, 2022: 17) In examining the effects of daily circulation patterns of the troposphere on dry and wet events in Iran, they found that the expansion of south and southwest currents from the Red Sea creates conditions for the expansion of low-pressure centers from the south of the Red Sea to southern Turkey and the western parts of Iran, resulting in most precipitation occurring in the western half of the Zagros Mountains. Zakizadeh et al. (2018: 31) also considered the establishment of a 65 m/s jet stream at a level of 300 hpa in the southern half of Iran, along with the formation of a cold trough over the Caspian Sea, to be the reason for the occurrence of heavy and widespread precipitation in Iran. Omidvar et al. (2018: 35) studied the heavy rainfall of December 24, 2014 in Kohgiluyeh and Boyer Ahmad provinces and found that the formation of a blocking phenomenon over the Mediterranean Sea and its deep thought over Iraq, resulting in the fall of cold air over the region and the transfer of warm southern air, caused heavy rainfall on this day over the studied region. According to Pazhoh and Darand (2024), the concentration of precipitation in Iran has increased in recent years, and the concentration of precipitation in the western and southwestern regions of the country was due to a decrease in the frequency of rainy days and an increase in the intensity of heavy rainfall. The purpose of this research is to conduct a synoptic and thermodynamic analysis of the causes of widespread and heavy rainfall in the western half of the country in relation to low-pressure systems and to analyze the moisture role of water resources adjacent to Iran, the results of which will help to further understand the rain-generating systems in these regions.

2. Data and Methods

This study utilized two sets of data to analyze the widespread and heavy rainfall that occurred on 21 and 22 January 2007 in western and southwestern Iran. These data sets include ground station data and upper atmosphere data. The ground station data consist of daily precipitation measurements for 21 and 22 January 2007, obtained from the Machine Services Department of the Iran Meteorological Organization. The upper atmosphere data comprise reanalyzed data for geopotential height, sea level pressure, zonal wind, meridional wind, and omega, sourced from the National Center for Environmental Prediction in Colorado. The jet stream map was created at the 250 and 300 hPa levels, while additional maps were produced and analyzed at the 1000, 850, 700, and 500 hPa levels. Figure 1 illustrates the distribution of stations in the study area. Furthermore, the total 24-hour rainfall on 21 and 22 January 2007 for more than 45 stations located in the western and southwestern regions of the country is presented in Table 2. The rainfall began in the southwest on 21 January and peaked on 22 January, with significant amounts recorded at stations such as Kohrang (55.8 mm) in the southwest, Doroud (50 mm), and Azna (35 mm) in the west of the region. Table 1 details the geographical locations of the stations in the studied area.

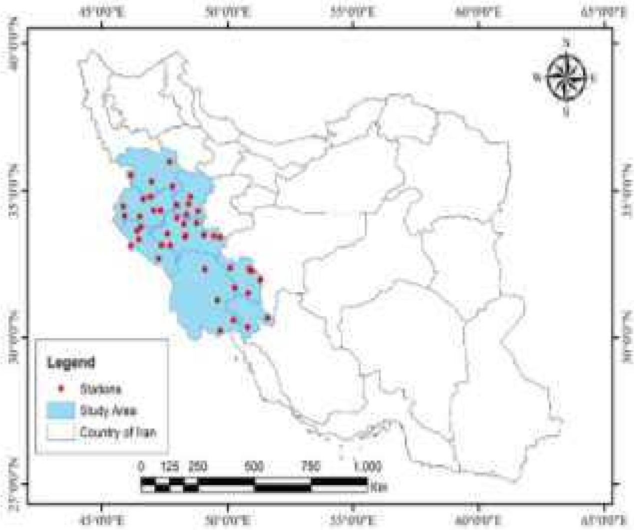

Figure 1. Study area and selected stations

3. Results and Discussion

Table 2 shows the 24-hour rainfall at selected stations, with the peak rainfall occurring on January 22, 2007, and the highest rainfall was recorded at Koohrang station with 55.8 mm due to the influence of the mountainous factor, followed by Doroud and Yasuj stations with 50 and 33 mm.

Table 1. Geographical location of stations in the study area

Stations	Height	lon		lat		Stations	Height	lon		lat	
Bijar	1883	47	37	35	53	**Azna**	1871.9	49	25	33	27
Qorveh	1906	47	48	35	10	**Ashtar**	1567.2	48	15	33	49
Marivan	1286.8	46	12	35	31	**Badrabad**	1154.8	48	16	33	26
Sanandaj	1373.4	47	0	35	20	**Boroujerd**	1629	48	45	33	55
Kamyaran	1404	46	56	34	48	**Boroujen**	2197	51	18	31	57
Hamedan	1741.5	48	32	34	52	**Yasuj**	1831.5	51	41	30	50
Malayer	1777.8	48	51	34	15	**Dogonbadan**	699.5	50	46	30	26
Tuysarkan	1783.2	48	26	34	33	**Lordegan**	1580	50	49	31	31
Nahavand	1680.9	48	25	34	9	**Farkhshahr**	2065	50	56	32	18
Ravansar	1379.7	46	39	34	43	**Kuhrang**	2285	50	7	32	56
Sarpol	545	45	52	34	27	**Shahrkurd**	2048.9	50	51	32	17
Kermansha	1318.6	47	9	34	21	**Dhadiz**	1457	50	16	31	43
Kangavar	1468	47	59	3	30	**Lali**	365	49	6	32	20
Islamabad	1348.8	46	28	34	7	**Behbahan**	313	50	14	30	36
Gilan Gharb	816	45	56	34	8	**Hindijan**	3	49	44	30	17
Sararud	1361.7	47	18	34	20	**Ramhormoz**	150.5	49	36	31	16
Dorud	1522.2	49	0	33	31	**Dareshahr**	670	47	24	33	8
Aligudarz	2022	49	42	33	24	**Dehloran**	232	47	16	32	41
Khorramabad	1147.8	48	17	33	26	**Ilam**	1337	46	26	33	38
Kohdasht	1197.8	47	39	33	31	**Lomar**	850	46	50	33	34
Noorabad	1859.1	48	0	34	3	**Mehran**	150	46	11	33	7
Poldukhtar	713.5	47	43	33	9	**Sarabeleh**	1045	46	34	33	47

Table 2. Total 24-hour precipitation of the studied stations

row	Station name	Total 24-hour p in mm		row	Station name	Total 24-hour p in mm		row	Station name	Total 24-hour p in mm	
		21 Jan	22 Jan			21 Jan	22 Jan			21 Jan	22 Jan
1	**Borujen**	3	13	**17**	**Doroud**	0	50	**33**	**Sarabeleh**	0.8	2
2	**Yasuj**	7	33	**18**	**Amanabad**	0	24	**34**	**Badrabad**	5.3	21.4
3	**Dogonbadan**	4	20	**19**	**Khoramabad**	5.5	24.4	**35**	**Borojerd**	4	28
4	**Lordegan**	5	53	**20**	**Kuhdasht**	9	23	**36**	**Nahavand**	3.5	19.3
5	**Farkhshahr**	0	13	**21**	**Noorabad**	2	19	**37**	**Kamiaran**	0	3
6	**Kuhrang**	6	55.8	**22**	**Poldokhtar**	12.5	27	**38**	**Marivan**	1	0.2
7	**Shahrkurd**	4	10.4	**23**	**Hamedan**	3	6.2	**39**	**Sanandaj**	1	0.4
8	**Dhadiz**	0	25	**24**	**Malayer**	5	10.4	**40**	**Ravansar**	2	0
9	**Lali**	1	26	**25**	**Twiserkan**	1.1	5.1	**41**	**Sarpol**	6	0.4
10	**Behbahan**	2	10	**26**	**Aligudarz**	1	22	**42**	**Kermansh**	2.9	7
11	**Hindijan**	0	8	**27**	**Azna**	0	35	**43**	**Kangavar**	7	11.4
12	**Ramhormoz**	2	5.2	**28**	**Dareshahr**	13	23	**44**	**Islamabad**	1.2	11.6
13	**Bijar**	0	5	**29**	**Dehloran**	11	8	**45**	**Gilangharb**	3.1	10
14	**Qorveh**	0.7	1.5	**30**	**Ilam**	3.3	4.8				
15	**Sararud**	0.2	9.1	**31**	**Lomar**	5.5	6				
16	**Aleshtar**	0	16	**32**	**Mehran**	7	15				

3.1. Synoptic and dynamic conditions of the first day of precipitation on 21 January 2007

As you can see in the sea level pressure map in Figure 2, an inverted low pressure with a pressure of 1005 hpa is closed on the eastern edge of the Mediterranean, which has formed a Sudanese-Mediterranean integrated system that covers from Sudan to northwest Iran, and western Iran is located in the eastern half of this integrated system. And the center of this low pressure coincides with the upper atmosphere trough.

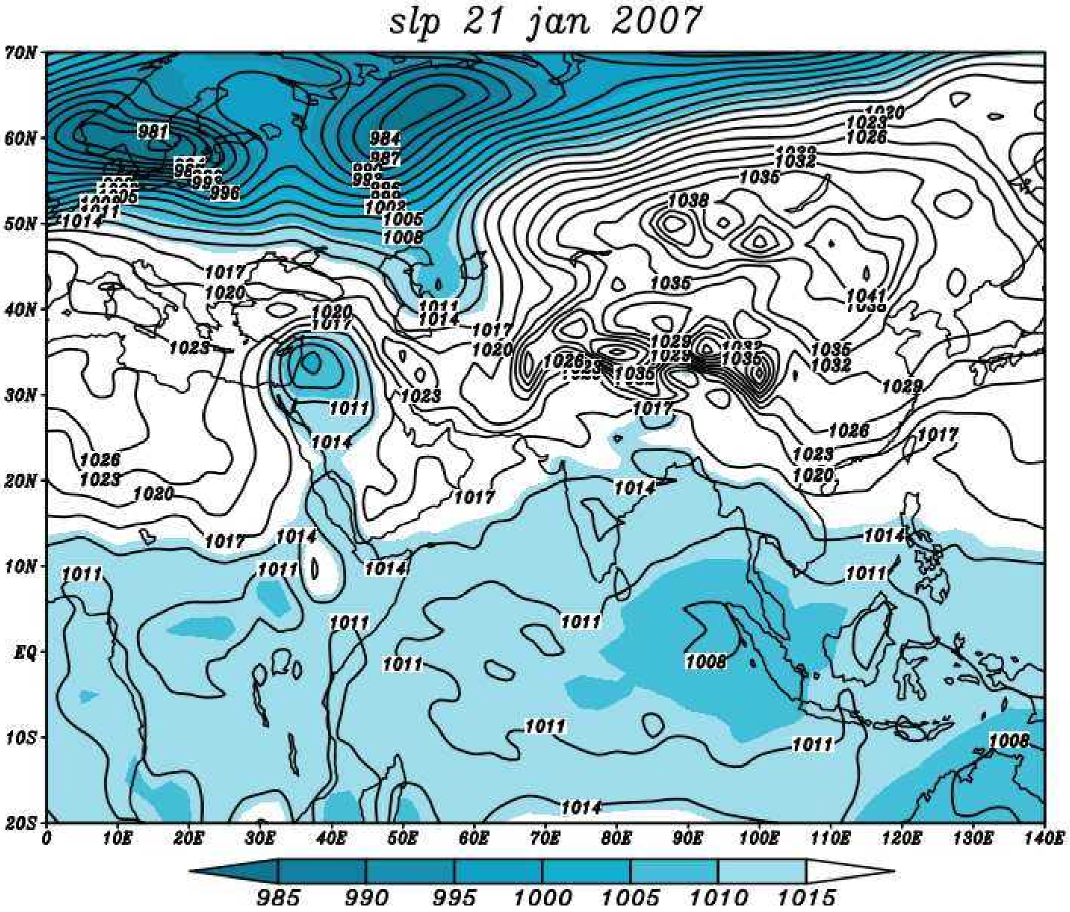

Figure 2. Sea level pressure map on January 21, 2007, one day before the peak of precipitation

In the 850 hPa height map in Figure 3, it is observed that a trough with 1395 geopotential meters is closed on the eastern edge of the Mediterranean Sea, which has a south-north curvature from the south of the Red Sea to the eastern edge of the Black Sea. Western Iran is located on the eastern edge of the trough and in front of it. At the 700 hPa level in Figure 4, the trough located on the eastern edge of the Mediterranean, which is a Cutoff Low, has deepened compared to the 850 hPa level, and the southern limit of this strong cyclone has extended to Sudan, where the study area (western Iran) is located in front of the trough that advects warm and humid air. The study area is currently under the influence of the ridge resulting from the high over Arabia, which plays the role of feeding moisture into the Sudanese system. In the omega map of the 1000 hPa level in Figure 5, it is observed that a field with a strong positive omega is closed over the western half of Iran with 0.2 Pascal/Second (P/S), which indicates air convergence at this level. At the 850 hPa level in Figure 6, the presence of a closed negative omega field with -0.25 P/S over western Iraq and the location of western Iran to the east of this negative omega field indicates severe divergence and increased instabilities on the first day of precipitation. It is observed that over the Mediterranean, the positive omega indicates convergence over this sea. However, over Sudan, along the negative omega field over western Iran, it is completely negative omega, which indicates severe moisture divergence from Sudan to western Iran. At the level of 700 hPa, Figure 7, the negative omega field became stronger and closed at -0.4 P/S over western Iraq, which exactly coincided with the center of low pressure on the earth's surface, and the south-north direction of the negative omega coincided with the location of western Iran in front of the trough.

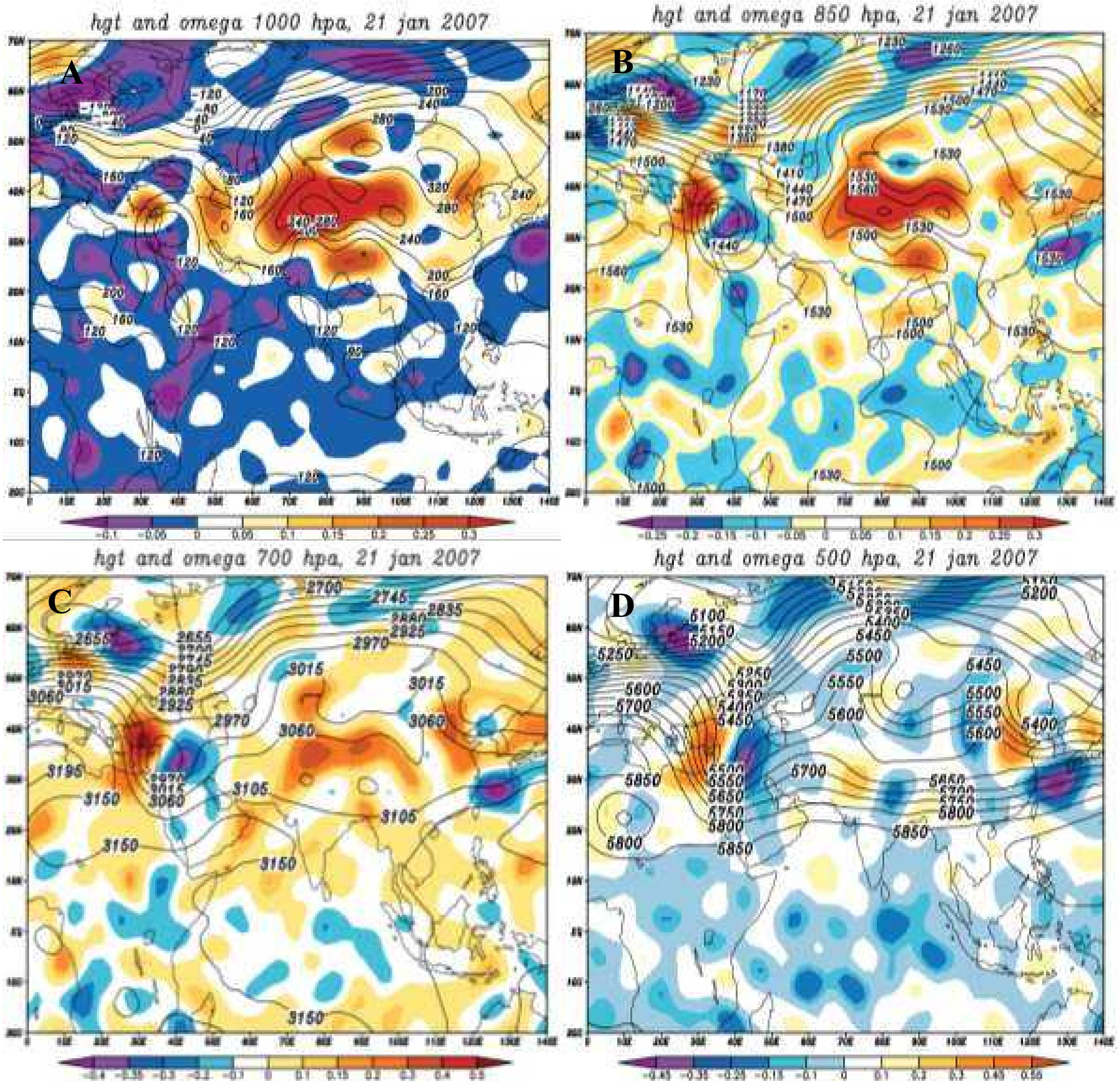

Figure 3. Composite maps of geopotential height (line) and omega (color) on January 21, 2007, one day before the peak of precipitation, at levels A: 1000, B: 850, C: 700, and D: 500 hPa, respectively.

In the 1000 hPa humidity map in Figure 4-A, it is observed that the highest specific humidity with more than 14 g/kg is closed over the Red Sea, which is in the direction of these currents from Sudan, but it reaches less than 12 g/kg over the Mediterranean Sea. It is observed that at the level of 850 hPa in Figure 4-B, the maximum specific humidity is still present over the Red Sea and low latitudes, and the expansion of this specific humidity is located exactly in front of the trough, which is approaching from low latitudes over the western region of Iran. In Figure 4-C, the path of the maximum specific humidity coincides with the east of the trough axis, extending southwest-northeast and passing over the Red Sea, Saudi Arabia and the Persian Gulf, and a second weak moisture core is also in the east of the Mediterranean Sea, which is seen separately in the center of the cyclone circulation. At the 500 hPa level, Figure 4-d shows that the amount and flow of moisture have decreased, but the maximum source of moisture is seen at low latitudes and in southern Arabia and the Gulf of Aden.

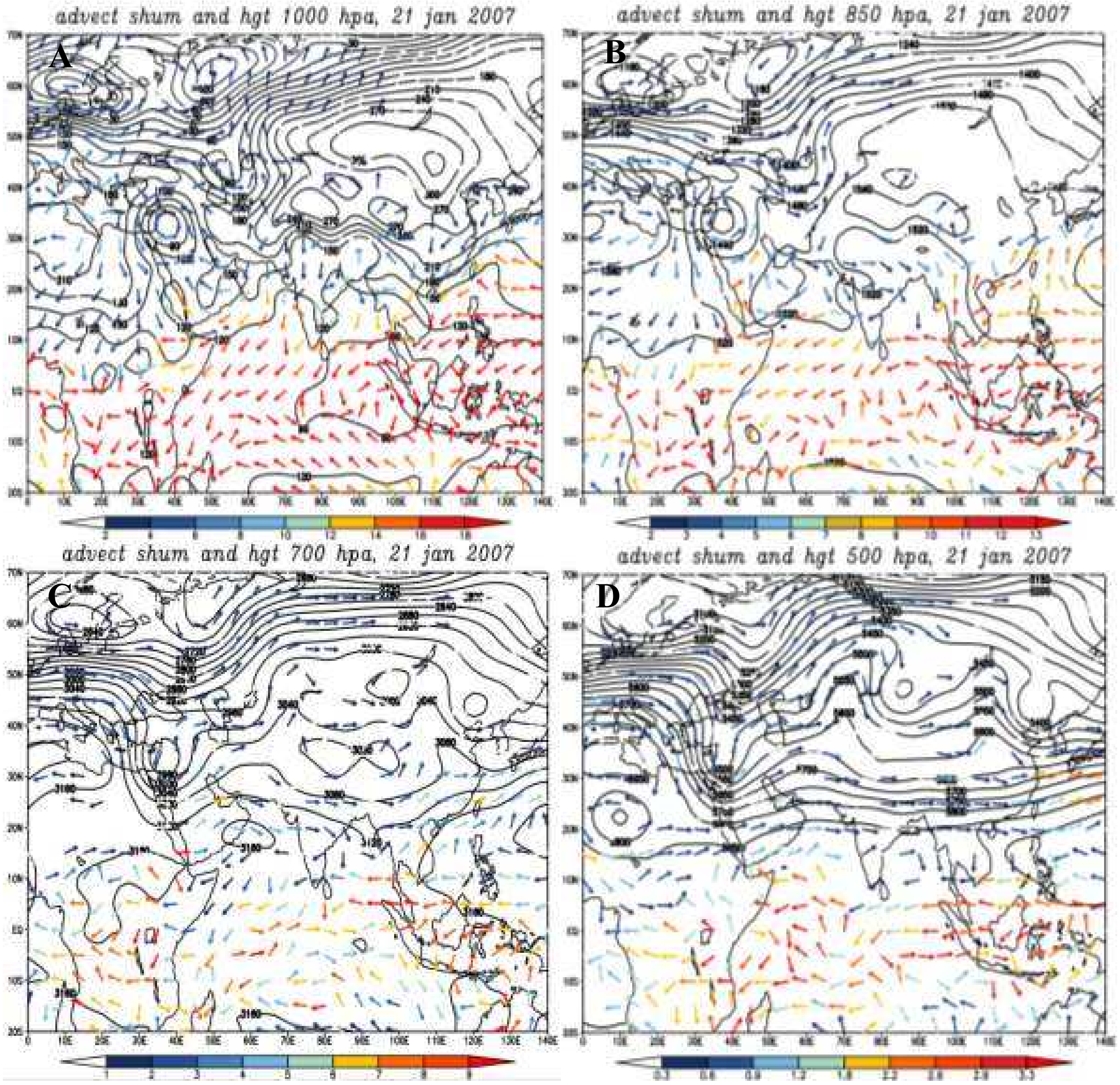

Figure 4. Composite maps of moisture advection (colored arrows) and geopotential height (line) on January 21, 2007, one day before the peak of precipitation, at levels A: 1000, B: 850, 700, and 500 hPa**, respectively**

Figure 5-A shows the 250 hPa level of the jet stream on January 21, 2007, the day before the peak of the precipitation system activity. It can be seen that the core of the jet stream is located in the west-east direction with a speed of more than 60 m/s in southern Iran, Saudi Arabia and the Sea of Oman, with the study area located to the north of the core of the jet stream. In the 300 hPa level of the jet stream in Figure 5-B, while the speed in the core decreases, it maintains its same position at the 250 hPa level, which covers Iran by passing through the northeastern lands of Africa and Saudi Arabia, and at both levels of 250 and 300 hPa, the curvature of the jet stream extends towards the study area and coincides with the path of maximum moisture advection at the east of the trough axis.

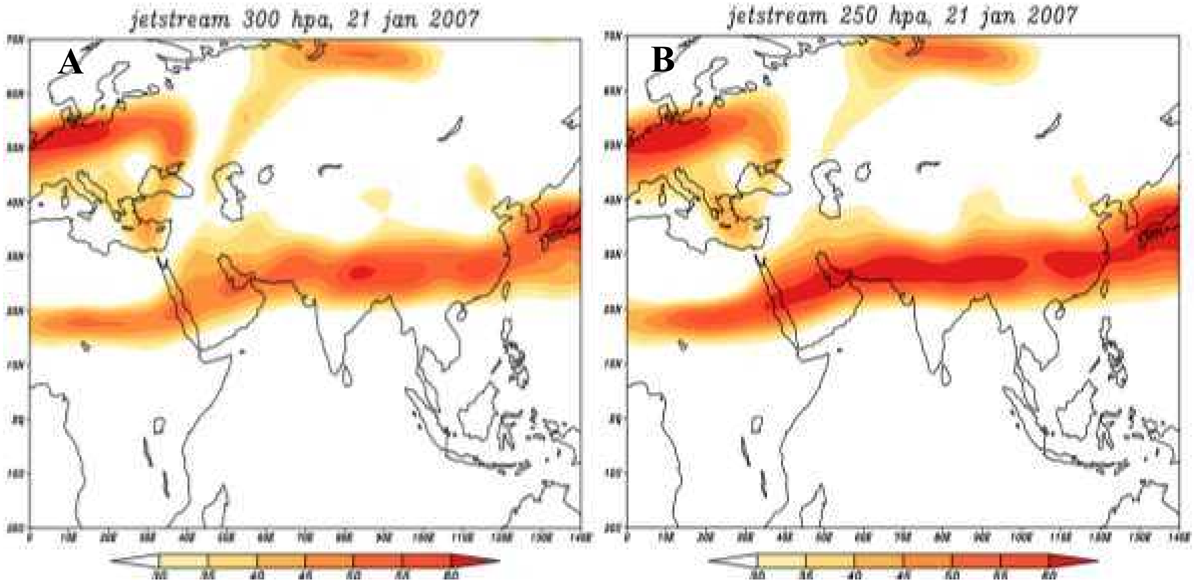

Figure 5. Jet stream maps on January 21, 2007, one day before the peak precipitation at levels A: 300, B: 250 hPa, respectively.

3.2. Synoptic and dynamic conditions on the day of the peak activity of the precipitation system, January 22, 2007

In the sea level pressure map in Figure 6, it can be seen that the low pressure center closed at 1014 in the center of Saudi Arabia and with its south-north extension stretched from southern Saudi Arabia to northwestern Iran. Compared to the closed low pressure the previous day, with an eastward movement from the eastern edge of the Mediterranean to western Iran on the day of the peak of the precipitation, the low pressure center was completely located over the study area. Behind the low pressure system, the infiltration of cold high pressure by passing over the Mediterranean Sea and the advection of warm air from the Arabian Sea in front of the low pressure system increased its intensity.

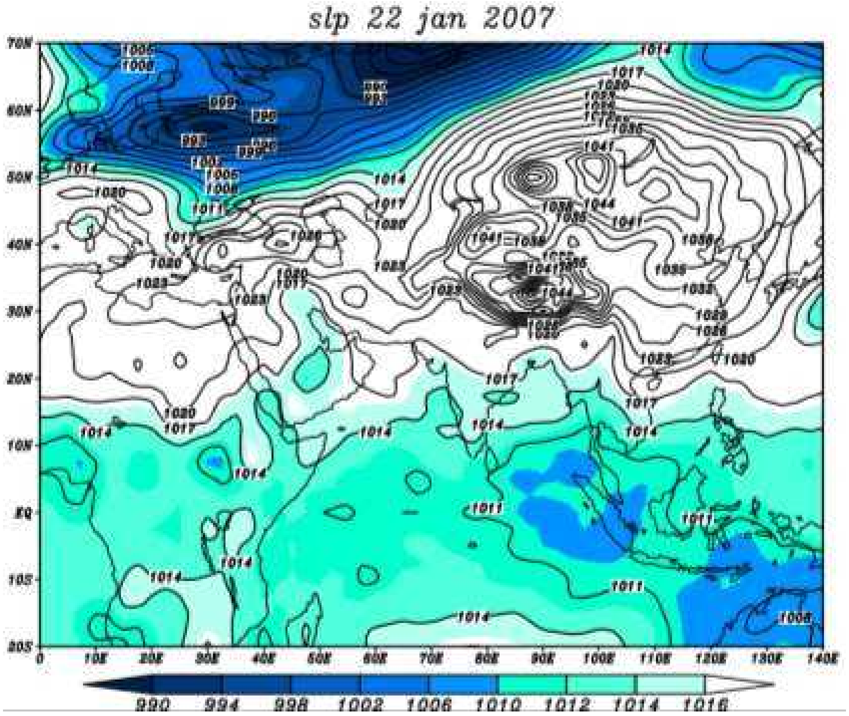

Figure 6. Sea level pressure map on January 22, 2007, the day of peak precipitation (color range: low pressure)

At the level of 850 hPa, Figure 7-b shows the location of the closed cyclone center with 1470 geopotential meters in western Iran, which covers most of Iran and extends from Sudan towards the region with its southwest-northeast curvature, and while deepening and changing the direction of the trough front to southwest-northeast, it has led to an increase in the advection of warm and humid air over the region. At the level of 700 hPa, Figure 7-c, the cyclone center with 3000 geopotential meters has moved eastward, but it has become wider and deeper than the previous day, and its southern tongue has expanded towards low latitudes. With the cyclone center moving eastward, the trough has also moved eastward, and as a result, western Iran has been affected by the instability process of the trough front. And the high over Arabia, while becoming wider, plays the role of feeding more moisture into the Sudanese system. The formation of an omega-shaped blocking in the injection of cold air behind the trough has also led to further strengthening of the 700 hPa trough. It is observed that with the deepening of the trough and the increase in meridional curvature and the eastward movement towards Iran, the warm and humid air has well diverged the southern water resources. In the 500 hPa level map (Figure 7-d), the depth of the trough is greater and the cutoff-low is located over West Asia. In the combined omega-geopotential height map of the 1000 hPa level, Figure 7-a, it is observed that the western half of Iran is dominated by the positive omega field, whose center is closed in northwest Iran with 0.25 P/S, which indicates air convergence in the lower atmosphere. At the 850 hPa level, the center of the negative omega field is closed over the Persian Gulf with -0.2 P/S, which extends to western Iran and indicates the strengthening of air instability and divergence at this level. At the level of 700 hPa, the intensity of the negative omega increased, reaching -0.3 P/S at its center, extending from Sudan to northern Iran with a southwest-northeast curvature, which strengthened the instabilities and showed a peak of precipitation on January 22, 2007.

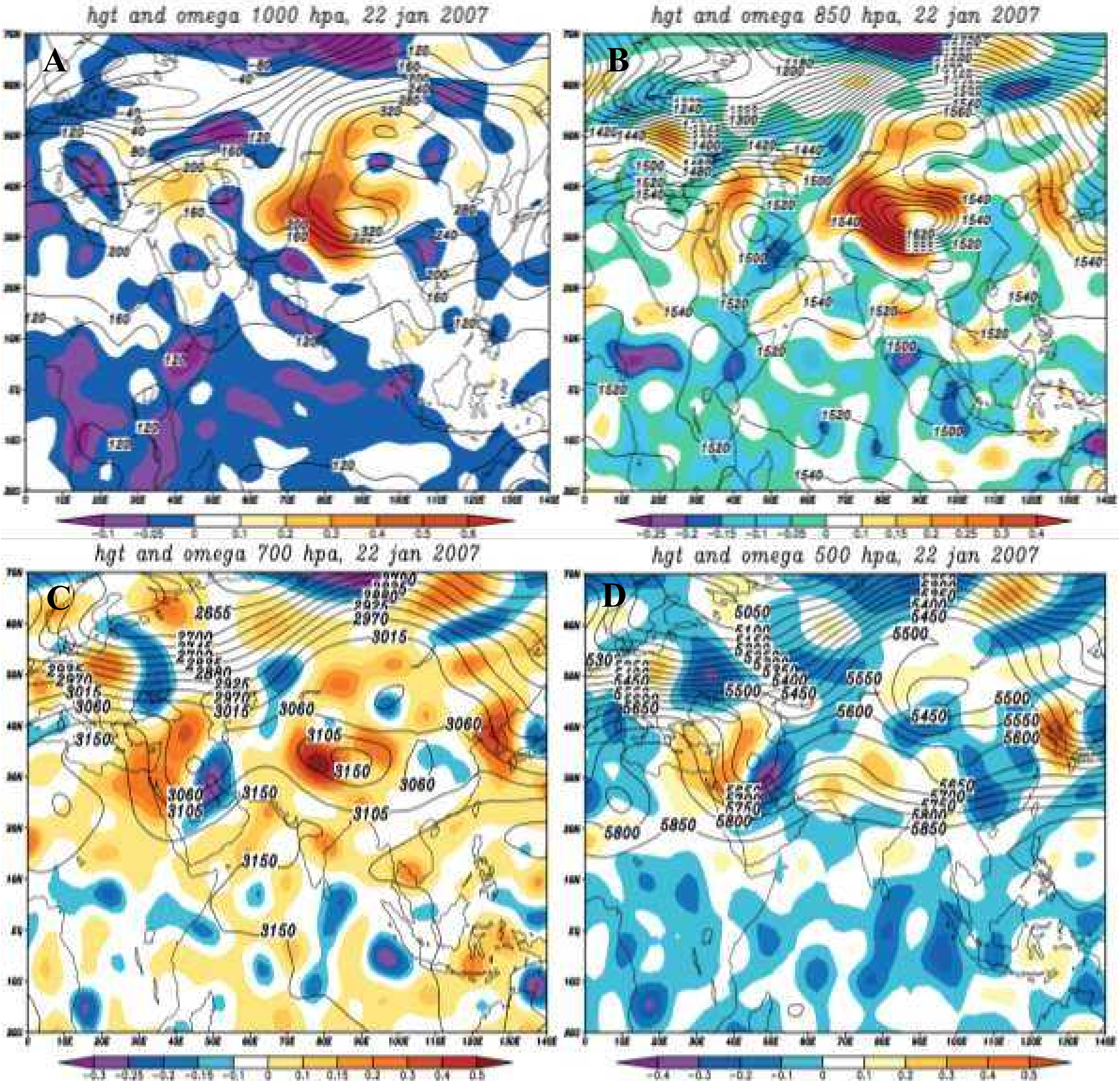

Figure 7. Composite maps of geopotential height (line) and omega (color) on January 22, 2007, peak precipitation at levels A: 1000, B: 850, C: 700 and D: 500 hPa, respectively

In the moisture advection map at the 1000 hPa level, Figure 8-A, a specific moisture core of more than 10 grams per kilogram is observed over southern Arabia, with a counterclockwise wind and a southwest-northeast current direction, which is aligned with the trough map located over the western half of Iran in front of the trough over the study area. At the 850 hPa level, Figure 8-B, the highest specific moisture core is over Sudan and southern Arabia, and the current direction is also in the same direction as the 1000 hPa level and coincides with the trough front, which has caused the advection of warm and humid southern air in the occurrence of instabilities and precipitation in the western half of Iran. The currents over the Indian Ocean are completely westward, and from there, they move towards higher latitudes, passing through the Arabian Sea and advection into the study area. It is observed that the cyclonic circulation, aligned with the Sudanese low-pressure track, with a southwest-northeast direction and passing over Saudi Arabia and the Persian Gulf, has provided precipitation moisture on the peak day. In Figures 8c-d, the levels of 700 and 500 hPa also have the maximum specific humidity in the south of the Red Sea and Arabia, but compared to the lower levels of the atmosphere, the path of moisture entry has shifted to the east and has advected from the southeast of Arabia and the west of the Arabian Sea, passing over the Persian Gulf and with a deep cyclonic circulation coinciding with the east of the trough axis, advection over the western and southwestern regions of Iran. It is observed that at the levels of 700 and 500 hPa, the strengthening of the anticyclonic circulation over the Arabian Sea plays a major role in sending moisture into the Sudanese low-pressure system and in front of the trough.

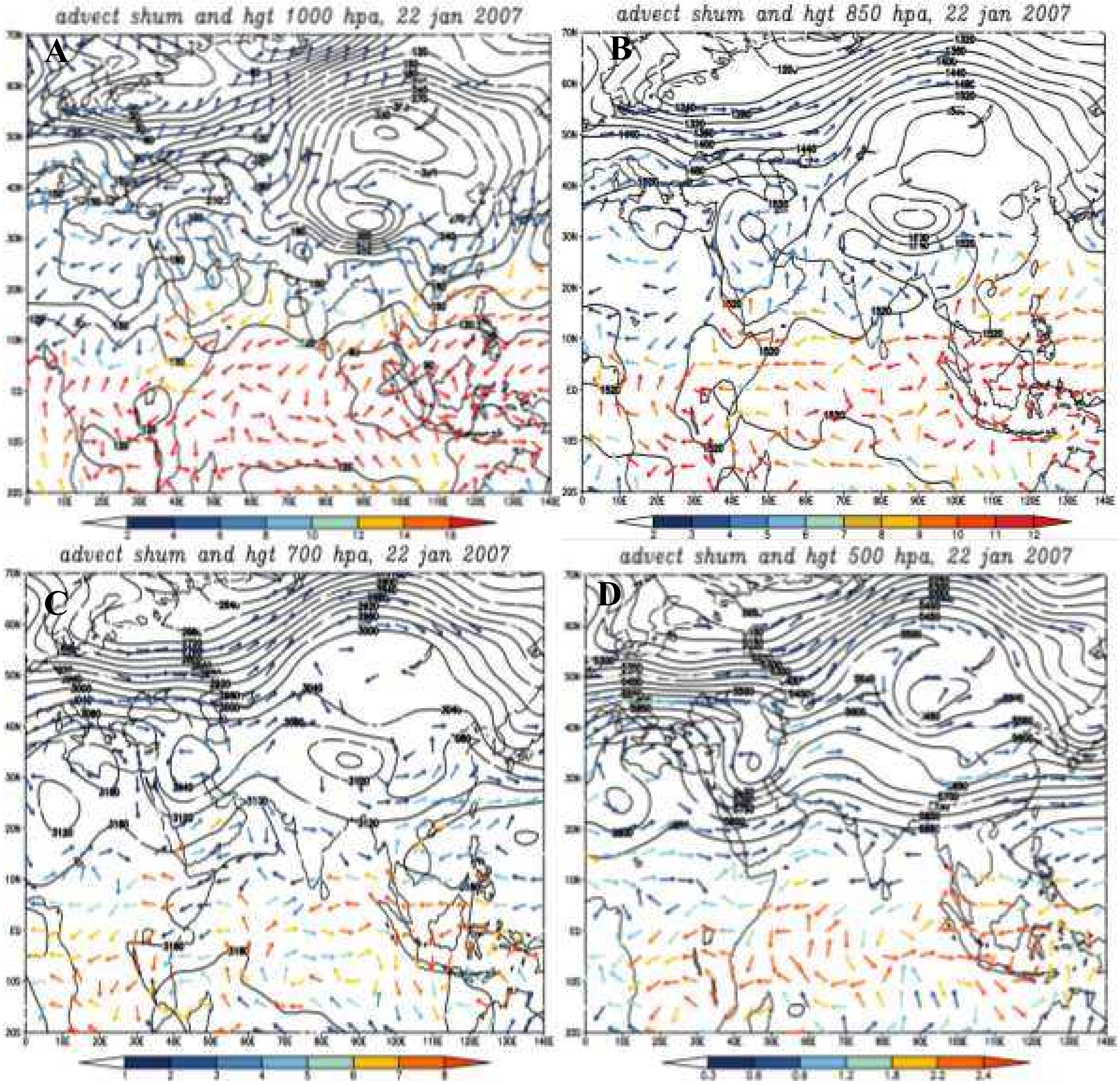

Figure 8. Composite maps of Moisture advection (colored arrows) and geopotential height (line) on January 22, 2007. Peak precipitation , at levels A: 1000, B: 850, 700, and 500 hPa, respectively.

Figure 9 shows the total specific humidity map of 1000 to 500 hPa levels during rainy days in western and southwestern Iran. Based on this map, it is observed that the cores of maximum specific humidity in East Africa and the low pressure area of Sudan with an intensity of more than 80 g/kg have been formed, which indicates the effect of east-west circulations from water resources towards land, from where, due to the penetration of the mid-level atmospheric trough to these areas, conditions have been prepared for the advection of specific humidity with a southwest-northeast extension towards the study area. Here, by eliminating values less than 35 g/kg, the specific humidity path has been more clearly identified.

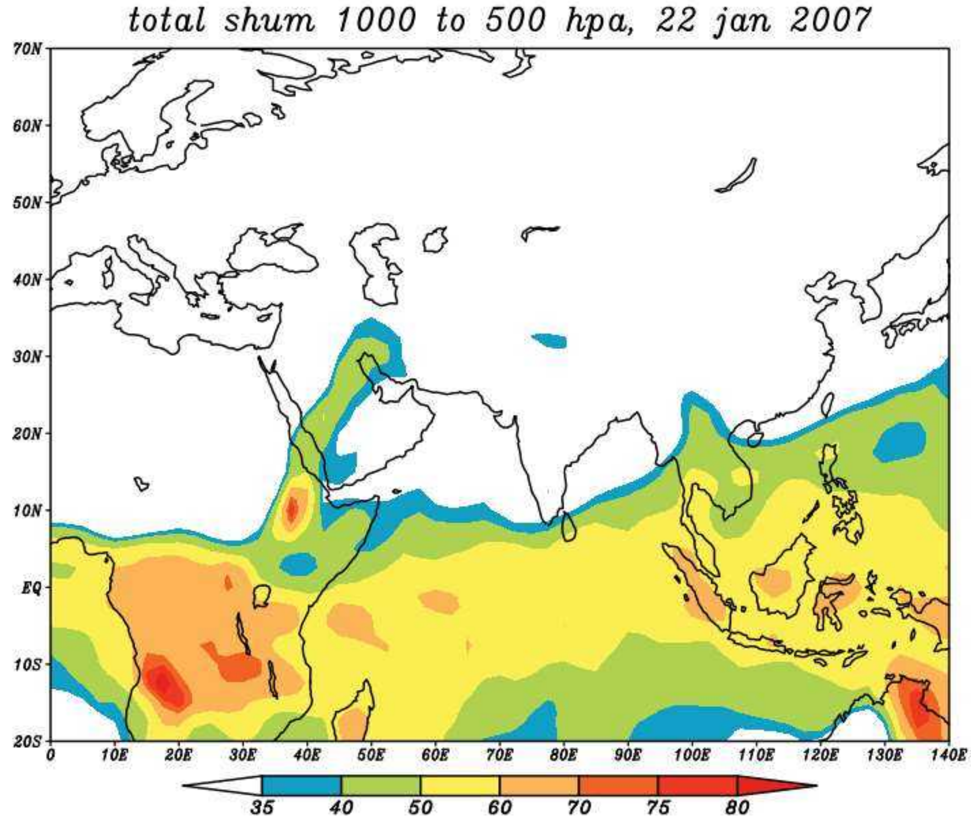

Figure 9. Map of total specific humidity for the rainy days of January 21 and 22, 2007

Figure 10 shows the jet stream at levels of 250 and 300 hPa on January 22, 2007. On the day of the peak rainfall, the subtropical jet stream, entering from the northeast of Africa and located on the left side of the jet stream outlet over the western half of Iran, shows the highest divergence. The central core speed is very high at levels of 250 and 300 hPa, 60 and 55 meters per second, respectively. By passing over the southern sources and lands in a southwest-northeast direction, and the jet stream coincides with the upper divergence and east of the trough axis, and coincides with the specific moisture path and vorticity maps, it has provided cyclone-forming conditions in the region and led to an intensification of instabilities.

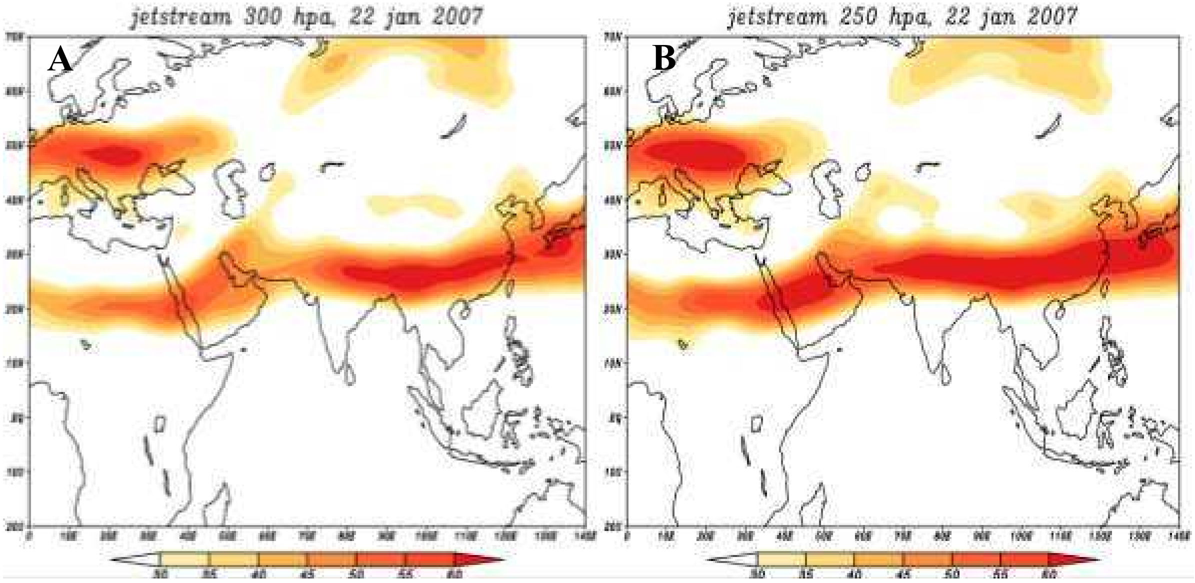

Figure 10. jet stream maps on January 22, 2007, peak rainfall, respectively at levels A: 300, B: 250 hPa

4. Conclusion

The occurrence of widespread and heavy rainfall in the west and southwest is a prominent characteristic of these regions. Since the moisture factor is more important than the ascent factor for creating widespread and heavy rainfall, it seems necessary to identify the sources and origin of precipitation moisture. In this study, the synoptic and dynamic conditions of the heavy and widespread rainfall on 1 and 2 Bahman 1385, corresponding to 21 and 22 January 2007, and its relationship with the moisture sources adjacent to Iran and the Sudanese and Mediterranean low-pressure systems were investigated. In the sea level pressure maps on the first day of precipitation, the Sudanese and Mediterranean low pressure systems merged on the eastern edge of the Mediterranean and on the day of peak precipitation, the center of the Sudanese low pressure system was independently closed over western Iran and high pressure centers were located in northwest Iran and over Turkey with 1032 and 1028 hPa, whose northwest-southeast lobes introduced cold air behind the Sudanese low pressure system, increasing the thermal gradient and strengthening the Sudanese system on the day of widespread precipitation in west and southwest Iran. Examination of the omega and geopotantial height maps also indicates divergence and severe cyclonic rotation in the ascend of moist air on the day of precipitation. With the deepening of the trough over Arabia and Iraq to the Red Sea region and its association with the Sudanese low pressure on the surface of the earth and its movement in the southwest-northeast direction over the study area and the Arabian high pressure with its establishment over the Arabian Sea and Oman is the main factor in transferring the moisture of the Arabian Sea and Oman into the Sudanese low pressure. The high pressure established over the Arabian Peninsula, the Arabian Sea and the northwestern Indian Ocean as one of the necessary conditions for the formation, strengthening and development of the Sudanese low pressure (Lashkari, 2003, 134) helps to further strengthen the precipitation system by advection of warm and humid air into the precipitation system. In the troposphere maps on the day of the peak activity of the precipitation system, the western and southwestern regions, which had a positive troposphere maximum, faced widespread and heavy rainfall. Jet stream maps at the levels of 250 and 300 hPa indicate the location of the subtropical wind with a southwest-northeast direction that passed through the northeast of Africa and the core of the maximum jet stream speed was over Arabia and the Red Sea. The studied area was also on the left side of the jet stream outlet, which coincided with the omega path and humidity and the left half of the jet stream outlet was located exactly in the east and in front of the trough axis, which has well discharged and diverged the ascending air in front of the trough. The results of this study on the impact of the Sudanese system are consistent with the research of Lashkari (1996), Mofidi (2004), and Omidvar (2007). Also, the largest amount of moisture was taken from the water sources of the southern Red Sea, western Arabia and Oman, respectively, while there was a small amount of moisture transfer from the Mediterranean. Which is consistent with the results of Darand and Pazhoh (2019).

References

[1] Akbari, T., Azizi, G., Asadi, A. & Davodi, M. The role of blocking system in heavy precipitation of Iran (a case study: southeast of Iran January 2008). Arab J Geosci, 9(591), 591-606. (2016)

[2] Littmann, T. An Empirical Classification of Weather Types in the Mediterranean Basin and Their inter Relation with Rainfall. Theorical and applied Climatology, 5, 161-171. (2000)

[3] Alijani, B. Identification of rainy weather types based on circulation calculations, Geographical Research Quarterly, 63-64, 114-132. (2002)

[4] Asakereh, H., & Razmi, R. Climatology of precipitation in northwest Iran. Geography and Development, 25, 137-158. (2011)

[5] Busher, K. The Earth's Climate, Extratropical Region. translated by Bahloul Alijani, Volume 2, Jahad Daneshgahi Publishing House, Tehran.(1994)

[6] Darand, M. & Pazhoh, F. Synoptic analysis of sea level pressure patterns and vertically integrated moisture flux convergence vimfc during the occurrence of durable and pervasive rainfall in iran. Dynamics of Atmospheres and Oceans, 86, 10-17. (2019)

[7] Dayan, U. & Abramski R. Heavy Rain in the Middle East Related to Unusual Jet Stream Properties, Ball. Bulletin American Meteorological Society, 64(10), 1138-1140. (1983)

[8] Ghassabi, Z., Fattahi, E. & Habibi, M. Daily Atmospheric Circulation Patterns and Their Influence on Dry/Wet Events in Iran. *Atmosphere*, *13* (1), 1-17. (2022)

[9] Ghavidel, Y. & Jafari Hombari, F. Synoptic analysis of unexampled super-heavy rainfall on April 1, 2019, in west of Iran. Nat Hazards, 104(2),1567–1580. (2020)

[10] Kahan, R., Baruch, E., & Dayan, U. Synoptic Climatology of Major Floods in the Negev Desert, Israel. Journal Climatol, 22, 867-882. (2002)

[11] Lashkari, H. Synoptic pattern of heavy rainfall in the south and southwest of Iran. PhD thesis, supervised by Houshang Ghaemi. Tarbiat Modares University, Faculty of Humanities, Department of Geography. (1996)

[12] Lashkari, H. Routing of Sudanese low-pressure systems entering Iran. Modarres Quarterly, 2, 133-156. (2002)

[13] Lashkari, H. Mechanism of formation, strengthening and development of the Sudan low pressure center and its role on precipitation in the south and southwest of Iran. Geographical Research, 46, (2003).

[14] Mafidi, A., & Zarrin, A. Synoptic study of the effect of Sudanese low-pressure systems on the occurrence of flood-

causing precipitation in Iran. Quarterly Journal of Geographical Research, 77, 136-113. (2005)

[15] Mafidi, A. Synoptic study of flood-causing precipitation originating from the Red Sea region in the Middle East. Quarterly Journal of Geographical Research, 75, 71-93. (2004)

[16] Maheras, P., konstantia, T, anagnostopoulu, Ch., Vafidais, M., patriaks, L., & Flokas, H. On the Relationships between Circulation Type and Changes in Rainfall Variability in the Greece. International Journal of Climatology, 24 (24), 1695–1712. (2004)

[17] Masoudian, S. A. Identifying circulation patterns that cause large floods in Karun. Geography and Development, 5, 161-182. (2005)

[18] Masoudian, S. A. Synoptic climatology and its application in environmental studies. first edition, University of Isfahan. (2006)

[19] McGuirk, J. P., Thompson, A.H., & Schaefer, J.R. An Eastern Pacific Tropical Plume. AMS Journals Online's, 116, 2505-2521. (1988)

[20] Mohammadi, H., Fattahi, E., Shamsipour, A.A., & Akbari, M. Dynamic analysis of Sudanese systems and precipitation occurrence in southwestern Iran. Quarterly Journal of Applied Research in Geographical Sciences, 24, 24-7. (2012)

[21] Omidvar, Kl. Analysis of synoptic and thermodynamic conditions of precipitation occurrence in Shirkuh region. Geographical Research, 59, 81-98 (2007)

[22] Omidvar, K., Tany, N., Ebrahimi, R., & Ghiyasi, E. Dynamic synoptic analysis of heavy cloud precipitation on 24 December 2014, a case study of Kohgiluyeh and Boyer Ahmad, Journal of Physical Geography, 11(41), 11-36. (2018)

[23] Pazhoh, F., & Darand, M. Spatiotemporal characteristics of daily precipitation concentration in Iran. *Environ Dev Sustain,* (2024). https://doi.org/10.1007/s10668-024-05428-1

[24] Petra, S., Andreas, F., & Herbert, F. Synoptic and Regional Patterns of Heavy Precipitation in Austria. Institute of Metorology, university of Natural Resource and Applied Life Science Vienna, 1-23. (2005)

[25] Sabziparvar, A.A. Synoptic study of flood-causing systems in southwestern Iran. supervised by: Mohammad Khairandish, Master's thesis in meteorology, University of Tehran, Institute of Geophysics. (1991)

[26] www.esrl.noaa.gov/psd/data.ncep.reanalysis

[27] Zaki Zadeh, M. B., Saligheh, M., Nasserzad, M. H. & Akbari, M. Statistical analysis and synoptic most effective jet stream pattern creating the precipitation of Iran. *Journal of Natural Environmental Hazards*, *7*(15), 31-48. (2018)